UNIVERSITY OF CALIFORNIA,
IRVINE

Slippery Interfaces and Extreme Strain in Reconfigurable van der Waals Devices

DISSERTATION

submitted in partial satisfaction of the requirements
for the degree of

DOCTOR OF PHILOSOPHY

in Physics

by

Andrew Zoltan Barabas

Dissertation Committee:
Javier Sanchez-Yamagishi, Chair
Luis Jauregui
Ruqian Wu

2024

TABLE OF CONTENTS

Page

LIST OF FIGURES **v**

LIST OF TABLES **vii**

ACKNOWLEDGMENTS **viii**

VITA **ix**

ABSTRACT OF THE DISSERTATION **xi**

1 Introduction **1**
1.1 Organization 1
1.2 Van der Waals Background 2
1.3 Atomic force microscopy (AFM) basics and Park NX10 3

2 Mechanically reconfigurable van der Waals devices via low-friction gold sliding **6**
2.1 Paper Main Text 6
2.1.1 Introduction 7
2.1.2 Low friction gold on hexagonal boron nitride 8
2.1.3 Sliding gate devices: Mechanically-tunable quantum point contact . . 11
2.1.4 *In-situ* heterostructure and cryogenic manipulation 13
2.1.5 Discussion 18
2.2 Materials and Methods 19
2.2.1 General Fabrication Techniques 19
2.2.2 Friction Measurements 20
2.2.3 Quantum point contact device 22
2.2.4 *In-situ* sliding 23
2.3 Supplemental Information 28
2.3.1 hBN-graphite friction 28
2.3.2 Cr-Au friction on hBN 29
2.3.3 QPC conductance map kink 31
2.3.4 QPC contact resistance 31

3 Mechanically reconfigurable van der Waals devices via low-friction gold sliding: Additional details **36**
3.1 AFM Z Scan drift . . . 36
3.2 AFM before/after annealing Au . . . 38
3.3 COMSOL tip simulation . . . 38
3.4 AFM tip torsional sensitivity . . . 44
3.4.1 Stick slip motion . . . 46
3.4.2 Manipulating gold on hBN . . . 47
3.5 Room temperature probe and AFM manipulation . . . 47
3.6 Montana cryostat cryogenic manipulation . . . 50
3.6.1 Janis ST-500 cryogenic manipulation . . . 51
3.7 Moire charge pumping devices . . . 52
3.7.1 Theory and charge pumping mechanism . . . 52
3.7.2 Open face devices . . . 54
3.7.3 Rotors and Cr,Ti friction . . . 55
3.7.4 Outlook . . . 55
3.8 Curved metal with super low friction . . . 56
3.9 Electrostatic thermal actuators . . . 59
3.10 Motion due to fluids . . . 62

4 Manipulating moires by controlling heterostrain in van der Waals devices **63**
4.1 Paper main text . . . 63
4.1.1 Introduction . . . 64
4.1.2 Heterostrain technique . . . 65
4.1.3 Characterization of moire with CAFM . . . 68
4.1.4 Effects on electronic properties . . . 70
4.1.5 Theoretical calculations . . . 73
4.1.6 Conclusion . . . 75
4.2 Materials and Methods . . . 76
4.2.1 Sample Fabrication . . . 76
4.2.2 Transport measurements . . . 79
4.2.3 AFM manipulation technique . . . 79
4.2.4 Conductive AFM . . . 80
4.2.5 Moire FFT strain fitting . . . 80
4.2.6 Error Analysis . . . 81
4.3 Supplementary Information . . . 82
4.3.1 Sample fabrication figures . . . 82
4.3.2 AFM image of torn graphene device . . . 83
4.3.3 Unaligned G-BN strain Raman signal . . . 84
4.3.4 AFM drift correction . . . 85
4.3.5 Uniaxial heterostrain model and fitting . . . 87
4.3.6 CAFM and strain data from other devices . . . 90
4.3.7 Satellite Dirac peak temperature dependence . . . 92
4.3.8 Additional magnetotransport . . . 94
4.3.9 Additional theory . . . 95

4.3.10 Detailed theory methods 97

5 Manipulating moires by controlling heterostrain in van der Waals devices: Additional details 104

5.1 Massaging out strain with AFM tip 104
5.2 AC Conductive AFM (and AFM internal lock-ins) 106
5.3 *In situ* AFM measurement 110
5.4 AFM drift velocity 111
5.5 Moire Fitting Error 112

Bibliography 115

LIST OF FIGURES

Page

1.1 AFM tip-sample interaction potential 4
1.2 AFM tip frequency shift 5

2.1 Au-hBN sliding friction 11
2.2 Quantum point contact schematics and gate sweeps 14
2.3 *In situ* mechanically-reconfigurable devices 16
2.4 Example AFM deflection linetraces for various sizes of gold squares on hBN. 28
2.5 All static and kinetic deflection values for gold-on-hBN and hBN-on-graphite extracted from linetraces. 29
2.6 Voltage deflection for 2 µm x 2 µm, 100 nm thick gold + 3 nm Cr sticking layer square on hBN. 30
2.7 Images of mechanically reconfigurable quantum point contact device 30
2.8 Three hole-doped quantum hall regions in series. 31
2.9 Custom build cryogenic manipulation setup 33
2.10 Optical images of hockey puck device fabrication. 34
2.11 hBN-encapsulated graphene device with transferred scanning top gate serpentine electrode, donut inner diameter is 3 µm. 35

3.1 AFM Z Scan versus time 37
3.2 Au grains before and after annealing 38
3.3 SEM image of Tap 300 cantilever 39
3.4 Tap 300 mesh in COMSOL 40
3.5 AFM Cantilever apex and pushing surface. 41
3.6 Thickness of push surface variation 42
3.7 Simulation to test the spring constant due to pushing into soft Au rectangle 43
3.8 Cantilever spring constant vs height of push 43
3.9 Tap 300 SEM image and initial simulated geometry 44
3.10 AFM tip sensitivity vs static friction peak. 45
3.11 Stick slip motion 46
3.12 Au-only pushed by tapping mode AFM (AS18) 47
3.13 Flat Au-only pads on hBN for probe tip manipulation 47
3.14 Before and after probe tip manipulation with anti-slip measures. 48
3.15 Before and after probe tip manipulation with anti-slip measures (IS-SiO2-01-T1) 49
3.16 Montana crude probe tip manipulation setup and damaged sample 50
3.17 Progression of ST-500 cryogenic manipulation setup 51

3.18 Current state of ST-500 cryogenic manipulation setup . . . 52
3.19 Aligned graphene-hBN band structure and density of states . . . 53
3.20 Illustration of localized charge and expected current for oscillatory motion . 54
3.21 Possible fabrication for graphene hockey puck devices . . . 56
3.22 Hockey puck devices . . . 57
3.23 Arched Au/Cr metal on graphene/SiO_2 (AG6-TL) . . . 58
3.24 Au/Ti mask on hBN suspended in air over the edge (AS43) . . . 59
3.25 Graphite electrostatic actuator device and a related COMSOL force simulation 59
3.26 Au electrostatic and thermal actuators on hBN . . . 61
3.27 Au sliding on hBN due to liftoff in acetone (AS59) . . . 62

4.1 Controlling heterostrain to manipulate vdW moires formed between graphene and hBN . . . 66
4.2 Progressive uniaxial strain and spatial uniformity in device B . . . 68
4.3 Effects of uniaxial heterostrain on the transport properties of graphene-hBN devices . . . 70
4.4 Aligned graphene-hBN theoretical band structure and DOS . . . 73
4.5 Optical images of gold based transfers . . . 82
4.6 Deterministic alignment of graphene to hBN substrate . . . 82
4.7 Device E before (a) and after (b) AFM cutting . . . 83
4.8 Torn graphene-hBN devices . . . 83
4.9 Stretching and Raman of unaligned G-hBN . . . 84
4.10 AFM moire wavelength reproducibility . . . 86
4.11 Moire peak fitting . . . 88
4.12 Moire wavelength versus strain for Device C (left) and Device A (right) . . . 90
4.13 Extreme moire heterostrain in Device A . . . 91
4.14 Temperature dependent gate sweeps for various devices . . . 92
4.15 1.6K magneto transport of device B . . . 94
4.16 Contour plots of first electron mini band . . . 95
4.17 First hole mini band contours dependence on strain angle . . . 96
4.18 Band structure cuts for several strain values at 0° strain angle . . . 97

5.1 Stitched together CAFM images spanning the entire device (MS24-B) . . . 105
5.2 AFM moire dislocation streaks (MS24-B) . . . 105
5.3 Conductive AFM circuit . . . 106
5.4 AFM 4 internal lock-ins . . . 107
5.5 AFM CAFM clip-type carrier . . . 109
5.6 AFM wired DIP socket . . . 111
5.7 AFM drift velocities in y and x direction . . . 111
5.8 Output from moire error analysis . . . 113
5.9 Addtional output from moire error analysis . . . 114

LIST OF TABLES

Page

3.1 Tip contact area thickness effect on spring constant 41
3.2 Au contact area effect on spring constant 42
3.3 Pyramid elasticity effect on spring constant 44

4.1 Parameters and uncertainties for main text figures 89
4.2 Table of the device dimensions presented in Figure 4.14 93

ACKNOWLEDGMENTS

I would like to thank:

my dissertation committee for their feedback on this work,

my advisor Javier, for his excellent advising and generally attention to his students well-beings,

Ian Sequeira, my lab partner throughout this PhD,

Michael Sandler, all of my other climbing and skiing partners, and the UCI Climbing and Alpine clubs for *really* looking out for my mental (and physical) well-being,

my close friends Daniel, Rachel, Brian, and Jennie for all of the life-affirming bits and yes-ands,

and especially my family for all their support throughout these years.

I thank The American Association for the Advancement of Science for permission to include Chapter Two of my dissertation, which originally published in *Science Advances*.

Financial support was provided by:

the University of California, Irvine,

National Science Foundation Career Award DMR-2046849,

and National Science Foundation Materials Research Science and Engineering Center program through the UC Irvine Center for Complex and Active Materials DMR-2011967.

VITA

Andrew Zoltan Barabas

EDUCATION

Doctor of Philosophy in Physics **2024**
University of California, Irvine *Irvine, California*

Bachelor of Science in Physics **2018**
University of California, Santa Barbara *Santa Barbara, California*

RESEARCH EXPERIENCE

Graduate Researcher **2019–2024**
University of California, Irvine *Irvine, California*

Undergraduate Researcher **2016–2018**
University of California, Santa Barbara *Santa Barbara, California*

TEACHING EXPERIENCE

Teaching Assistant **2018-2019, 2023**
University of California, Irvine *Irvine, California*

CalTeach Teaching Assistant **2015-2018**
San Marcos High School *Goleta, California*

CalTeach Teaching Assistant **2015**
Dos Pueblos Engineering Academy *Goleta, California*

REFEREED JOURNAL PUBLICATIONS

Mechanically reconfigurable van der Waals devices via low-friction gold sliding **2023**
Science Advances

Electrically driven amplification of terahertz acoustic waves in graphene **2024**
Nature Communications

Manipulating moires by controlling heterostrain in van der Waals devices **2024**
In Preparation

ABSTRACT OF THE DISSERTATION

Slippery Interfaces and Extreme Strain in Reconfigurable van der Waals Devices

By

Andrew Zoltan Barabas

Doctor of Philosophy in Physics

University of California, Irvine, 2024

Javier Sanchez-Yamagishi, Chair

Interfaces of van der Waals (vdW) materials, such as graphite and hexagonal boron nitride (hBN), exhibit low-friction sliding due to their atomically flat surfaces and weak vdW bonding. We developed techniques to make selectively sliding and gripping connections to van der Waals materials in order to electrically contact, apply large forces selective layers, and selectively slide layers of a van der Waals heterostructure.

We applied this to create scannable top gate devices, fully slidable heterostructures, reconfigurable & tunable devices, highly heterostrainable devices, and devices which can be manipulated and measured simultaneously. Our approach opens a wide parameter space to control van der Waals devices beyond what was previously possible.

Chapter 1

Introduction

Where did all the coffee cups go? - Javier Sanchez-Yamagishi

1.1 Organization

This dissertation begins with an introduction to van der Waals materials and atomic force microscopy.

This is followed by a chapter on the gold sliding project and accompanying publication, where our published paper, methods section, and supplementary information appear in their entirety. The next chapter provides additional details which do not appear in the final paper. This is primarily information on techniques, unpublished data, fabrication methods which were not used for the final measurement, and projects which were not able to be completed with the techniques and time available.

The fourth chapter focuses on the advancement of our sliding technique to strongly heterostrain devices. This content is in preparation for submission to a peer-reviewed journal. It too is followed by an additional details chapter.

1.2 Van der Waals Background

Van der Waals (vdW) materials are a unique class of materials whose chemical bonds lie only in plane, leaving them atomically flat and free of dangling bonds in the out-of-plane direction. In their bulk form, only the relatively weak van der Waals force holds layers together. This allows layers to be peeled apart, thinned down, and isolated even to the monolayer level.

vdW materials span the full spectrum of materials properties: metals, insulators, semiconductors, ferromagnets, superconductors, etc. In addition to being exfoliable, they can be reassembled to form a heterostructure with layers of differing materials. The resulting sandwich can have new properties owing to proximitization of layers and most interestingly, due to moire patterns between layers. Moire patterns introduce additional periodicity to the system, modulating the potential, interlayer tunneling, hopping terms, etc which can strongly affect the heterostructure properties.

The weak out-of-plane bonds and atomic flatness enable another feature unique to vdW materials, extremely low friction. This allows layers to be slid, rotated, and strained without strongly affecting neighboring layers. It is this mechanical tunability which inspired our work here.

Towards the start of my PhD there was limited work taking advantage of this low friction to make novel van der Waals heterostructure devices. The primary studies thus far were: simple friction studies of vdW-vdW interfaces and metal nanoparticles on vdW devices[1–7] twist angle dependent studies of aligned g-BN heterostructures[8, 9] and out-of-plane graphite conductance[10, 11]. Conspicuously absent were manipulations at cryogenic temperatures, which would enable in situ study of these mechanical parameters, and translation devices, such as scanning probe systems which could operate in direct atomic contact. We were also inspired by the richness of mechanical applications demonstrated by suspended MEMS

structures[12] and saw the opportunity to develop similar techniques in the still wide-open field of sliding vdW materials.

1.3 Atomic force microscopy (AFM) basics and Park NX10

AFM is a scanning probe microscopy technique. The probe is a very sharp tip (∼1-30 nm diameter) on a cantilever. A laser points at the cantilever and reflects onto a 4 quadrant "position sensitive" photodiode (PSPD). When the tip deflects, the laser position shifts on the photodiode, resulting in a change in the photodiode voltage.

In contact mode, the most basic mode of operation, the desired contact force (corresponding to a vertical PSPD voltage) is selected as the set point for a feedback loop. The tip is rastered over the sample and height of the tip is adjusted in order to maintain the set point force. This tip height is the topographic map of the sample. In addition to the Z Height channel, it is common to record the LFM (lateral force microscopy) channel, which outputs the lateral voltage signal from the PSPD. The Error channel is usually collected as well; it shows the difference between the setpoint force and the measured force (from the PSPD).

Due to the nonlinearity in the piezos which control the XYZ position, many modern AFMs (including the Park NX10) employ a sensor to measure the piezo position, rather than simply converting the applied piezo voltage to a displacement.

More advanced modes oscillate the tip at near resonance and measure height based on the shift in the resonance frequency due to proximity to the sample surface. The natural resonance of a harmonic oscillator is $\sqrt{\frac{k}{m}}$; however, the attractive interaction between the tip and sample modifies this as the tip approaches. The attraction results in an effective

spring constant, $k_{eff} < k$, which can be understood intuitively because the attraction negates some fraction of the cantilever's spring restoring force, pulling the tip down. This smaller effective spring constant results in a downward shift in the resonance frequency, and this too can be understood intuitively as the "stickiness" of the sample pulls on the tip, making it linger and decreasing its oscillation frequency.

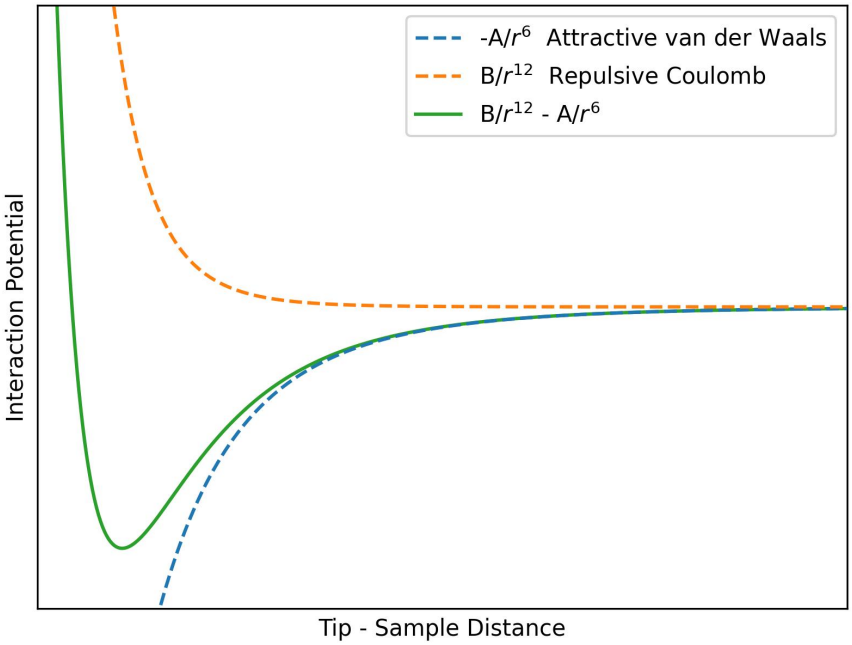

Figure 1.1: AFM tip-sample interaction potential

The combined potential is referred to as the Lennard-Jones or 12-6 potential.

This can be used to perform a "tapping" mode measurement, where the cantilever is driven at a slightly lower frequency than the resonance. When the tip approaches the surface, it feels an increased force, the resonance frequency shifts downward (towards the drive) which increases the amplitude of the tip oscillations causing it to "tap" the sample surface.

The general feedback mechanism is using the amplitude of the tip oscillations as the setpoint. When the tip is too far away, the oscillation amplitude is too small, and the feedback brings the tip closer. When the tip is too close to the sample the amplitude is larger than the setpoint, and the feedback moves the tip away. It is by feedbacking to keep this setpoint

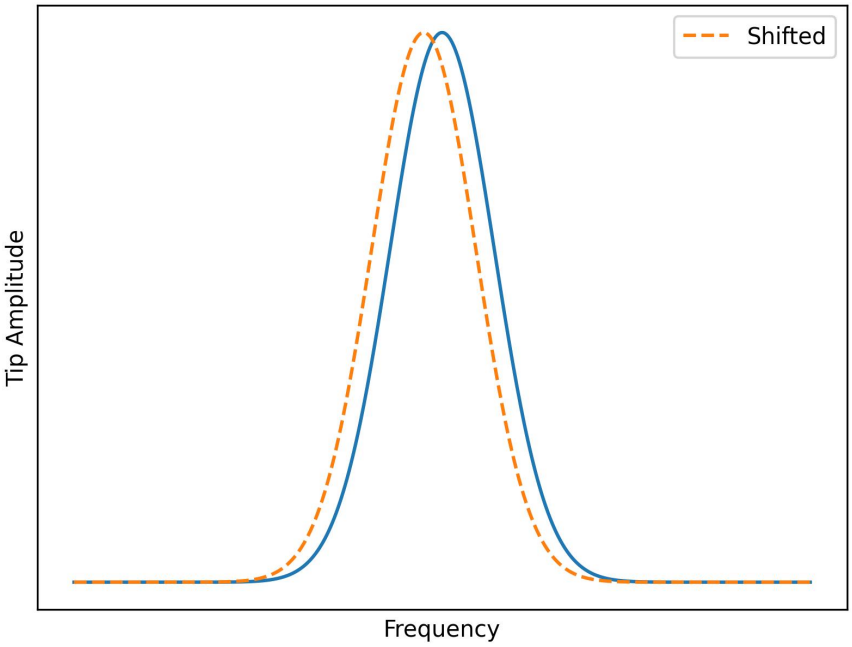

Figure 1.2: AFM tip frequency shift

The AFM tip resonance shifts downward in frequency due its the attractive interaction with the sample.

amplitude constant that the topography of a surface can be mapped.

The Park NX10 also has a variation on tapping mode, non-contact mode (NCM), which instead drives the tip slightly above the resonance. The peak still shifts down when the tip-sample distance decreases (Figure 1.2), however this moves the peak away from the drive and decreases the oscillation amplitude. In this mode the tip does not directly tap the sample, preserving both the tip sharpness and sample for longer. In my experience, I have found that NCM mode can be useful if you are concerned about damaging the tip/sample, but it almost always requires the user to adjust the default set point (use increments of 0.2-0.5 nm) and does not produce as high quality images as Tapping mode with a new tip.

Chapter 2

Mechanically reconfigurable van der Waals devices via low-friction gold sliding

I like water colors. I like acrylic paint... a little bit. I like house paint. I like oil-based paint and I love oil paint. I love the smell of turpentine and I like that world of oil paint very, very, very much. - David Lynch

This text was originally published in Barabas & Sequeira et al., Sci. Adv. 9, eadf9558 (2023), used with permission from The American Association for the Advancement of Science.

2.1 Paper Main Text

Abstract: Interfaces of van der Waals (vdW) materials such as graphite and hexagonal boron nitride (hBN) exhibit low-friction sliding due to their atomically-flat surfaces and

weak vdW bonding. We demonstrate that microfabricated gold also slides with low friction on hBN. This enables the arbitrary post-fabrication repositioning of device features both at ambient conditions as well as *in-situ* to a measurement cryostat. We demonstrate mechanically-reconfigurable vdW devices where device geometry and position are continuously-tunable parameters. By fabricating slidable top gates on a graphene-hBN device, we produce a mechanically-tunable quantum point contact where electron confinement and edge-state coupling can be continuously modified. Moreover, we combine *in-situ* sliding with simultaneous electronic measurements to create new types of scanning probe experiments, where gate electrodes and even entire vdW heterostructures devices can be spatially scanned by sliding across a target.

2.1.1 Introduction

Nanoscale electronic devices are typically static, with the material structure and device geometry set during the fabrication process. Exploring the full parameter space requires fabricating multiple devices with varying geometries and material structures. Ideally, a device's material structure and geometry would be reconfigurable *in-situ*, allowing for post-fabrication modification while simultaneously measuring its properties. Micro-electro-mechanical systems (MEMS) enable a limited range of mechanical reconfigurability at the cost of complex suspended device structures [12]. For conventional non-suspended devices, mechanical-modification of the device structure is typically not possible due to high friction forces at all interfaces.

An exception to this is van der Waals (vdW) layered materials, which exhibit low interfacial friction due to weak vdW bonds, atomically-flat layers, and lattice incommensurability [1–7]. Recently, this property has been exploited to perform twist-angle dependent studies of graphite and graphene-based heterostructures by sliding vdW flakes with an atomic force

microscope (AFM) [8–11]. This approach is powerful, but currently limited by difficulties in fabricating complex vdW heterostructures, as well as the need to perform experiments in ambient conditions.

Here, we show that microfabricated gold exhibits low-friction sliding on hexagonal boron nitride (hBN), a vdW material, at both ambient conditions and at cryogenic temperatures (7.6 K). The low-friction gold-hBN interface enables us to produce a wide range of slidable structures to form mechanically-reconfigurable vdW devices, including a tunable graphene quantum point contact and sliding-based scanning probe devices. Such devices can be modified ex-situ in an AFM or *in-situ* in a measurement cryostat.

2.1.2 Low friction gold on hexagonal boron nitride

We create reconfigurable structures, by depositing gold microstructures directly onto hBN flakes using electron beam lithography and electron beam evaporation (see "Friction measurements" in the Methods section for fabrication details) . By pushing laterally with an AFM tip, we can slide microscale, polycrystalline gold features as large as 35 μm^2 across the hBN surface. The low-friction sliding enables arbitrary repositioning of deposited features (Figure 2.1a-b). We observe that small features can even be moved by scanning an AFM tip in tapping mode. The motions are non-destructive, with no change to either the gold or hBN observable in AFM except for the cleaning of contaminants on the hBN surface, which are swept away by the sliding gold (Figure 2.1c).

To characterize the friction, we slide gold squares of different sizes on hBN using an AFM tip and determine the interfacial friction from AFM deflection measurements, similar to previous vdW tribological studies [3–5, 7, 13, 14]. Figure 2.1d illustrates the friction measurement scheme. First the tip is moved laterally at a fixed z-piezo extension elevated above the hBN surface (left panel). Once the tip makes contact with the edge of the stationary gold square it

deflects laterally, resulting in a voltage signal on the AFM photodiode (middle panel). The lateral deflection increases until the static friction of the gold-hBN interface is overcome, after which it drops to a constant value corresponding to the kinetic friction as the gold slides on the hBN (right panel). These regions are highlighted in an example deflection trace in Figure 2.1e, where the peak (static) voltage and constant (kinetic) voltage are indicated.

To determine the scaling of friction with interface size, we repeat these measurements multiple times each for 0.5 to 3 µm wide gold squares and observe a linear scaling of deflection voltages versus area, with slopes of 82 ± 6 mV/µm^2 (static) and 24.4 ± 0.6 mV/µm^2 (kinetic). Assuming that force is directly proportional to deflection voltage, our data shows that interface friction scales linearly with area, which is expected for polycrystalline interfaces [14]. By contrast, atomically flat and lattice incommensurate interfaces, including single-crystal gold nanoparticles on graphite, can exhibit sublinear scaling versus area [2, 3, 7, 14]. This suggests that increasing the grain size of our gold will decrease interface friction. To test this, we vacuum annealed our samples at 350 °C for 30 minutes and observed the deflection voltages decrease by 50%. The annealing process also caused the average gold grain size to increase from ∼20 nm to ∼80 nm, suggesting a connection; although, the removal of contaminants from the Au-hBN interface by heat annealing likely plays a role as well.

We convert the AFM deflection voltage to a lateral force using a linear model which requires both the AFM tip's lateral spring constant and the AFM's lateral sensitivity. The spring constant is the ratio of lateral force applied to the tip and lateral displacement, which we determine by simulating our tip in COMSOL Multiphysics. And the sensitivity is the ratio of lateral tip displacement and lateral deflection voltage measured on the AFM photodiode. To measure the lateral sensitivity, we use the slope of the static region of our deflection linetraces (see "Friction measurements" in the Methods section for more details).

Converting the deflection voltages yields forces of 6 µN (static) and 2 µN (kinetic) for a 9 m^2 gold square on hBN. Applying the conversion to the linear fits results in a friction force

per unit area. For the unannealed Au-hBN interface, the friction values are 800 nN/μm^2 (static) and 230 nN/μm^2 (kinetic), and after annealing they decrease to 400 nN/μm^2 and 100 nN/μm^2, respectively. These force values have uncertainties of 30%, dominated by uncertainty in the sensitivity, and should be considered upper bounds due to the calibration method and limitations of the linear model (see "Friction measurements" in the Methods section). These interfacial friction values are comparable to prior tribology studies of gold on graphite, which measured 50 to 430 nN/μm^2 (kinetic) for ∼60 to ∼100 nm wide, single-crystal, gold nanoparticles [13]. For additional comparison, the previously reported kinetic friction of unaligned graphite on hBN is smaller, at 15 nN/m^2 [4]. We have also made friction measurements of gold with a 3 nm Cr sticking layer on hBN, and initial tests show it exhibits roughly an order of magnitude higher friction than annealed gold on hBN without a sticking layer (see Figure 2.6 in Supplemental Information (SI)).

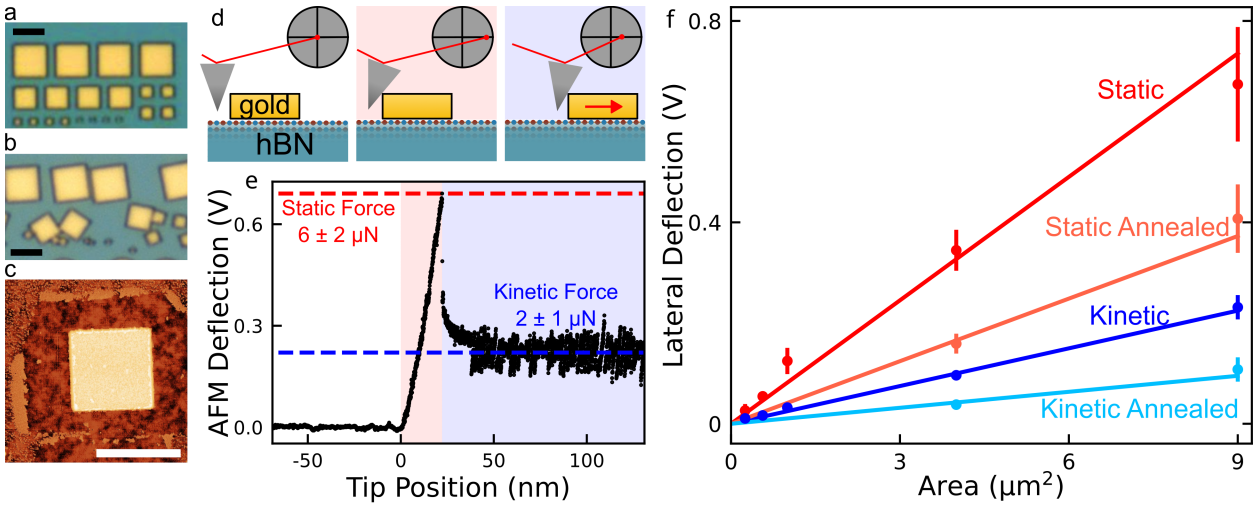

Figure 2.1: Au-hBN sliding friction

All scale bars are 3 μm. **(a&b)** Optical images of ∼170 nm tall gold squares on hBN before and after manipulation with an AFM tip. **(c)** AFM height image of 3 μm wide gold square on atomically flat hBN surface with contaminants swept aside by sliding. The RMS roughness of the swept hBN is 1 Å, and the height of the surface contaminants is roughly 8 nm. A non-linear color scale is used to highlight features across a wide range of heights. **(d)** Schematic illustrating AFM lateral friction measurement: before contact (left), during static friction (middle), during kinetic friction (right). **(e)** AFM friction linetrace for a 3 μm wide square with the tip moving at 1 nm/s. The peak voltage corresponds to the Au-hBN static friction, and the subsequent constant voltage corresponds to the kinetic friction. **(f)** Lateral deflection voltage versus interface area between gold and hBN for 0.5, 0.75, 1, 2 and 3 μm wide squares, before and after annealing at 350 °C for 30 minutes. Each data point is the average of multiple measurements for each size. Error bars show standard deviation. Lines are linear fits through zero, fitting only the 4 and 9 μm^2 data points; this excludes smaller deflection data points which have variable AFM sensitivity (see "Friction measurements" in the Methods section for more details).

2.1.3 Sliding gate devices: Mechanically-tunable quantum point contact

The low friction between Au-hBN enables studies of vdW quantum devices in which reconfigurable gold gates are used to mechanically-modify electron confinement. Gate-defined quantum point contacts (QPC) and quantum dots are of particular interest as they are integral for making graphene-based qubits [15–17] and for studying non-abelian quasiparticles

[18, 19].

We apply this unique confinement control capability to make a reconfigurable QPC defined by movable gold-only top gates on a hBN-encapsulated graphene device (Figure 2.2a). The top gates confine electrons by depleting the graphene into a band gap, thereby forming a narrow QPC constriction between two conducting regions. Although graphene lacks an intrinsic band gap, one forms in a perpendicular magnetic field at zero density due to exchange interactions [20]. Therefore, in the quantum hall regime, we can study the edge mode transmission through the constriction at different Landau level filling factors and QPC separations by holding the dual-gated region at the charge neutrality point while sweeping the back-gate voltage [21, 22].

To adjust the QPC separation, the top gates are physically moved with an AFM tip at ambient conditions, modifying the QPC confinement mechanically (Figure 2.2a). We then cool the sample to 1.5 K, apply a 9 T out-of-plane magnetic field, and measure the resistance versus top-gate and back-gate voltages. From these measurements we determine the QPC conductance, referred to as G_{QPC}, by taking the inverse of the measured resistance after subtracting a contact resistance (see "Quantum point contact device" in the Methods section and SI for more details).

Adjusting the QPC separation modulates the tunneling coupling between counterpropagating edge modes, thereby tuning their transmission through the QPC constriction. This is illustrated in Figures 2.2b and 2.2c, which show different gate separations of the QPC but at identical gate voltage conditions. The Landau level filling factors shown are $\nu_{bg} = -2$ for the back gate and $\nu_d = 0$ for the dual-gated regions. When the QPC separation is large, edge modes transmit across the device unimpeded, resulting in a G_{QPC} of 2 e^2/h (Figure 2.2b). In contrast, at the same filling factors, a smaller QPC separation causes the counterpropagating edge modes to tunnel couple and backscatter, decreasing $G_{QPC} \leq 2\ e^2/h$ (Figure 2.2c).

We measure the QPC conductance with $\nu_d = 0$ for four separations: 1110 nm, 170 nm, 80 nm, and 10 nm (Figure 2.2d) It is apparent that physically narrowing the QPC generally decreases G_{QPC} at a given back-gate voltage. At filling factor $\nu_{bg} = -2$ (vertical dashed line at $V_{bg} = -1.65$ V), a 2 e^2/h plateau is observed for the 1110 nm separation, corresponding to the edge modes in the back-gated region transmitting across the device unimpeded, equivalent to Figure 2.2b. At the same filling factor, narrowing the QPC separation to 170 nm decreases G_{QPC} to between 1 and 2 e^2/h, indicating partial reflection of one edge mode. Further narrowing to 80 nm results in a 1 e^2/h plateau. This surviving quantized plateau is explained by the spatial separation of the edge modes. The innermost counterpropagating modes are close enough to completely backscatter via tunneling, while the outer modes are still too far apart to couple and instead transmit through the QPC fully. Narrowing the QPC separation further to 10 nm results in partial reflection of the remaining edge mode such that $G_{QPC} < 1$ e^2/h (as illustrated in Figure 2.2c). Similarly, for $\nu_{bg} = -1$ ($V_{bg} = -0.65$ V), a 1 e^2/h plateau is observed in the 1110 nm separation which we reduce to 0.14 e^2/h by narrowing the QPC separation, demonstrating our ability to mechanically pinch-off the conductance. In the full device conductance map (Figure 2.2e-h), the gate voltage region where pinch off is attained (right of diagonal line) grows in size as the gate separation is reduced.

The mechanical gate tuning we demonstrate offers an unprecedented level of control, as confinement geometry and physical position of the QPC can be modified independent of gate voltages. Such an approach will be highly useful for tuning the properties of gate-defined quantum dots and QPCs in vdW heterostructures.

2.1.4 *In-situ* heterostructure and cryogenic manipulation

An exciting aspect of the low friction between gold and hBN is the potential for true *in-situ* manipulation of a device's atomic structure. Here, *in-situ* means simultaneous manipulation

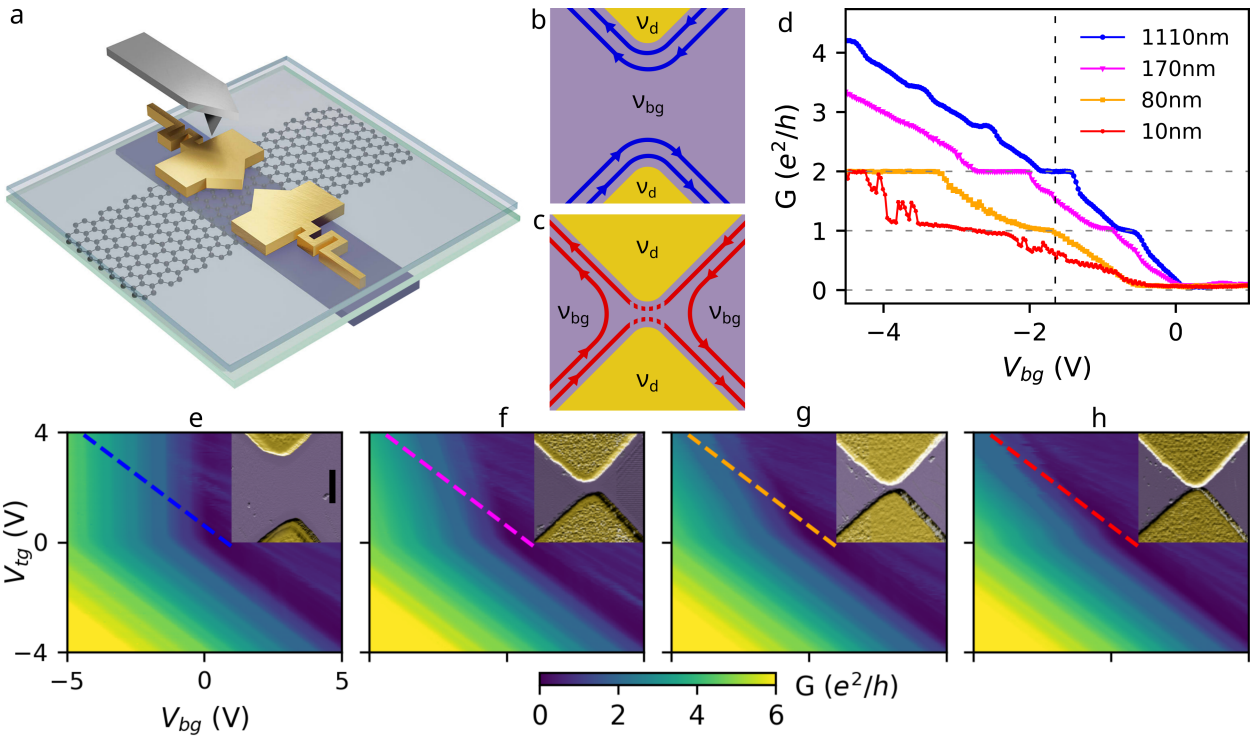

Figure 2.2: Quantum point contact schematics and gate sweeps
(a) Schematic of an hBN-encapsulated graphene device with a local graphite back-gate and flexible serpentine leads connected to the movable QPC top gates (metal contacts to the graphene and graphite not shown). **(b&c)** QPC edge mode schematic for $\nu_d = 0$ and $\nu_{bg} = -2$. **(b)** For a large QPC separation all edge modes are completely transmitted, as in the 1110 nm separation. **(c)** Reduced QPC separation such that the innermost edge mode is completely backscattered while the outer edge mode is partially backscattered (indicated by the dotted lines), as in the 10 nm separation. **(d)** Line cuts of full 2D conductance color plots taken at 9 T and 1.5 K along $\nu_d = 0$ for each of the four separations. The vertical dashed line at Vbg = -1.65 V indicates the $\nu_{bg} = -2$ filling. **(e,f,g,h)** Conductance color plots versus graphite back-gate and QPC top-gate voltages at separations of 1110 nm, 170 nm, 80 nm, and 10 nm, respectively. Dashed lines correspond to $\nu_d = 0$ linecuts presented in **(d)**. Insets are false color AFM amplitude images of QPC gates. Scale bar in **(e)** is 500 nm and applies to all AFM images.

and measurement under the extreme conditions often required for quantum experiments, such as cryogenic temperatures, high magnetic fields, and high vacuum. Of these conditions, cryogenic manipulation presents the biggest challenge because friction typically increases significantly at low temperatures due to reduced thermal vibrations and the freezing of gas within the cryogenic vacuum space [23].

To advance vdW manipulation beyond pushing individual flakes at ambient conditions, we

aim to achieve deterministic lateral motion of flakes and even whole heterostructures by creating a rigid mechanical connection to them. The conventional method for vdW flake manipulation, as demonstrated in Figures 2.1 & 2.2 and prior works [8–11] uses a sharp AFM tip to push a flake from the side and then reimages the flake position using the same tip. This, however, does not result in deterministic, one-to-one motion of the flake and makes certain manipulation applications such as scanning infeasible. Likewise, this manipulation technique is not well-suited to overcome the high friction forces at cryogenic temperatures and for large interface areas due to the small contact area between the sharp tip and the flake. In fact, we encounter the limits of this style of motion with very large gold contacts in our QPC devices (area >35 μm^2), which are cut by the AFM tip as it pushes laterally. To address these issues, we have created metal handles which interface the AFM tip to a vdW heterostructure.

The handle grips the vdW flakes/heterostructures by overlapping the flake edges, so that it conforms to the flake and distributes force along the flake's edges. We press-fit a flattened AFM tip into a donut-shaped hole in the handle, which deforms the metal to match the tip shape and provides increased grip. This strong connection enables deterministic sliding of gold on hBN at cryogenic temperatures (T = 7.6 K, see Figure 2.3a and Movie S1 in SI).

Despite the increased friction at cryogenic temperatures, as evidenced by visible tip flex in Movie S1, we observe that the hBN surface is left pristine and undamaged after more than 100 motions at a speed of 30 µm/s (Figure 2.3b). See "*In-situ* sliding" in the Methods section for details about the manipulation technique and setup. Cold sliding can enable a variety of experiments including reconfigurable vdW heterostructures at cryogenic temperatures, which would allow for rapid, continuous measurements with respect to physically reconfigurable parameters. While mechanical linkage and motion is useful in its own right, electrical contact to moveable structures is also critical to perform many experiments. To this end, we fabricate flexible serpentine-shaped electrodes connected to our donut handles which are anchored at

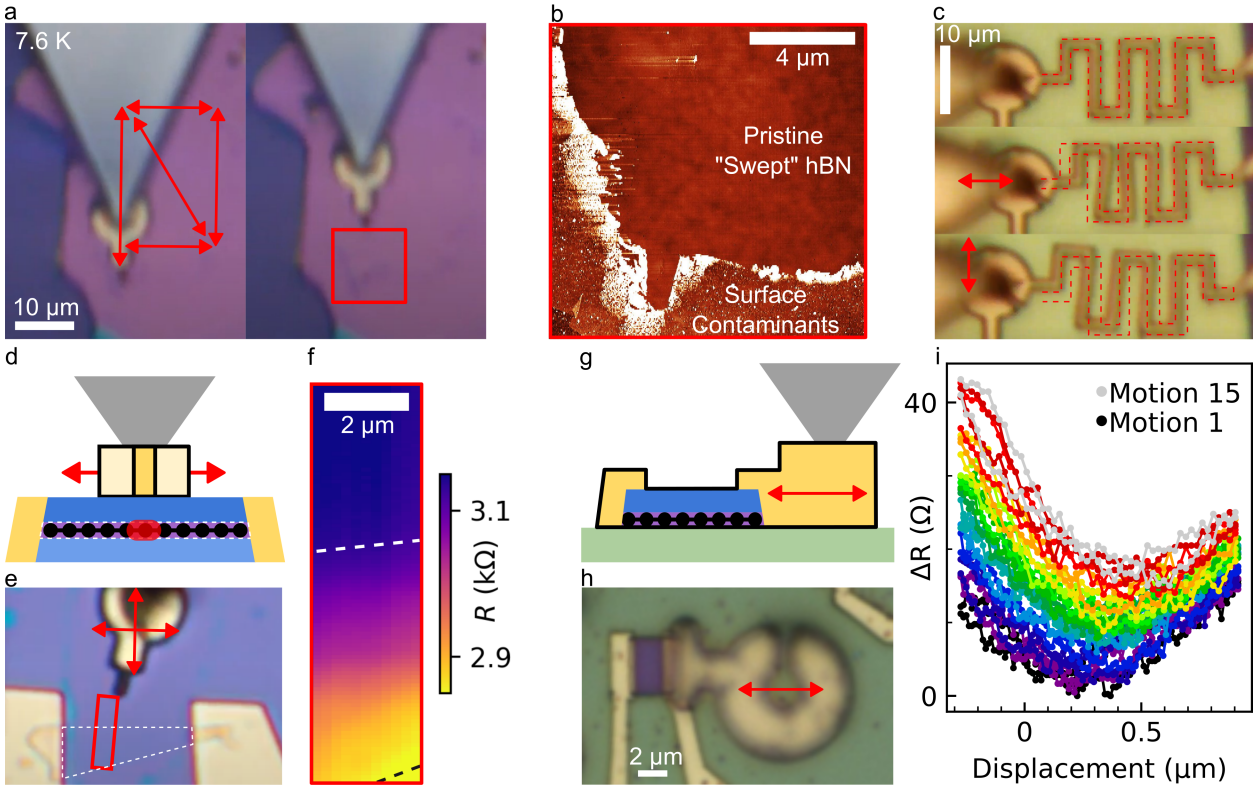

Figure 2.3: *In situ* mechanically-reconfigurable devices

(a) Optical images showing gold sliding on hBN (pink) at 7.6 K, actuated by an AFM tip (gray). Arrows denote the range and direction of motions. Dark purple on the left is the SiO2 substrate. See Movie S1 in the SM for a video recording of the motions. **(b)** AFM image of hBN surface after cryogenic scanning motions from **(a)** showing the hBN surface is left undamaged with only swept up surface contaminants. AFM area is the solid red boxed area in **(a)**. **(c)** Optical images of gold serpentine electrodes on hBN (pale yellow/green) showing 2 μm longitudinal and transverse motions. Red dotted lines outline the initial position. Video recordings of oscillating motion shown in SM Movie S2 and S3. **(d)** Side profile schematic of a sliding top-gate hBN-encapsulated graphene device, actuated with an AFM tip. Top-gate slides over stationary graphene to change local gating and device resistance. **(e)** Top-down optical image of the same device. The graphene is outlined with a dotted white line, and the light purple background is hBN. Red rectangle is 2.4 x 9.5 μm. **(f)** Graphene resistance versus top-gate position. Scanning range shown as the red rectangle in the optical image. Dashed lines indicate graphene edges. **(g)** Side profile schematic of a slidable graphene-hBN device on a stationary hBN substrate, actuated with an AFM tip. The slidable features in the schematic are outlined in black. (h) Top-down optical image of the same device. The pale green background is hBN. **(i)** 2-probe resistance of the slidable graphene device versus sliding position (see Movie S4 in SM for the video recording). 0 μm corresponds to the initial, transferred position. The increase in resistance over subsequent motions is likely due to photodoping from the light source used for imaging.

one end off the hBN flake on the SiO_2, shown in Figure 2.3c. We are able to oscillate these electrodes at 10 Hz with an amplitude of 2 µm by actuating with an AFM tip and the same donut interface described above (video available online). We find these accordion geometries with a wire cross section of 1 µm thick and 1 µm wide are able to stretch over 10 µm before breaking. Note, except for extreme displacements, the friction force is high enough to prevent the electrodes from springing back when the AFM tip is disengaged.

By combining mechanical motion and flexible electrodes, we create a sliding scanning top-gate, shown in Figure 2.3d-f. At room temperature, we raster a gold top-gate by sliding it over an encapsulated graphene-hBN device, modulating the device resistance by changing the overlap between the graphene and top-gate. The resistance versus gate position is plotted in Figure 2.3f, which can be interpreted as a coarse image of our graphene device convolved with the geometry of the sliding gate. This constitutes a new mechanism for scanning probe microscopy [24], where a scanned gate is in direct atomic contact with the sample, obviating the need for the feedback control of the probe-sample distance that is typical with scanning probes.

Taking advantage of the low-friction of both graphene-hBN and Au-hBN interfaces, we apply our technique to make a slidable, contacted vdW heterostructure, shown optically and schematically in Figure 2.3g,h. Here an entire graphene device is translated over an hBN substrate, actuated via a metal handle. The graphene, edge-contact electrodes, and top hBN all slide as a single unit, and allow for continuous measurement of the graphene as it is moved. Figure 2.3i shows the change in graphene resistance as it is translated back and forth. As the graphene slides 1.2 µm, we observe a reproducible modulation of the device resistance corresponding to a maximum change of 10-15 Ω. Naively, one would not expect any change in the graphene resistance due to translating the device. One explanation for this effect is that the graphene is gated by charge inhomogeneity in the hBN [25], modulating its resistance and causing it to act as a local charge sensor. Another effect which can arise in

this device geometry is strain in the graphene or at the graphene-gold interface that develops in response to friction forces during the motion. These effects will be isolated and explored in future studies.

2.1.5 Discussion

The ability to move both metal and vdW layers within a device offers an unprecedented level of control and flexibility in both device function and experiment design. The mechanically reconfigurable devices we demonstrate enable experimental studies where structure and geometry are continuously tunable parameters. This allows for dense sampling of the device and heterostructure parameter space while keeping local disorder constant, something that is impossible to achieve with the conventional approach of fabricating multiple devices. Reconfiguration by sliding makes possible the modification of quantum confinement via moveable gate electrodes, as well as the continuous tuning of lattice interfaces in vdW moire heterostructures. Our demonstration of deterministic in situ sliding also introduces the possibility of dynamic structural studies, where time-varying modulations of the device geometry,strain, and interfacial moires induce electronic effects such as topological charge pumping [26–28] Last, the proof-of-principle sliding scanning probe experiments show a new approach to spatial mapping of local material properties at the extreme limit of proximity, i.e., direct atomic contact, as well as with the full flexibility of planar nanofabrication.

2.2 Materials and Methods

2.2.1 General Fabrication Techniques

The following techniques are universal to our device fabrication except when specified otherwise.

Lithography

All lithography performed is electron beam lithography (EBL) using a PMMA resist. We use PMMA 950 A5 spun at 2000 rpm for 2 minutes resulting in a ∼500 nm thick layer for depositions less than 300 nm in thickness and for etch masks. EBL patterns are written at 1.6 nA or 3.2 nA with 30 kV excitation. The PMMA is developed for 3 minutes in a cold mixture of 3:1 IPA:water.

1D-edge-contacts

1D-edge-contacts for our graphene encapsulated in hexagonal boron nitride (hBN) devices are written with EBL and developed before reactive ion etching (RIE) with 10 sccm of SF6, 2 sccm of O2, 30 W of RF power, at 100 mTorr for 30 s [29].Then 3 nm of Cr and ∼100 nm of Au are deposited at 1 Å/s in an electron beam metal vapor deposition system. Liftoff is performed by soaking the sample in acetone for 1-2 hours and agitating with a pipette.

Exfoliation and Dry Transfers

We exfoliate hexagonal boron nitride and graphene from bulk crystals. Stacks are assembled using stamps consisting of PC film on a PDMS square on a glass slide [30].We have used

hBN ranging from ∼15 nm to ∼230 nm thick as a substrate for sliding gold structures.

2.2.2 Friction Measurements

Fabrication for gold-hBN friction measurements

Gold-only squares for friction measurements are fabricated by spinning PMMA on a silicon chip of exfoliated hBN, writing squares using EBL, depositing 170 nm of gold, and lifting off in acetone.

AFM lateral friction measurements

To measure lateral friction we use the lithography mode of a Park Systems NX10 AFM and a Budget Sensors Tap300Al-G tip to manipulate gold on hBN in ambient conditions. First the top surface of the gold squares is measured using lithography set point mode with 100 nN of downward force and a dwell time of 8 s. The tip is then moved next to the gold square, lowered 100 nm below the top surface of the gold, and moved laterally, transverse to the AFM cantilever, and into the gold square at 10 nm/s. The lateral deflection voltage is recorded throughout the motion. Measurements were also made at 1 nm/s and 100 nm/s, and no dependence on speed was observed in this range. Care is taken for the motion to be through the center of mass of the gold in order to avoid rotation, and motions with rotation are excluded from our analysis. The squares are also oriented so their edge is perpendicular to the direction of motion. Note, that no permanent deformation of the gold is observed in AFM images taken after manipulations.

The regions before contact, during static friction, and during kinetic friction are identified to extract the average baseline voltage, average kinetic friction, and the peak static friction value respectively. We include some example linetraces to demonstrate the scales, and overall

appearance of typical linetraces (Figure 2.4. Although some traces do not exhibit the ideal lineshape, their kinetic and static friction values do not deviate from other traces. The exact mechanisms which cause non-idealities are not clear.

To measure force using the AFM, we assume a linear model where deflection voltage is related to the force on the cantilever as $F_{tip} = V_{tip}k/S$, where V_{tip} is the lateral deflection voltage of the AFM tip, k is the tip spring constant, and S is the AFM sensitivity.

The cantilever is simulated in COMSOL Multiphysics to determine its spring constant, referencing optical and SEM images for its dimensions [5].To simulate the spring constant a lateral force is applied 100 nm above the apex of the tip and the displacement at this position is determined, resulting in a force per distance displaced of k = 250 ± 10 N/m for our tip. The simulations are parameterized with respect to the cantilever dimensions in order to estimate an uncertainty for the lateral spring constant. The material used is single-crystal anisotropic silicon with the top of the cantilever as the <100> plane and the cantilever pointing in the <110> direction.

To determine the sensitivity, S, which is the ratio of the lateral voltage deflection to tip displacement, we take the slope of the static region of the deflection linetrace, when the tip deflects before the gold starts moving. This assumes that the lateral displacement of the AFM piezo stage is equal to the tip deflection during the static portion of the pushing. However, we expect the tip deflection to be less than the stage displacement due to other effects such as the elastic deformation of the gold, or due to the tip slipping as it comes into contact with the gold edge. Such effects are evidenced by non-linearity in the slope of the static region and by the variable sensitivities we observe for smaller squares. The net effect is that our approach will overestimate the displacement of the cantilever, which would result in our extracted forces providing an upper bound on the friction force. Due to the variable sensitivity we observe for smaller squares (1 μm^2 and smaller), we only use the 4 and 9 μm^2 linetraces to calculate an average lateral sensitivity of S = 27 ± 8 mV/nm.

Annealing gold on hBN

To test the effect of heat annealing, the gold squares on hBN are vacuum annealed for 30 minutes at 350 C in a tube furnace. Measuring their friction again, we see that the tip deflections decreased by ∼50%. AFM imaging shows that the grain sizes increased from ∼20 nm to ∼80 nm in diameter. This qualitative behavior is expected for polycrystalline materials, but it may also be the result of trapped contaminants escaping from the gold-hBN interface.

2.2.3 Quantum point contact device

QPC device fabrication

Our reconfigurable QPC device consists of a graphene strip encapsulated in hBN, with a local graphite back-gate on an Si/SiO_2 substrate. 1D-edge-contacts are added to the graphene and graphite back-gate. The moveable top gates are 170 nm thick gold-only deposited with long, flexible electrodes to allow the gates to be moved while maintaining electrical contact. The Au-hBN interface friction is relatively large for the top gates and flexible electrodes due to their large surface area. To avoid cutting the gates while attempting motions we cross-link 500 nm tall PMMA rectangles onto the gates (Figure 2.7a). These tall features provide more surface area for the AFM tip to push into in order to move the top gates. Although they still deform from manipulations they serve as a sacrificial handle. We dose the PMMA with 15000 $\mu C/\mu m^2$ at 30 kV and 3.2nA in order to cross-link it. A small, isolated square of gold is also deposited onto the hBN (at the same time as the gold-only top gates), in order to sweep contaminants from the hBN surface, seen in Figure 2.7b.

To determine the QPC constriction width we measure the top gate separation using AFM. Due to the height of the top gates, the separation at the base of the gate differs from what

is observed using a standard AFM tip. To account for this we measure the sidewall profile using an ATEC-NC cantilever and subtract that from what is measured with our standard tips, referencing features on the top surface of the gate.

The graphite back-gate for our device is smaller than the graphene. This is so the 1D-edge-contacts to the graphene don't short to the back-gate. We refer to regions of the graphene which are not gated by the graphite as the graphene contacts, and they are doped to a higher carrier density by the silicon back-gate.

QPC measurement details

The resistance data was taken in a four-probe configuration by measuring the current at the drain electrode via a Femto current preamplifier (1E6 V/A gain) and the longitudinal voltage drop with a SR830 lockin amplifier using low frequency lockin techniques.

Before performing the 2D gate sweeps, we hole-dope the graphene contacts by biasing the silicon back-gate with -45 V corresponding to a filling factor of $\sim$7 at 9 T (nominal 285 nm SiO_2 thickness). For this reason, when both the dual-gated region and back-gated region are electron doped the device is unable to effectively transmit quantum hall edge modes across the resulting pn-junction, and it appears insulating as evident in the upper right corner of each conductance color plot in Figure 2.2e-h of the main text.

2.2.4 *In-situ* sliding

Metal handle and flexible serpentine electrode fabrication

To fabricate the "thick" metal handles and flexible serpentine electrodes for *in-situ* sliding, much thicker PMMA than normal is used: 950 A11 spun at 4000 rpm for 5 s, then 2750 rpm

for 2 minutes. This produces a film of PMMA that is ∼2.25 µm thick. EBL is performed using our standard parameters described in the general fabrication technique section. The metal deposition consists of 80 nm Au, 10 nm Cr, 1 µm Cu, 10 nm Cr, and 50 nm Au, all at 1 Å/s except for the copper which is deposited at 3 Å/s. The bottom layer of gold is for low friction with the hBN substrate, the top gold protects against oxidation, and the chromium acts as a sticking layer between the gold and copper.

1 µm and 500 nm flexible serpentine electrode widths were tested and we find that 500 nm width electrodes are more flexible, but also more fragile. Both work well for manipulation but we prefer the 500 nm due to the decreased interface area and hence reduced friction. We have also fabricated 1 µm and 500 nm width "thin" serpentine electrodes which are 150 nm tall gold-only instead of the thick multilayer metal combination and find that the 500 nm width electrodes are quite fragile in this case and can break more easily.

Typical metal handle donut dimensions we use have a nominal inner diameter 3 µm and an outer diameter of 9 µm. The C-shape is to help with liftoff as well as to add compliance in being stretched open upon press-fitting with the AFM tip.

In-situ manipulation technique

Before performing *in-situ* manipulations using our metal handles, we first flatten a 100 N/m, 1200 MHz MicroMasch 4XC AFM tip in order to increase the tip-handle contact area. This is carried out by oscillating the tip back and forth and side to side while in contact with the SiO_2 of our sample until it is >3 µm wide, slightly larger than the inner diameter of the donut. We choose this tip for its high force constant and the protruding "tip view" style which makes it easier to align with the donuts.

In general, our technique for performing *in-situ* manipulations involves the sample with a metal handle donut mounted on a XYZ piezo scanner that engages into a stationary flattened

AFM tip. This process is carried out by first aligning the donut with the tip and raising the piezo stage. The stage is raised until the donut contacts the tip as determined by optically observing a change in the light reflected off the cantilever (seen through a 20x objective). After the initial contact, we press-fit the tip into the donut by raising the stage further. At room temperature we engage the donut into the tip by ∼1.5-2.5 µm to achieve a rigid connection with the structures shown in Figure 2.3c of the main text. In higher friction situations, such as for larger objects or at cryogenic temperatures, engaging more than ∼2.5 µm, corresponding to a larger downward force of the tip on the donut, is necessary to reduce the slippage between the tip and donut and to achieve deterministic, one-to-one sliding motions. For the sliding done at 7.6 K, we engaged ∼5 µm as opposed to ∼2.5 µm at room temperature to get a similar one-to-one deterministic motion. When finished, the tip can be removed by lifting it from the donut, which results in a slight lateral motion.

Room temperature manipulation setup

Room temperature *in-situ* sliding experiments, including the scanning top gate and the sliding graphene "hockey puck" heterostructure, were performed at ambient conditions. The setup consists of an AFM tip glued to a glass slide, mounted on a coarse manual XYZ stage and the sample/chip carrier mounted on a Thorlabs 3-axis NanoMax open loop piezo stage. A Mitutoyo VMU microscope with 20x and 2x objectives is used for optical imaging. In both the room temperature and cryogenic manipulation setups, nanomanipulation is performed using the piezo positioners, which are brought into range by coarse screw-based positioners.

Cryogenic manipulation setup

Cryogenic manipulations are performed in a continuous flow Janis ST-500 optical cryostat, using the same microscope as for the room temperature manipulation setup. The ST-500

is cooled using a Janis helium recirculation setup and achieves a sample temperature of 7.6 K. The sample is mounted on an Attocube ANSxyz100std/LT piezo scanner (with 55 µm of XY range and 25 µm of Z range at ∼4 K), and the AFM tip is mounted to a custom flexural positioner for coarse positioning at room temperature (Figure 2.9). Accounting for thermal contraction, the tip is coarsely positioned at room temperature so that it will be within piezo scanner range of the sample once at base temperature.

Sliding "hockey puck" heterostructure

We fabricate our encapsulated slidable graphene "hockey puck" device by transferring ∼200 nm thick top hBN onto monolayer graphene, writing rectangular PMMA etch masks, and etching with SF_6 and O_2 (same recipe as 1D-edge-contacts) to leave behind rectangles of hBN on graphene. We then write and deposit 150 nm gold-only "wrap-around contacts" which provide edge contacts to the graphene. The thick top hBN and "wrap-around-contacts" add mechanical support to prevent buckling and provide a rigid grip to hold the "hockey puck" heterostructures together while it is translated. The "hockey pucks" are picked up using a PC/PDMS stamp and transferred onto a large bottom hBN substrate before writing and depositing thick flexible electrodes and donuts in order to electrically contact and manipulate them *in-situ*. Of the five "hockey puck" devices we attempted to transfer and electrically contact, all but one were successfully contacted (Figure 2.10f).

Two-probe resistance measurements were performed by current biasing and measuring the voltage drop across the device to determine the resistance. The resistance versus displacement trace was measured by displacing in 10 nm steps and then recording the resistance after a short pause. In the main text we refer to the full forward and backward measurement sequence as a single "motion". Each motion takes about 30 seconds. A video of the motions was recorded, and a light source illuminated the sample during all of the measurements. In addition, all measurements were performed with the silicon back-gate grounded.

In Figure 2.3d of the main text, the zero position corresponds to the initial transferred position of the "hockey puck", before any motion. After being transferred and contacted, the device was slid to the leftmost position, at about −275 nm, before the subsequent 1.2 µm back-and-forth motions.

Scanning top gate device

The scanning top gate device was fabricated by encapsulating graphene in hBN and 1D-edge-contacting it. For this device, the "thick" metal top gate serpentine electrode structure was initially written and deposited on a separate SiO_2 chip and then picked up and transferred onto the completed graphene device using a PC/PDMS stamp. This electrode was transferred to a position so that one end overlapped with a previously written Cr/Au contact which provided the electrical connection to the top gate as well as a high friction anchor point (Figure 2.11).

Two-probe resistance measurements were performed in an identical manner to the sliding "hockey puck" device described earlier with the addition of 2 dimensions of motion. The fast scan direction was perpendicular to the graphene channel. The top gate voltage was held at zero volts for the data presented in the main text.

2.3 Supplemental Information

2.3.1 hBN-graphite friction

We measure several flakes of hBN on graphite and see that while the friction for 6 μm^2 flake matches very well for the same sized gold square, larger hBN flakes on graphite exhibit similarly low friction and hence indicate a sub-linear scaling with area, unlike the polycrystalline gold on hBN (Figure 2.5). This is expected since the hBN flakes are single crystal and exhibit superlubricity [4, 7].The hBN flakes measured are 20-50 nm tall, much shorter than the 170 nm tall gold squares, so to manipulate the thin hBN flakes, the height of the underlying graphite substrate is measured with 100 nN downward force. This sets the AFM tip height for the lateral motion. We find that using this height setting does not result in the tip touching the graphite substrate during manipulation.

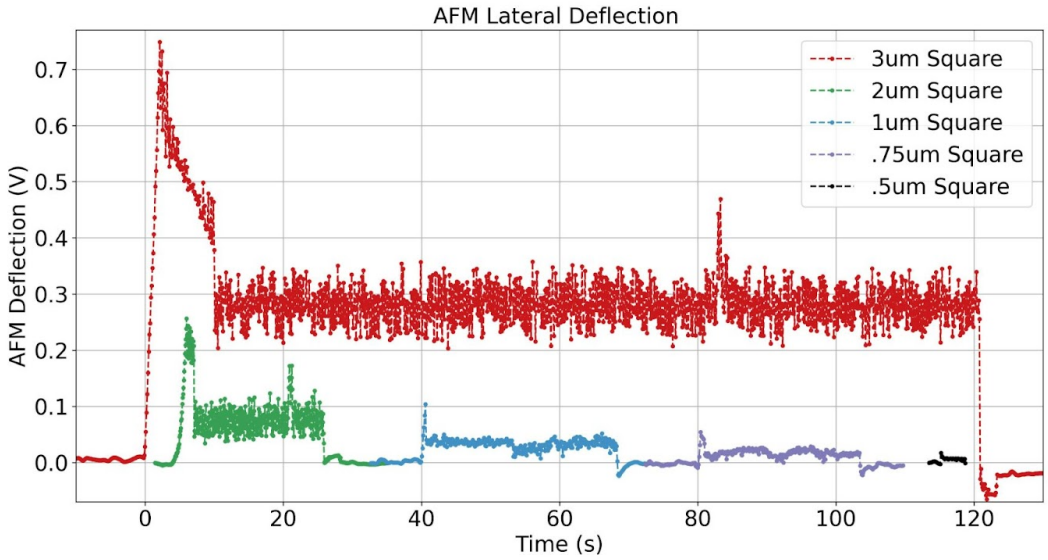

Figure 2.4: Example AFM deflection linetraces for various sizes of gold squares on hBN.

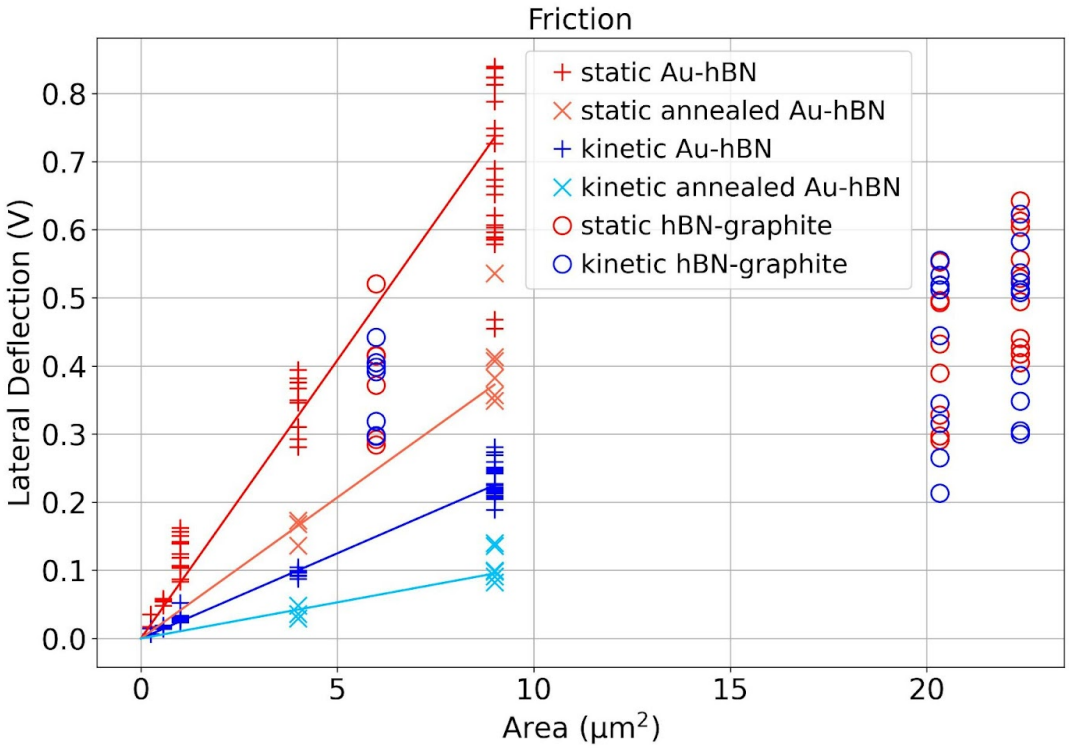

Figure 2.5: All static and kinetic deflection values for gold-on-hBN and hBN-on-graphite extracted from linetraces.

Friction forces per unit area for Au-hBN are: static 0.762 ± 0.232 MPa, static annealed 0.386 ± 0.117 MPa, kinetic 0.233 ± 0.07 MPa, kinetic annealed 0.099 ± 0.031 MPa. Fits are through zero and only include 4 and 9 μm^2 data points.

2.3.2 Cr-Au friction on hBN

When moving small pieces of 3nm Cr + 100 nm Au on hBN, we have found their static and kinetic deflection voltages to be roughly an order of magnitude higher than the same sized annealed gold-only square on hBN.

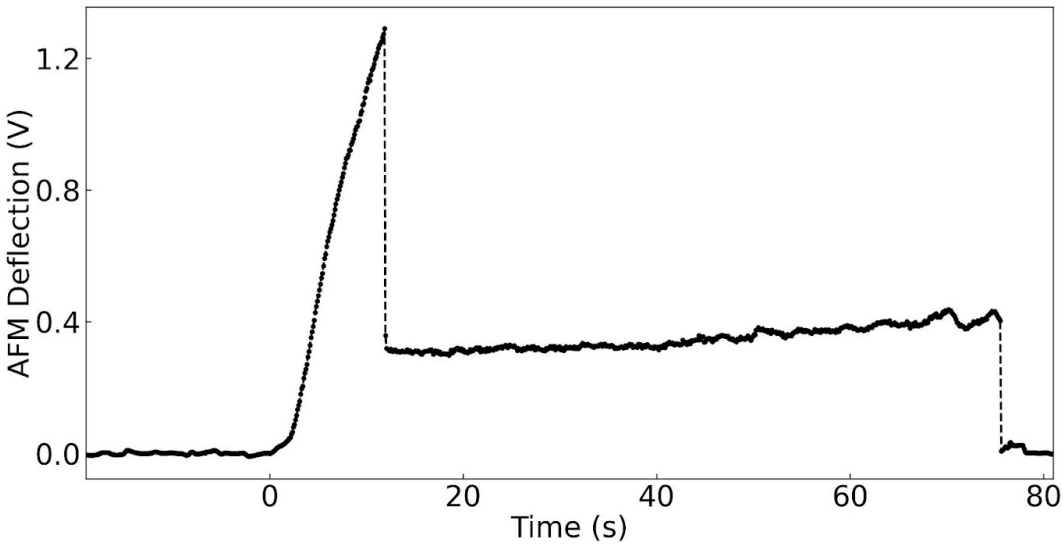

Figure 2.6: Voltage deflection for 2 µm x 2 µm, 100 nm thick gold + 3 nm Cr sticking layer square on hBN.

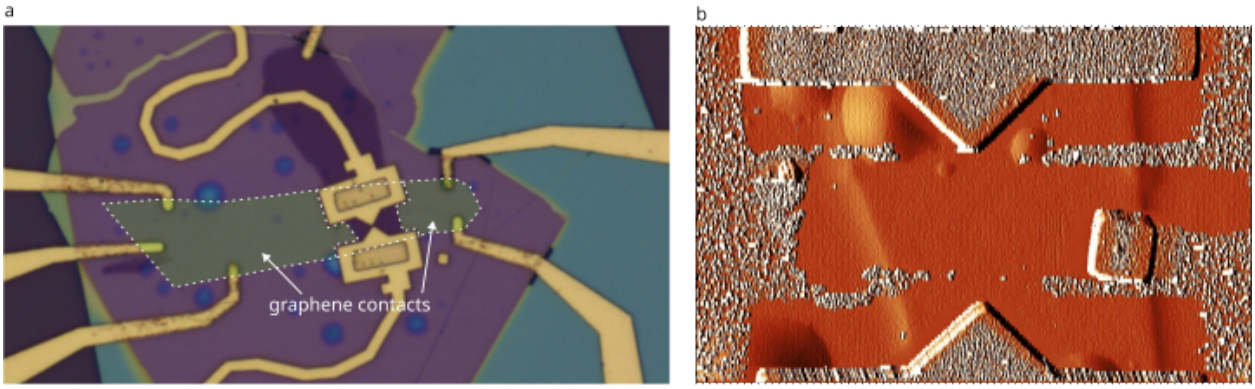

Figure 2.7: Images of mechanically reconfigurable quantum point contact device **(a)** 100x optical image of completed QPC device after finishing first set of gate manipulations to achieve a desired gate separation. Graphene flake is outlined and graphene contact regions highlighted in green reside in regions where the carrier density is determined only by the silicon back-gate. **(b)** AFM amplitude data taken zoomed in on the QPC gates showing the cleaning process. A gold square is swept back and forth between the QPC gates to remove surface contaminants from the sensitive QPC region prior to positioning the QPC gates to a desired separation.

2.3.3 QPC conductance map kink

The kink feature observed in Figure 2.2e-h near zero top gate voltage is a result of our top gates extending to the graphene contacts providing a parallel conduction path which is different from other QPC studies. This aspect is not important to the operation of the QPC which only exists for $\nu_d \leq 0$.

2.3.4 QPC contact resistance

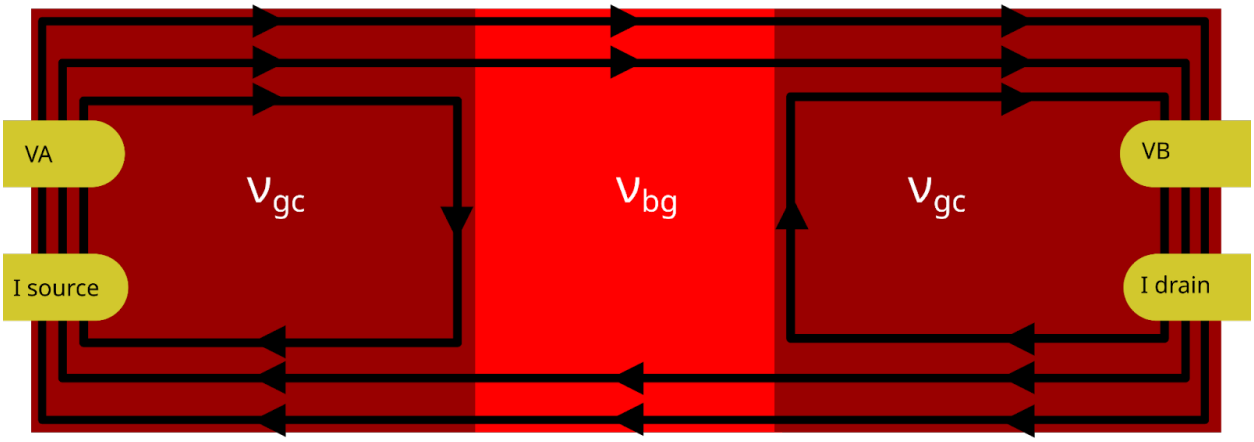

Figure 2.8: Three hole-doped quantum hall regions in series.

Electrodes in yellow are set up in a four-probe configuration, identical to the measurements for the QPC device. ν_{gc} is the filling factor of the graphene contacts and ν_{bg} is the filling factor of the graphite back-gated region where $|\nu_{gc}| > |\nu_{bg}|$.

Due to the graphene contacts being in series with the QPC constriction, the measured resistance is a sum of the QPC constriction resistance and the graphene contacts resistance RC. This constant resistance RC is subtracted from the measured value to calculate G_{QPC} which is presented in Figure 2.2 of the main text. RC was determined by fitting the value of the widest plateau in Figure 2.2d to a conductance of 2 e^2/h, which we ascribe as an effective

$\nu_{qpc} = -2$ at the QPC constriction point. Note that the graphene contacts support their own quantum hall edge states, generally at a different filling factor than the back-gated and dual-gated regions. In a four-probe longitudinal resistance measurement between a network of different quantum hall regions with different filling factors, one can measure effective positive and negative contact resistances as outlined below. For the largest separation, we measured a net positive contribution to the contact resistance and for the three smallest separations we measured a net negative contribution. The contact resistance values used are R_C =(+1580, -3000, -2920, -2800 Ω) for the QPC separations of 1110 nm, 170 nm, 120 nm, and 10 nm respectively.

A positive contribution to RC can be understood due to disorder causing forward moving edge modes to backscatter to backward moving edge modes and vice versa. Bubbles formed between the layers during the stacking process are a source of disorder in our device and can be seen optically or in our AFM images in the graphene contact regions.

As an example of how one can measure a negative contribution to R_C with our contact configuration, consider the scenario depicted in Figure 2.7 with three quantum hall regions in series with filling factors from left to right ν_{gc}, ν_{bg}, and ν_{gc} where ν_{gc} is the landau level filling factor of the graphene contact regions. Assuming both ν_{gc} and ν_{bg} are negative (as is the case for operating the QPC), the magnitude of $|\nu_{gc}| > |\nu_{bg}|$, and full equilibration of the quantum hall edge modes, one can derive the following equations: defining $R_{AB} = V_{AB}/I$, then $R_{AB} = R_{bg} - R_{gc}$ where $R_{bg} = h/(\nu_{bg}e^2)$ and $R_{gc} = h/(\nu_{gc}e^2)$.

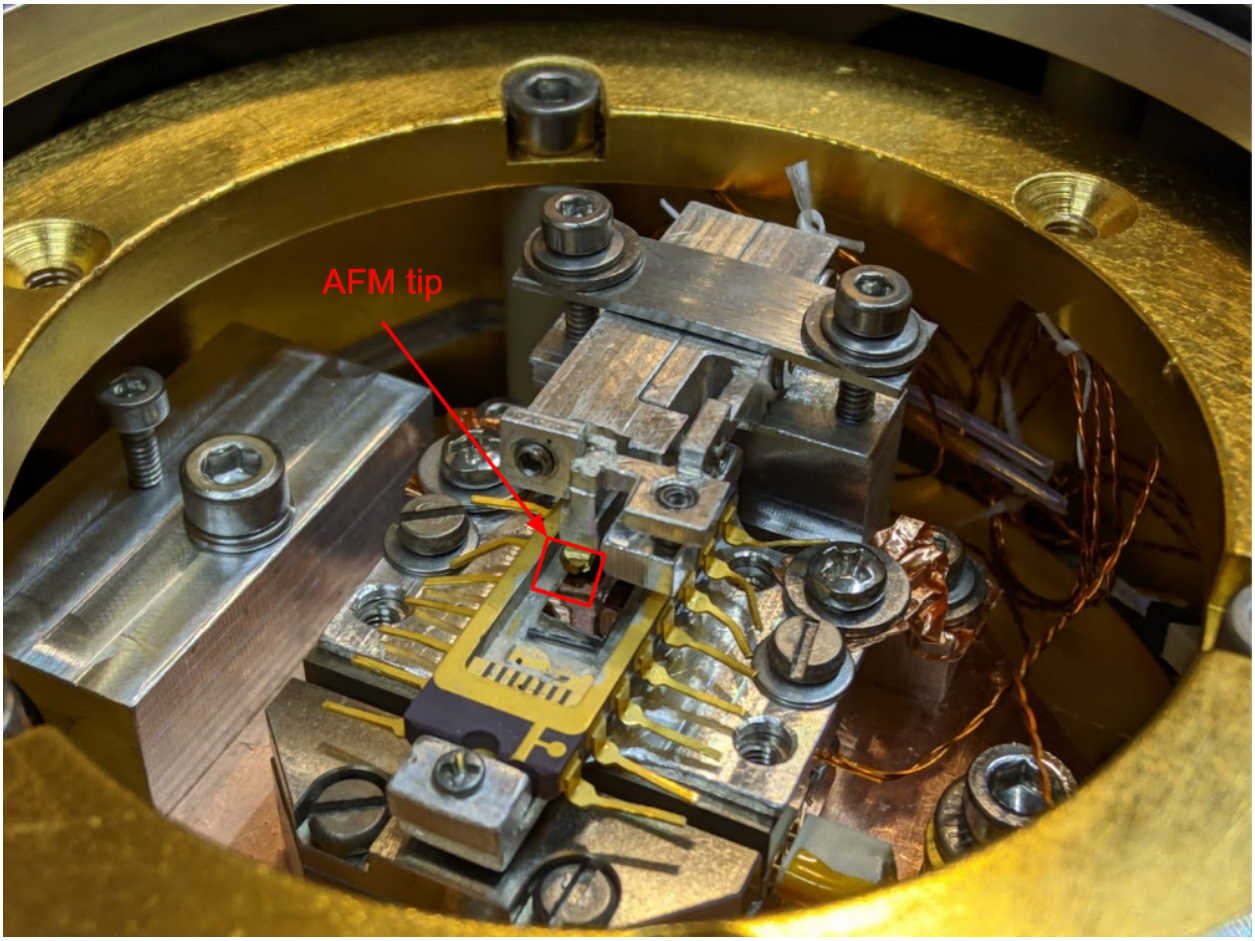

Figure 2.9: Custom build cryogenic manipulation setup

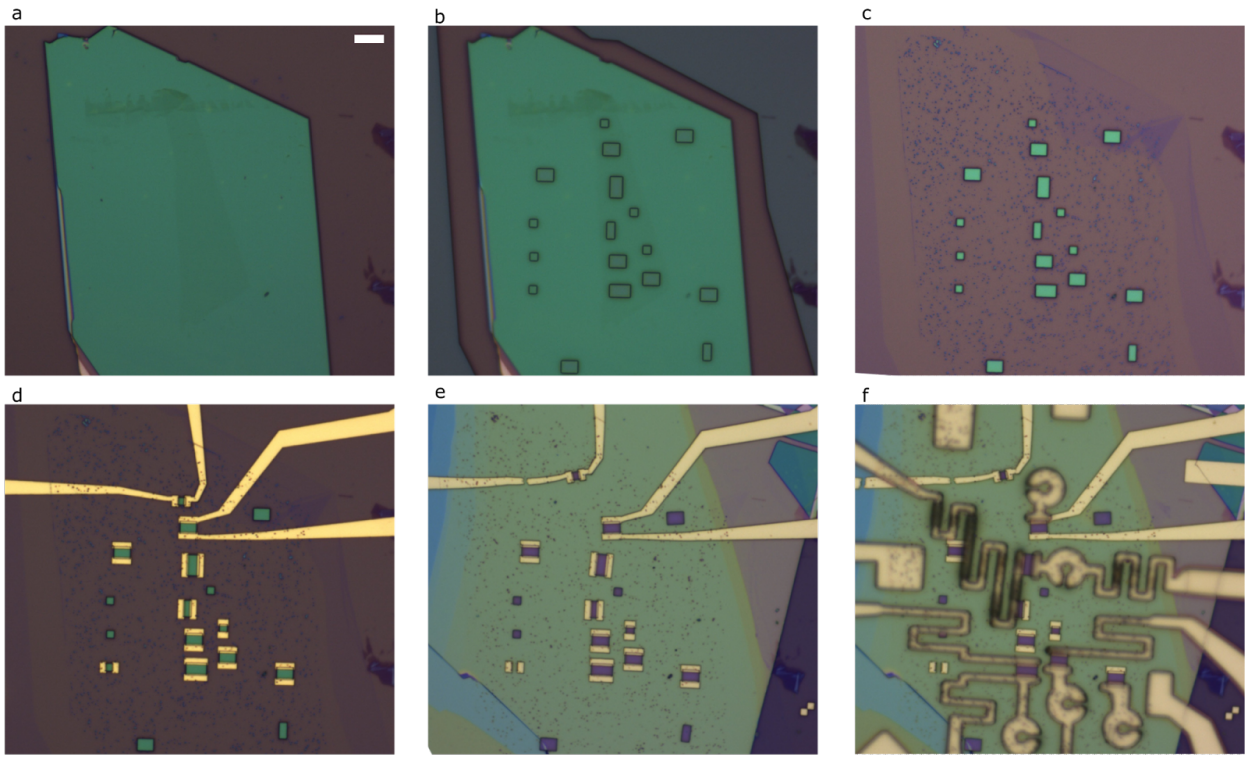

Figure 2.10: Optical images of hockey puck device fabrication.

The scale bar in **(a)** is 3 µm and applies to all images. **(a)** hBN transferred on top of graphene flake on SiO_2 substrate. **(b)** Developed PMMA etch mask written over regions of hBN with and without graphene beneath. **(c)** hBN and graphene etched using SF_6 and O_2. **(d)** 150 nm gold-only wrap-around contacts deposited. **(e)** Hockey pucks and contacts transferred onto bottom hBN flake. **(f)** Thick metal handles and flexible serpentine electrodes deposited. The metal donut is out-of-focus because it is ∼1 µm thick, but it is still in good contact with the hBN.

Figure 2.11: hBN-encapsulated graphene device with transferred scanning top gate serpentine electrode, donut inner diameter is 3 µm.

Movie S1. Gold sliding on hBN at 7.6 K Motion amplitude is approximately 10 µm vertically, 10 µm horizontally, and 14 µm diagonally.

Movie S2. Gold accordions longitudinal sliding at 3 Hz on hBN at room temperature Oscillation amplitude is approximately 2 µm.

Movie S3. Gold accordions transverse sliding at 3 Hz on hBN at room temperature Oscillation amplitude is approximately 2 µm.

Movie S4. Encapsulated graphene hockey puck *in-situ* sliding and measurement Measurements performed at room temperature with an amplitude of motion is 2.4 µm. Resistance data is collected every 10 nm.

Chapter 3

Mechanically reconfigurable van der Waals devices via low-friction gold sliding: Additional details

Some *garbage is ok.* - Hannibal Buress

3.1 AFM Z Scan drift

The Z Scan and Z Drive of the AFM output a height which is directly proportional to the voltage applied to the piezo. They are different from the Z Height channel which takes data from a separate sensor to measure the Z position of the tip. As a result, the Z Scan and Z Drive channels can differ significantly from Z Height. This is particularly noticeable when using Z Scanner mode in Lithography mode. The AFM software (in its current version SmartScan 2.0 RTM2) allows the user to specify the Z Scanner position (based on this piezo

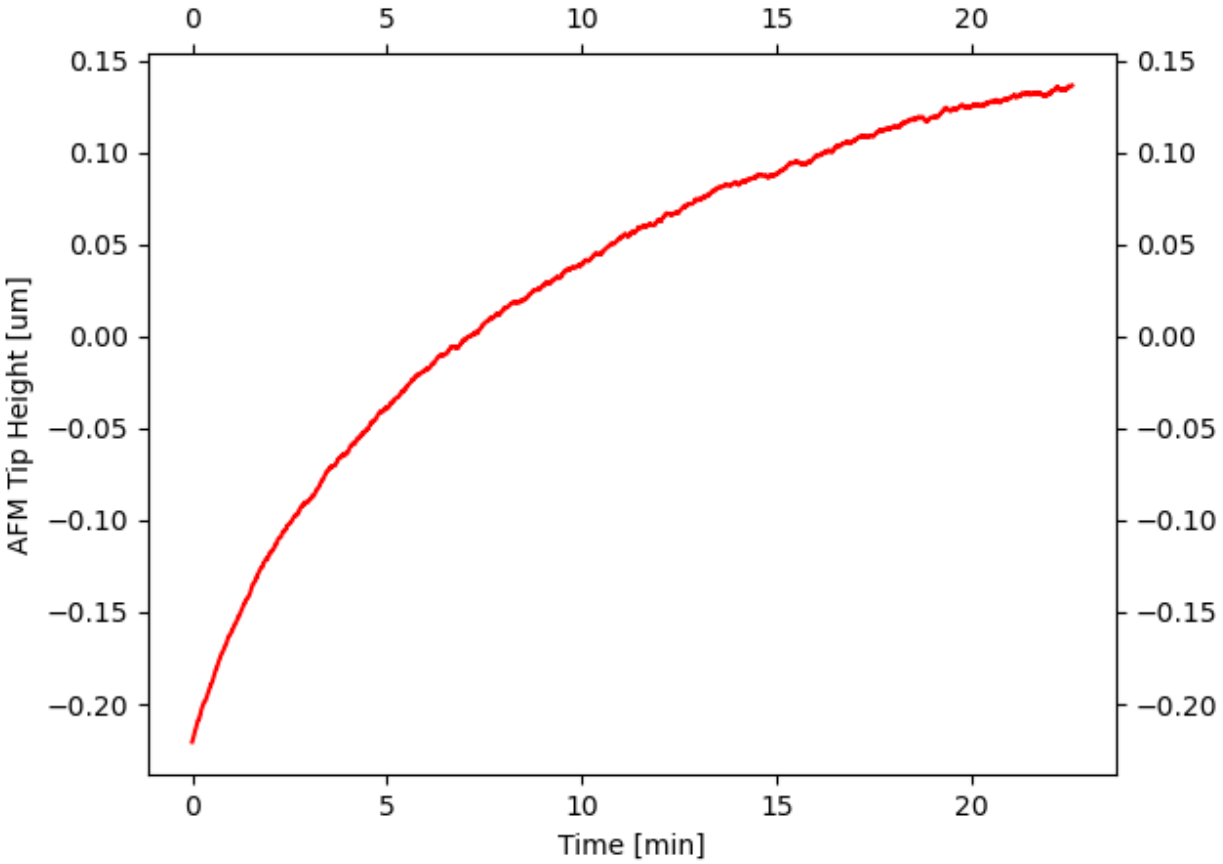

Figure 3.1: AFM Z Scan versus time
Taken immediately after approaching in Tapping mode. This illustrates the piezo charging effect.

voltage scaling). It doesn't use the Z Height sensor.

Additionally, the Z Scan value changes over time, especially immediately after approaching, see Figure 3.1. I suspect this is due to some kind of charging/capacitance effect when a very different voltage is applied to the Z piezo. As a result, when measuring the height of the sample in order to use Z Scanner mode for a manipulation, the measurement is performed with an 8 s dwell time. Using this dwell time results in a height value which is ∼10-20 nm above the sample surface, and doesn't result in scratching the sample for µm-scale manipulations. Ideally, Park would update their Litho Mode to allow the user to input a Z Height position, which would make vertical positioning much easier and more accurate.

3.2 AFM before/after annealing Au

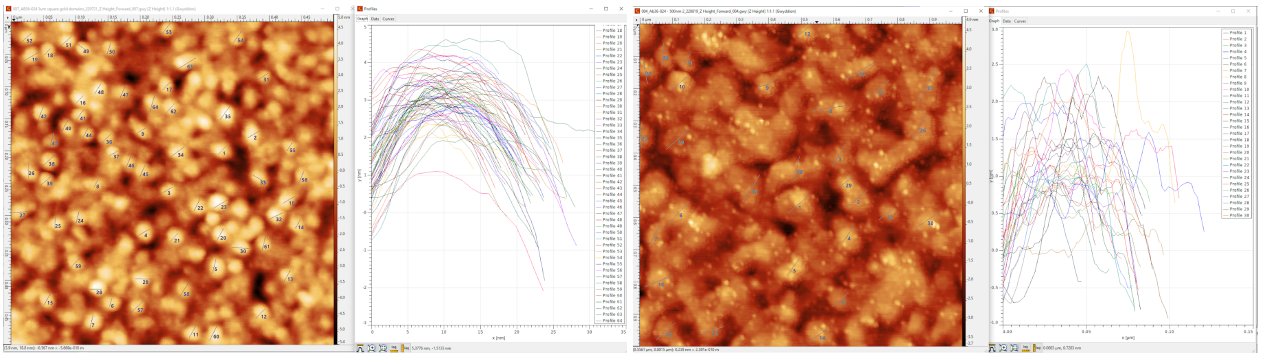

a b c d

Figure 3.2: Au grains before and after annealing

A: Before annealing **B:** Profile of marked grains **C:** After vacuum annealing at 350C for 30 minutes **D:** Profile of marked grains

3.3 COMSOL tip simulation

I created a model of the tip in COMSOL, first very crude and over time I added more detail to better reflect the tip appearance as seen in SEM/optical images (Figure 3.3). It is possible to import geometry from Solidworks and probably from other 3D CAD software as well, but creating the geometry in COMSOL allows you to more easily parameterize your simulations in order to rapidly simulate variations on a geometry. The downside is that creating a geometry in COMSOL is less intuitive than Solidworks.

For the tip spring constant simulation I used a stationary simulation and applied a force to the tip. I then measured the displacement at the location of the applied force and from that calculated the spring constant. Since we can easily measure the tip frequency in the AFM, I also performed an eigenfrequency simulation which helped confirm the simulation accuracy. Additionally, the out-of-plane spring constant can be used to corroborate the simulation.

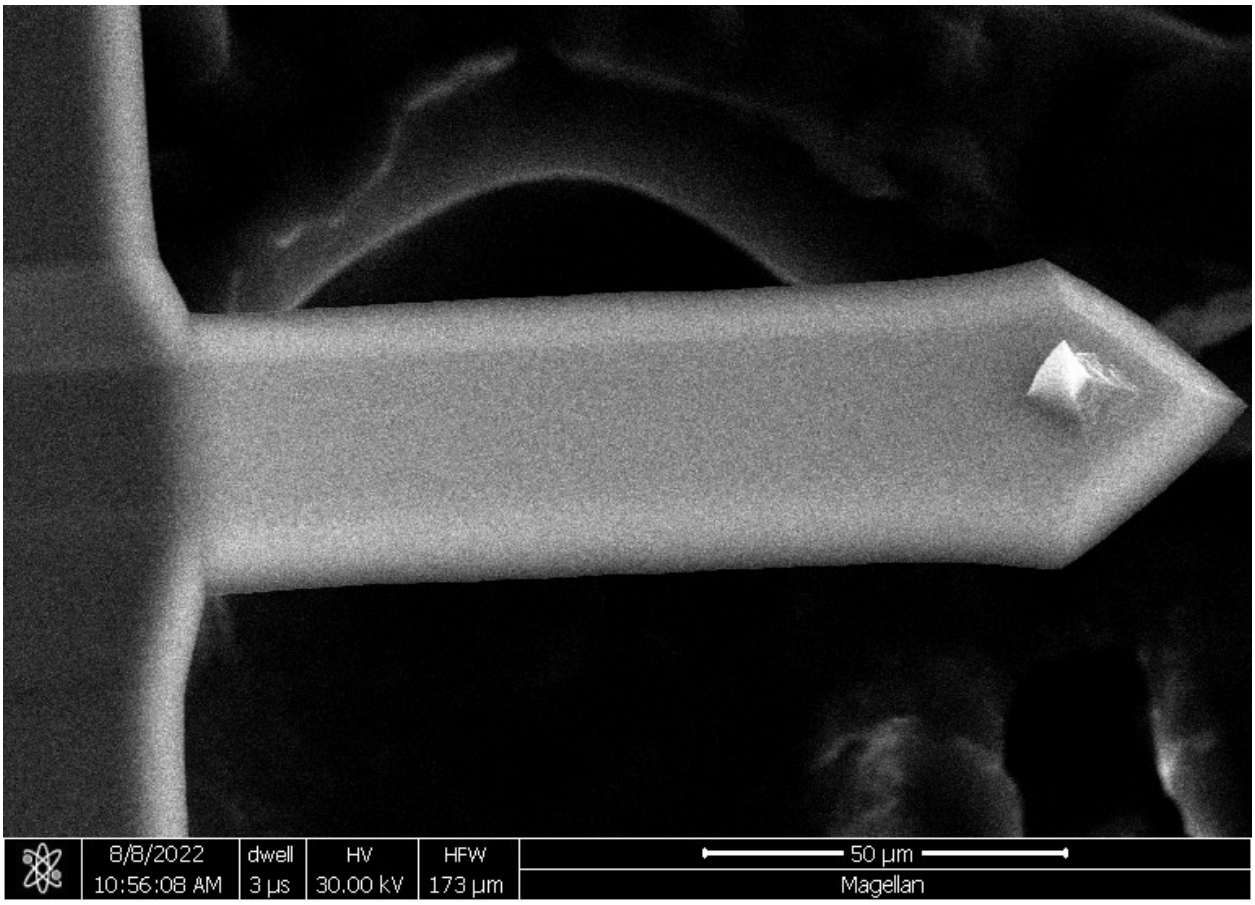

Figure 3.3: SEM image of Tap 300 cantilever

While simulating the spring constant and resonance frequency in COMSOL is very straightforward, a great deal of time was spent in generating the mesh in an intelligent way. A mesh that is too coarse won't produce accurate results, and one too fine will take too long to run, especially if you are parameterizing the simulation.

Because the tip tapers to a very small size, the mesh must get quite small as well too. For this reason it is useful to use different mesh in different areas with larger or smaller sizes. It can also be incredibly helpful to set custom maximum and minimum element size, growth rate, and resolution at narrow regions. For the pyramid of the tip that allows the base to be larger mesh and the apex to be smaller. For other simulations I have done, such as for electrostatic simulations of thin metals, regions where you know the important physics is

happening, such as at certain edges or surfaces, should be set to finer mesh as needed. If you see any behavior in your simulation with the same size as the mesh, that is a clear sign to increase the resolution.

With regards to an AFM cantilever, initially one might assume that the softness of the probe is primarily set by the cantilever dimensions and depends less on the tip pyramid, but this is not true for the torsional spring constant. This is apparent when considering that along its height, the XY dimensions of the pyramid are similar in size or smaller than the cross-section of the cantilever.

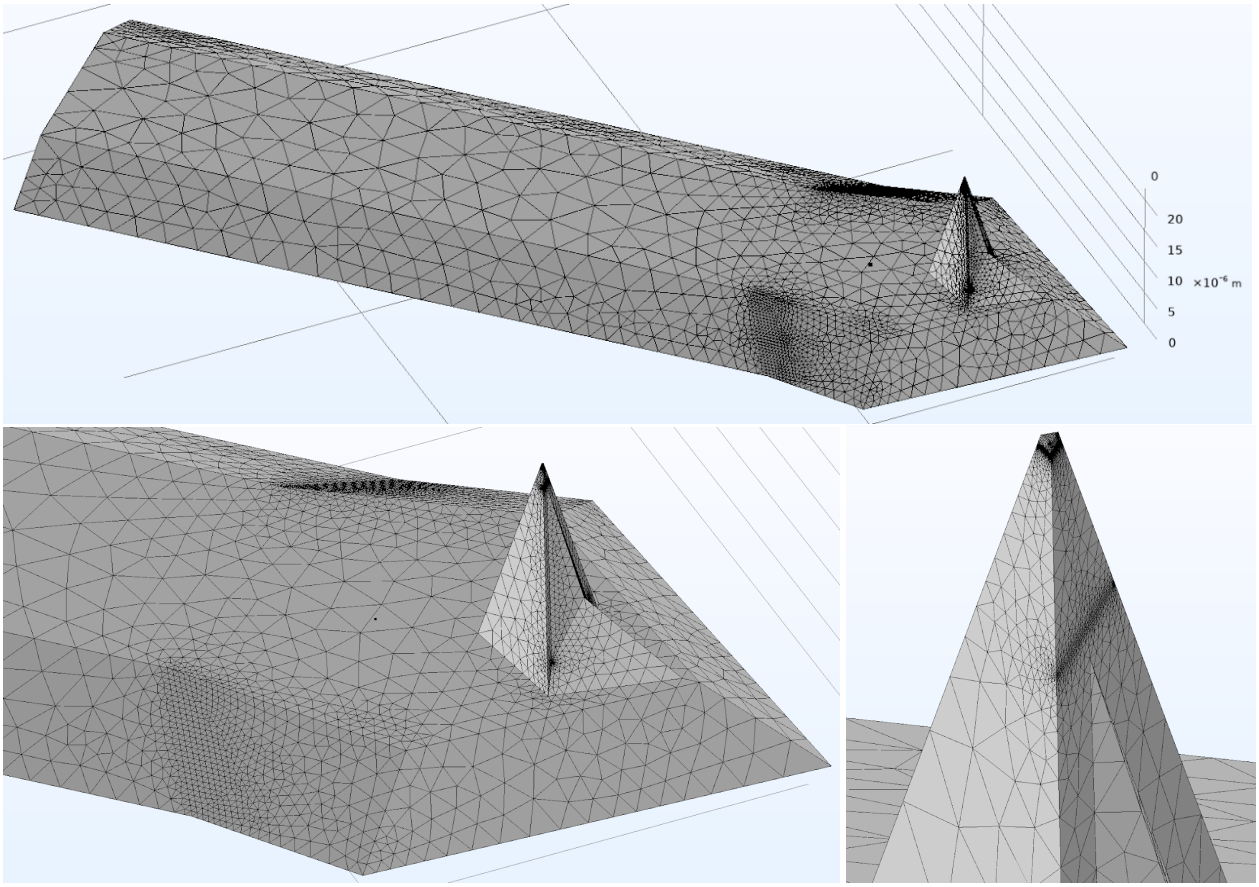

Figure 3.4: Tap 300 mesh in COMSOL

I also spent a decent amount of time working out how to best deliver a force to the cantilever. To distribute the force I applied the force to a thin area 100 nm from the apex of the tip.

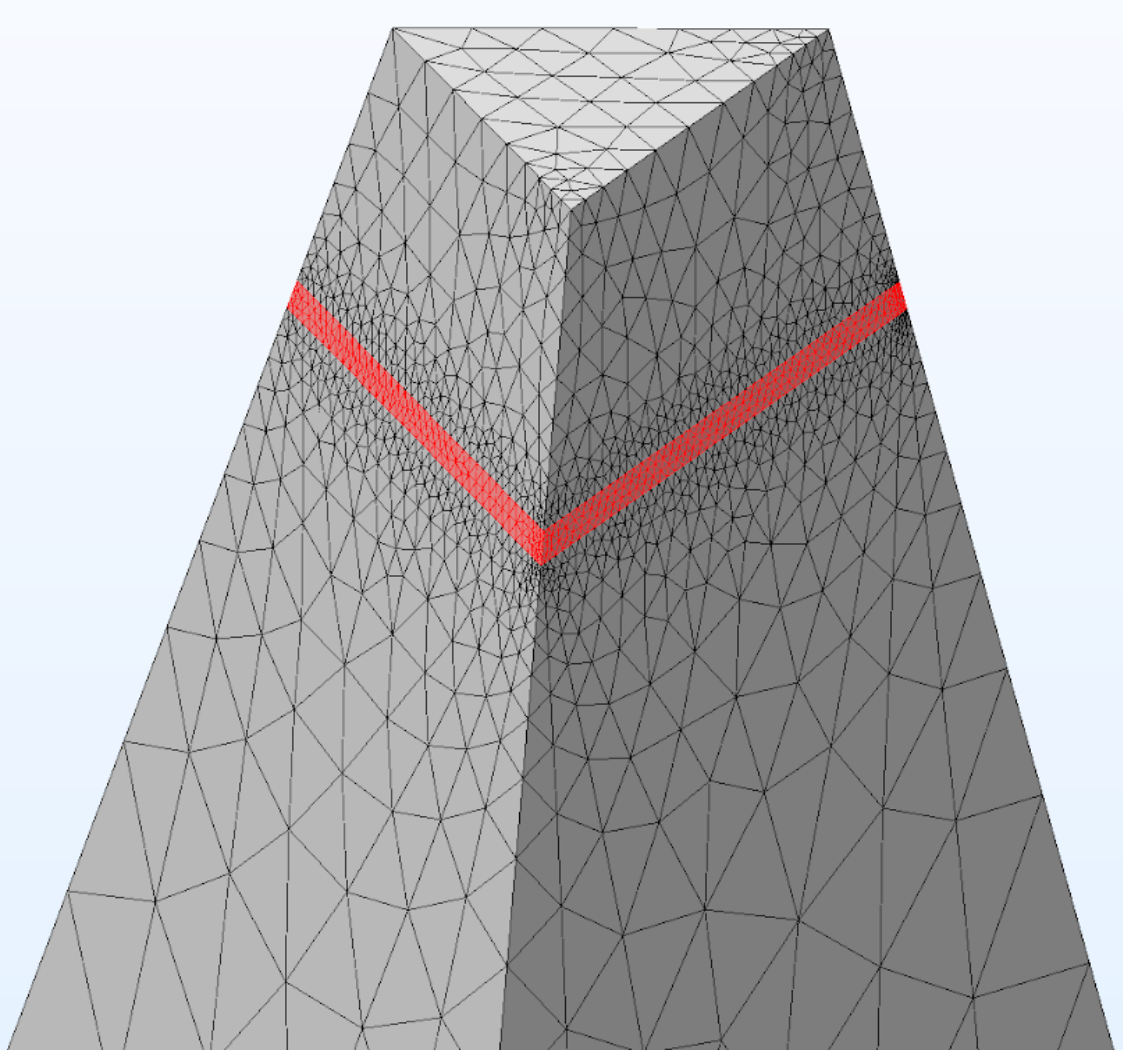

Figure 3.5: AFM Cantilever apex and pushing surface.

The force was applied to the left, red highlighted surface

To determine if the thickness of the area played a significant role in the measured spring constant, I parameterized it and got the thickness/spring constant combinations shown in Table 3.1. The difference in spring constant here is only ∼2% for very large percent changes in the thickness. So it is not particularly sensitive.

Tip push thickness (nm)	10	30	50
k (N/m)	209	205	201

Table 3.1: Tip contact area thickness effect on spring constant

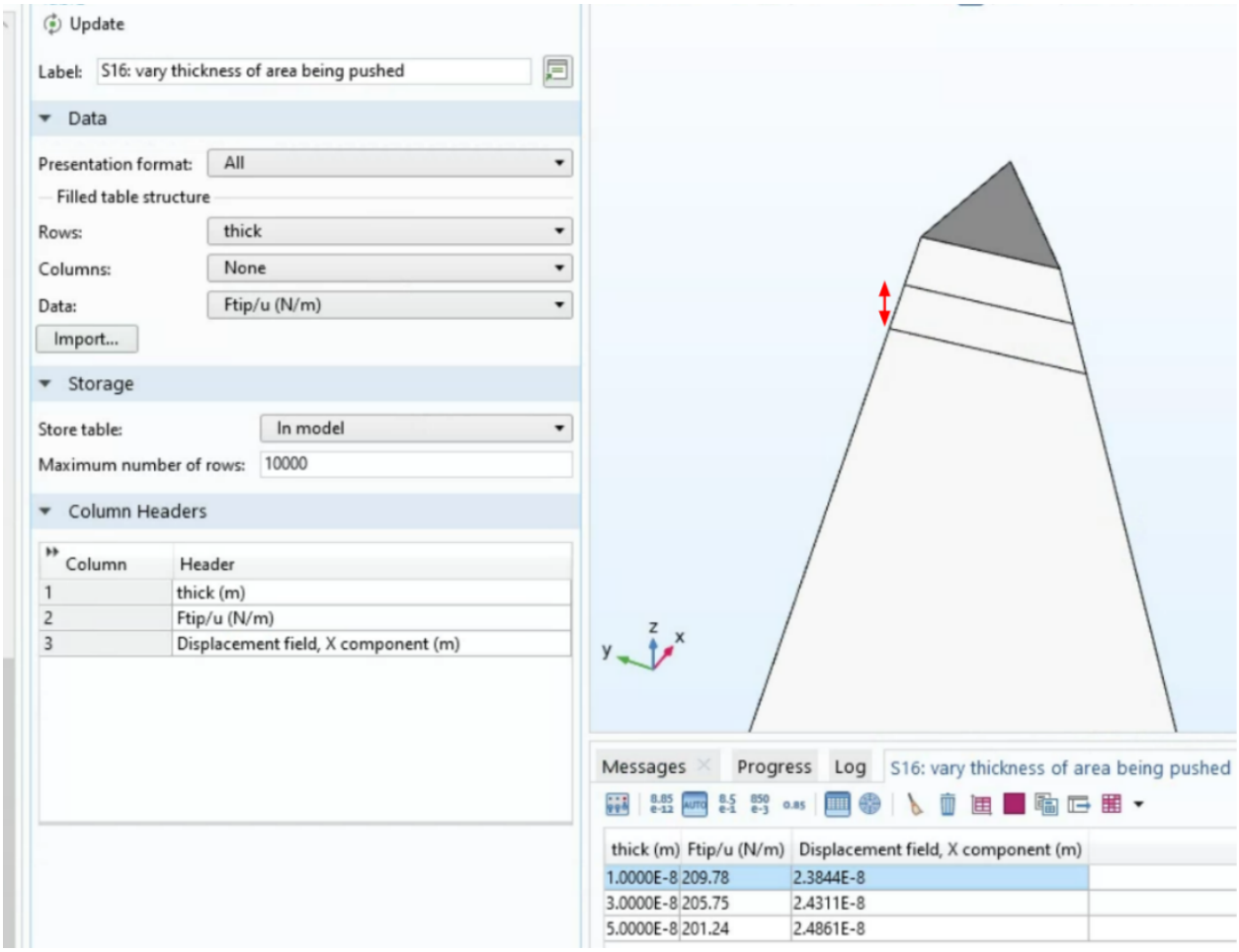

Figure 3.6: Thickness of push surface variation

Another consideration we made is that the sample, which is a gold rectangular prism, has some springiness itself and will deform and spring back when pressed into by the AFM tip. When pressing into such a gold rectangle with a 10x8 nm surface area, the spring constant approaches that of the cantilever, different by only a factor of ∼2. Here the contact area strongly determines the spring constant measured:

Contact dimensions (nm)	70x3000	70x100	20x100	10x8
k (N/m)	98	5588	2550	460

Table 3.2: Au contact area effect on spring constant

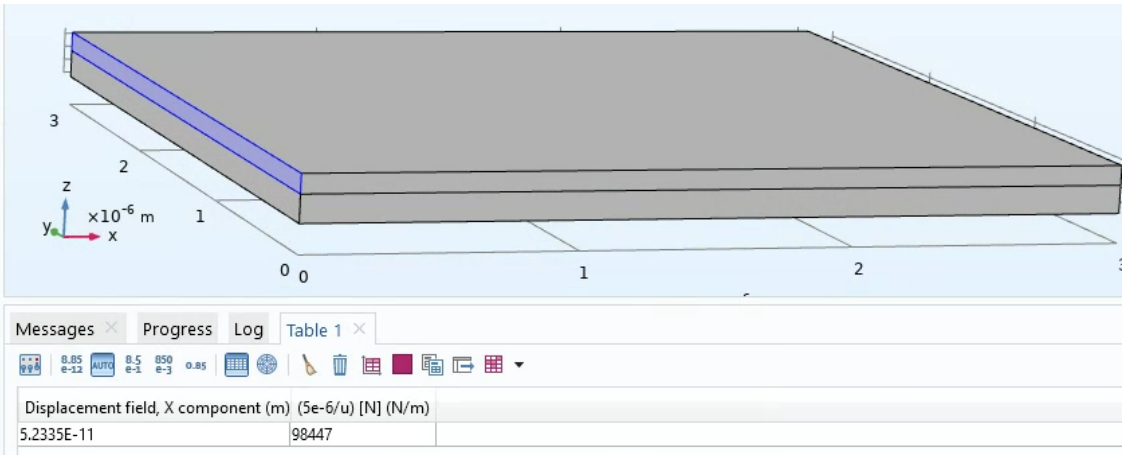

Figure 3.7: Simulation to test the spring constant due to pushing into soft Au rectangle

I also considered the height of the push from the apex. Minor variation in this parameter are also not critical as a 50% change only results in a ∼10% change in the spring constant. It's possible though that this is more sensitive for actual AFM tips, whose pyramid edges become more curved near the apex of the tip.

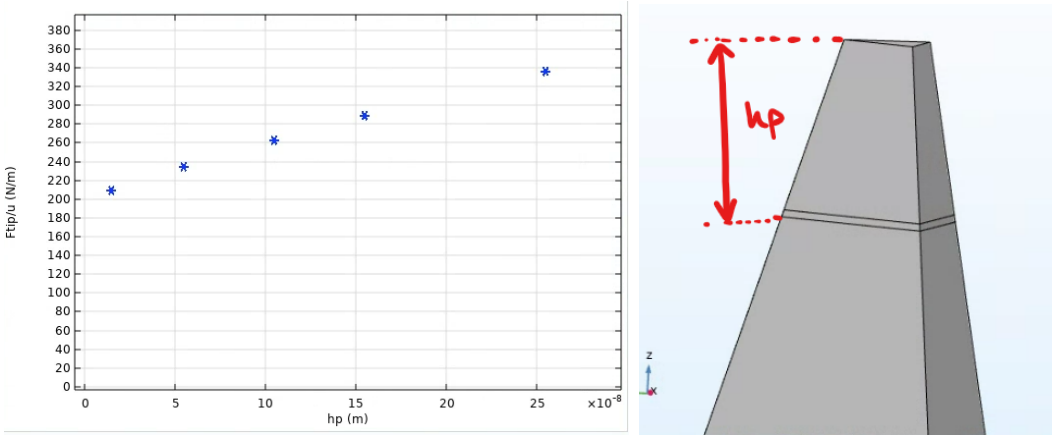

Figure 3.8: Cantilever spring constant vs height of push

In my initial geometry, I made the tip a simple triangular pyramid. This differs from the actual tips which have a much bulkier/wider base. To check how large of a factor this played, I simply ran the same simulation with certain sections of the pyramid set to be fully rigid. The elastic height refers to how much of the pyramid is treated elastically. 17 µm means the

Elastic height (µm)	17	7	1	0
k (N/m)	207	217	300	800

Table 3.3: Pyramid elasticity effect on spring constant

entire pyramid is elastic, 1 µm means that only the 1 µm closest to the apex is elastic and the rest of the pyramid is rigid. The data in table 3.3 suggests that while the base 10 µm of the pyramid is relatively rigid, the next 6 µm up plays a more significant role. This inspired me to more accurately represent the true pyramid shape.

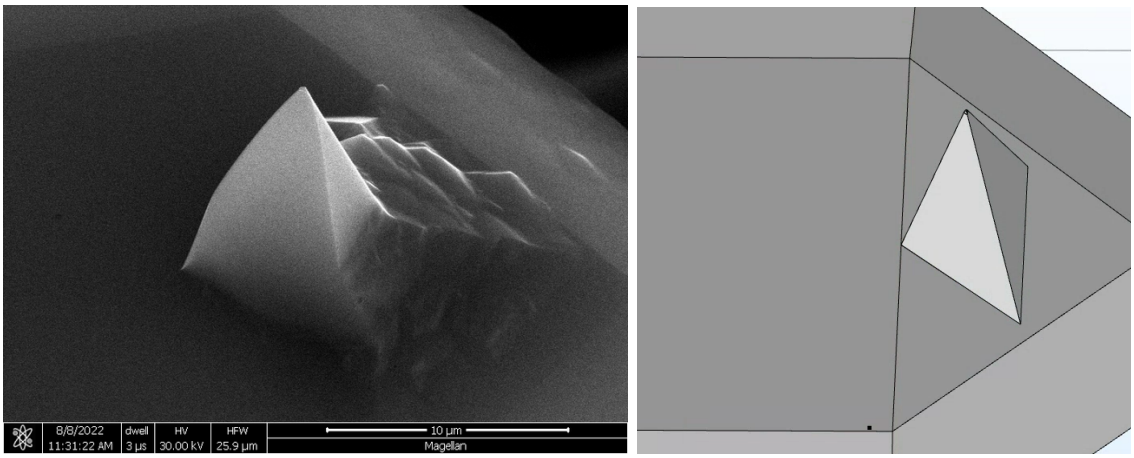

Figure 3.9: Tap 300 SEM image and initial simulated geometry

3.4 AFM tip torsional sensitivity

We determined the AFM-tip torsional sensitivity simply by taking the slope of the static friction signal for each lateral force friction measurement. While this is not the best way to make this measurement, it was much simpler than the most accurate method.

In Figure 3.10 I plot the sensitivity vs the static peak position for each trace. It is apparent that the 3 smallest square sizes have a different sensitivity than the 3 largest sizes. It is for this reason that only the 4 and 9 µm^2 data sensitivity values are used. The sensitivity is also quite different for G-BN. This may be due to the flakes being only ∼20-50 nm resulting in a

contact point much closer to the apex of the cantilever or due to different Young's modulus between gold and hBN.

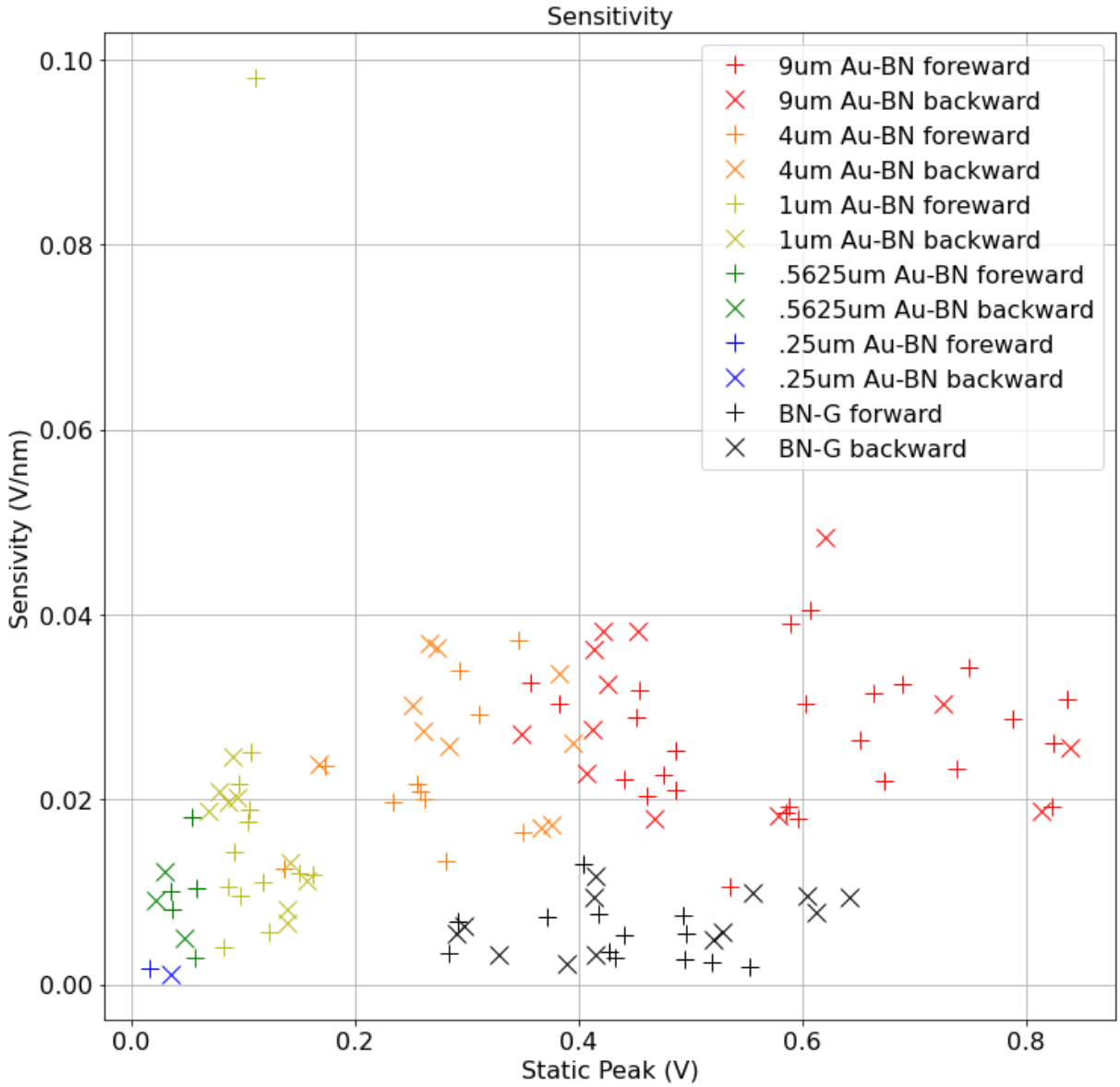

Figure 3.10: AFM tip sensitivity vs static friction peak.

Each data point is a single Au-hBN square friction measurement.

3.4.1 Stick slip motion

Throughout our manipulations we have periodically observed evidence of stick slip motion in the form of a sawtooth pattern in the friction signal. If the tip is moving quickly or the time-resolution is too low, then the signal will simply appear noisy. We have observed this for a variety of interface combinations: Au-hBN, graphene-hBN (with Au mask above), Au/Cr-hBN, Au/Ti-hBN. For µm-sized Au-hBN the slip distance (determined from the tip speed and time between stick-slip peaks) was ∼2 nm versus 8-10 nm for Au/Ti (100/10 nm) on hBN.

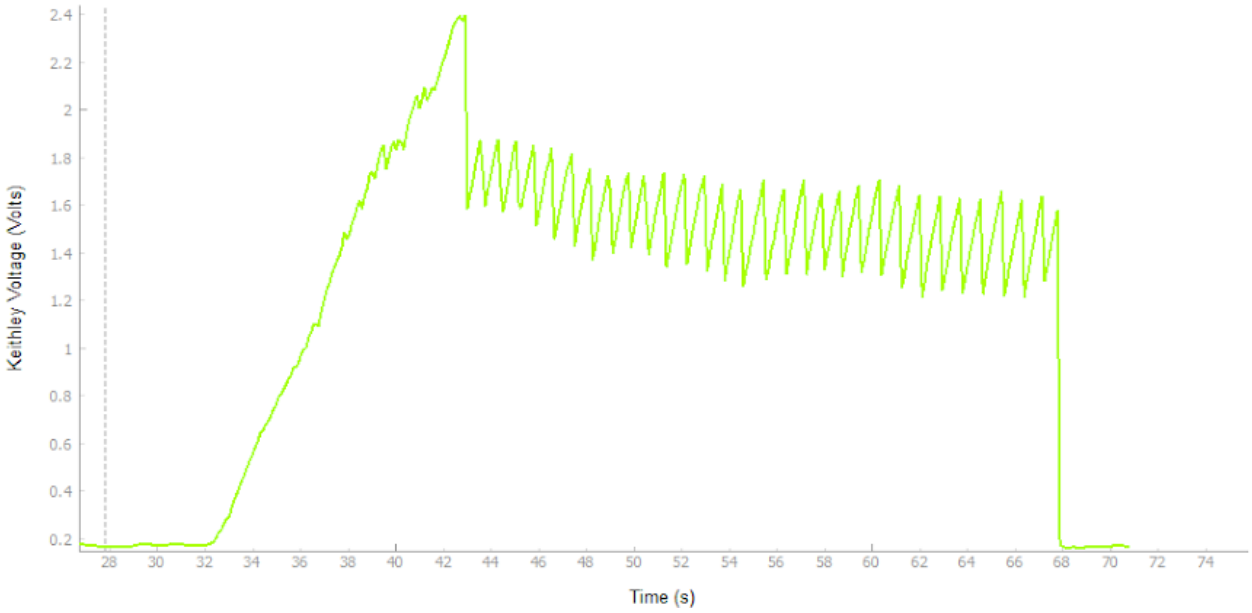

Figure 3.11: Stick slip motion

Friction signal of a Au/Ti (100/10 nm) rotor sliding on hBN with a tip speed of 10 nm/s, average distance for the slips is 8 nm.

3.4.2 Manipulating gold on hBN

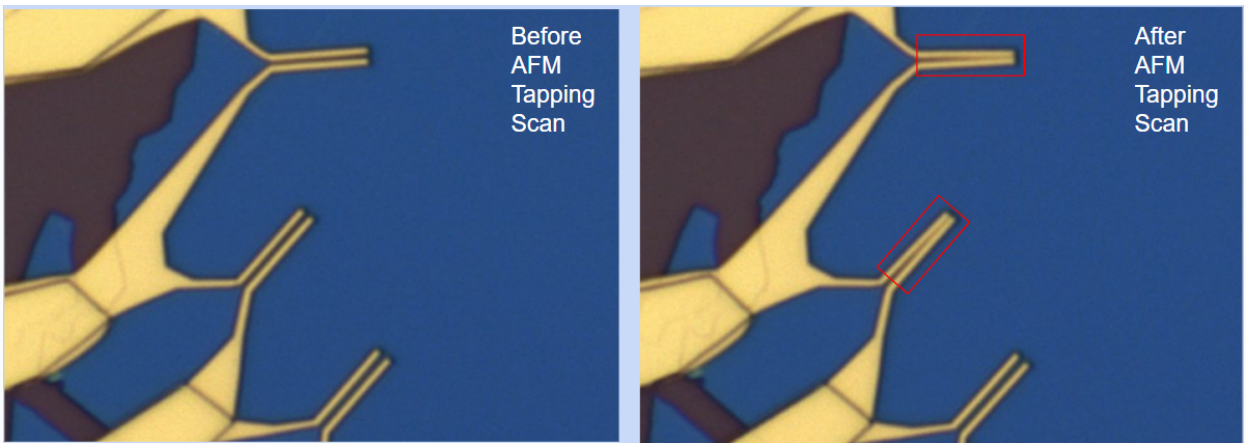

Figure 3.12: Au-only pushed by tapping mode AFM (AS18)
A 150 nm tall gold only electrodes on hBN before AFM tapping scan. **B** The same features accidentally pushed together as a result of imaging in tapping mode.

3.5 Room temperature probe and AFM manipulation

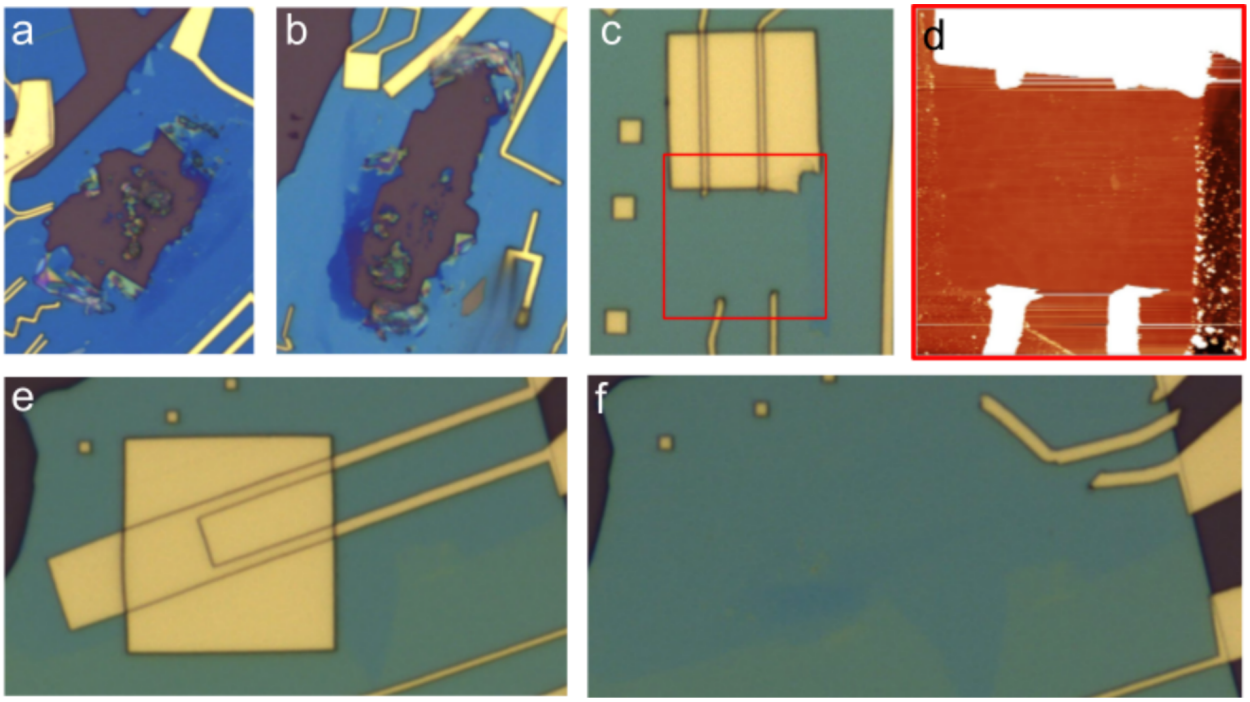

Figure 3.13: Flat Au-only pads on hBN for probe tip manipulation
Various samples with 100 nm thick Au pads. **A,B,C,E,F:** Attempted manipulation in Janis cryoprobe station at LN2 temperatures. **D:** AFM of **C** showing mostly undamaged hBN in the region the Au slid, with a gouge on the right edge. **A**: AS18, **B**: AS19, **C,D,E,F**: AS20

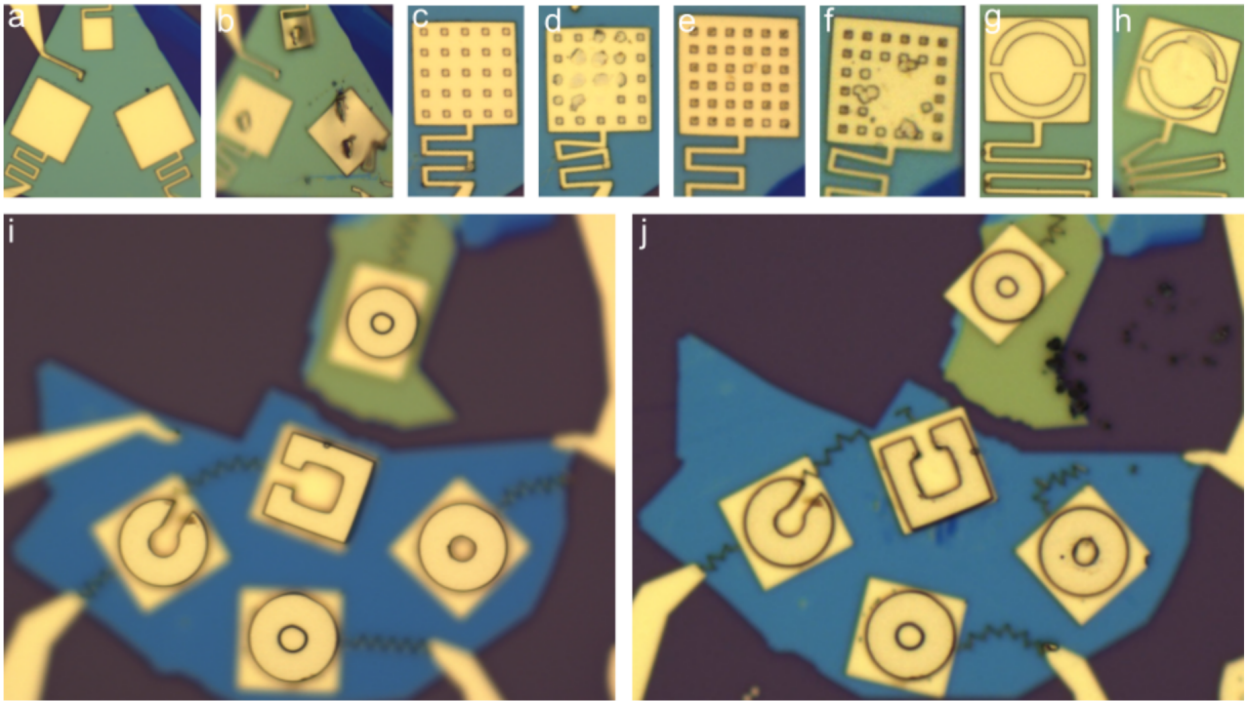

Figure 3.14: Before and after probe tip manipulation with anti-slip measures.

A,B,C,D,E,F,G,H: Before and after 100 nm thick Au anti-slip measures. These did not reliably keep the probe tip from slipping on the Au pad. **I,J:** Au pads with Cr/Cu/Cr/Au (10/1000/10/80 nm) donut shapes. These performed much better at keeping the tip from slipping. However, the tip could still gouge the hBN through the 100 nm base Au pad.

A,B: AS26, **C,D:** AS27, **E,F:** AS28, **G,H:** AS31, **I,J:** AS35

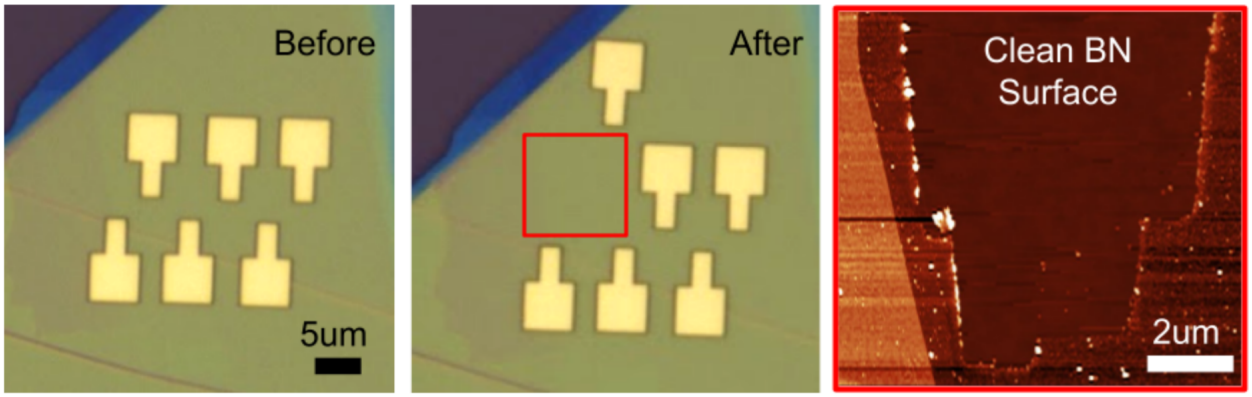

Figure 3.15: Before and after probe tip manipulation with anti-slip measures (IS-SiO2-01-T1) **Left & Middle:** Before and after images of gold features on hBN manipulated (100's of back/forth motions) via a ground down AFM tip pressing into the gold. **Right:** AFM afterward of the undamaged hBN surface. The poor XY control, large degree of slipping, and potential to still gouge hBN underneath lead us to attempt motion using AFM tips. While tips for imaging were quite sharp and could gouge hBN through 100 nm of Au, ground down tips, with pyramid apex of ∼3 µm wide, would distribute the force much more evenly. Additionally, they slipped much less, likely because the corner of the apex plateau was sharp and could dig into the Au. AFM tips are also very helpful for avoiding extremely large forces on the hBN because they are designed to be compliant in the out-of-plane direction, lessening the force and providing clear feedback for contact when the cantilever deflects (by eye, though a more advanced system could use a laser and photodiode to detect deflection as in a standard AFM system).

The poor XY control, large degree of slipping, and potential to still gouge hBN underneath lead us to attempt motion using AFM tips. While tips for imaging were quite sharp and could gouge hBN through 100 nm of Au, ground down tips, with pyramid apex of ∼3 µm wide, would distribute the force much more evenly. Additionally, they slipped much less, likely because the corner of the apex plateau was sharp and could dig into the Au. AFM tips are also very helpful for avoiding extremely large forces on the hBN because they are designed to be compliant in the out-of-plane direction, lessening the force and providing clear feedback for contact when the cantilever deflects (by eye, though a more advanced system could use a laser and photodiode to detect deflection as in a standard AFM system).

3.6 Montana cryostat cryogenic manipulation

Figure 3.16: Montana crude probe tip manipulation setup and damaged sample

Left & Right: Probe tip clamped to bent copper sheet. **Bottom:** AS35 which was manipulated at 4K via that probe tip. Likely issue is that the tip holder was too floppy and oscillated by ∼microns when the cryostat was running. This resulted in it acting like a jackhammer of sorts. This attempt was still useful though because some of these Au pads were pushed indirectly and slid on the hBN, providing evidence that Au could slid on hBN at liquid He temperatures without damage to the sliding interface.

3.6.1 Janis ST-500 cryogenic manipulation

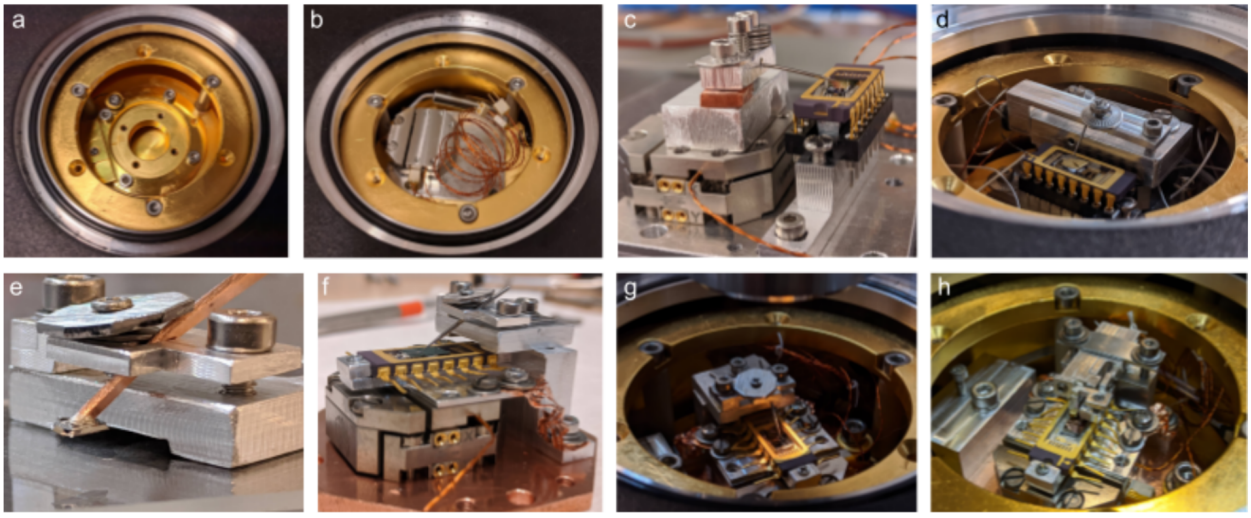

Figure 3.17: Progression of ST-500 cryogenic manipulation setup

A: Empty cryostat with ring-shaped heater holder. The ring shape is to heat the stage uniformly. **B:** Attocube and custom base plate inside ST-500. **C,D,E:** Prototypes with needle holder mounted to the Attocube and sample held stationary **F:** Prototype with sample mounted to the Attocube and needle holder stationary (at cryogenic temperatures and adjustable by hand at room temperature). This switch is enabled by bending the chip carrier pins outward and allows the sample and Attocube to be mounted more centrally in the cryostat. Since the samples and Attocube are similar sizes, it makes sense to have the sample on the Attocube. If instead the tip was on the Attocube, it would increase the XY footprint of the sample and tip. Though such a design should not necessarily be ruled out. **G:** Setup in F inside the cryostat **H:** AFM tip holder instead of a probe tip holder. This setup has a XYZ flexural arm actuated by set screws in order to perform coarse positioning at room temperature. This design, while very cool looking and compact, had too much cross talk between the different directions in order to be useful. It was easier to perform coarse positioning simply by hand. Additionally the 2 screw clamping mechanism here resulted in the probe tip holder shifting laterally as the screws were tightened down. The simpler single screw clamp of the previous designs was much more stable.

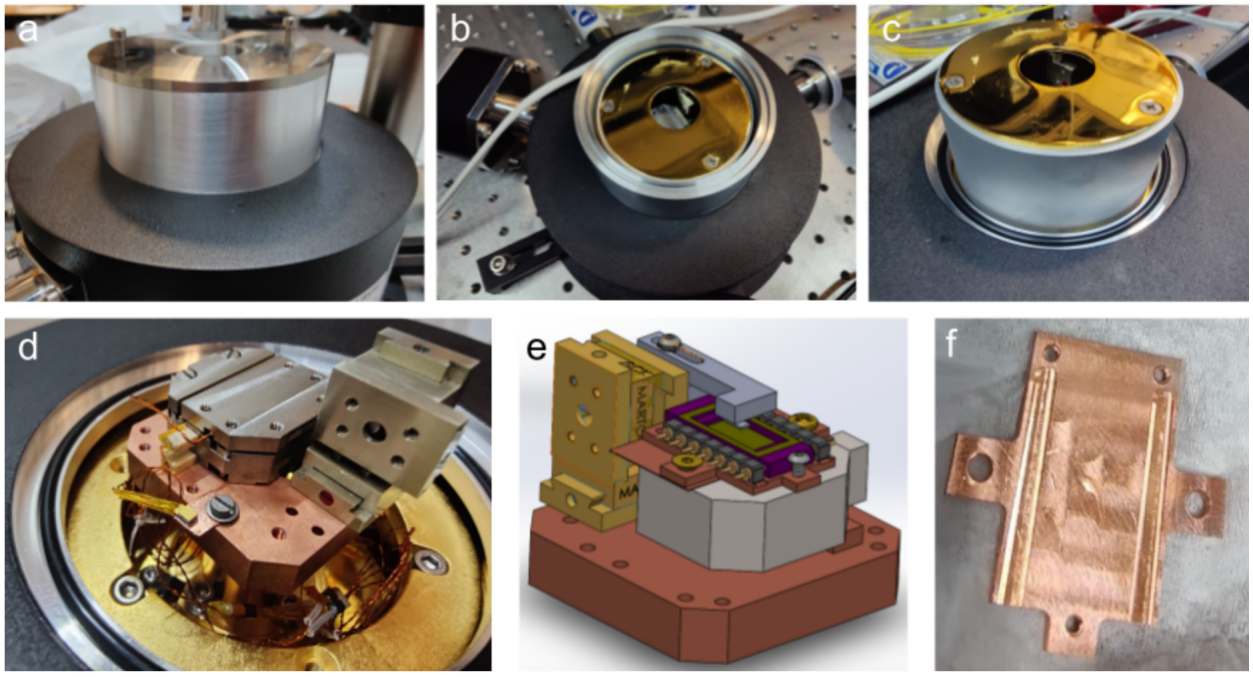

Figure 3.18: Current state of ST-500 cryogenic manipulation setup

A,B,C: Views of the custom vacuum shroud and radiation shield extension. **D:** Attocube and Elliot Martock semi-custom ultra small XYZ micropositioner mounted to an elevated plate, which is itself mounted to the Janis stock sample pedestal. This brings the working area higher and accessible from all directions compared to the prior recessed position. **E.** Solidworks assembly showing the sample, pogo pins for contact and AFM tip holder. The tip holder still needs to be finalized and machined. And the thermal links from the elevated baseplate to the sample holder must be made. **F.** 1 of 2 machined sample holders with tapped mounting hold and grooves for pogo pins.

3.7 Moire charge pumping devices

3.7.1 Theory and charge pumping mechanism

When aligned to hBN, graphene's band structure modifies due to the moire superlattice between the materials. The A and B sublattice sites of graphene become more inversion asym-

metric due to hBN inherent inversion asymmetry. This opens a band gap at the graphene's charge neutrality point. Additionally the moire pattern couples opposite ends of the Dirac cone via the moire wavevector, resulting in satellite Dirac points (SDPs) and gaps. These gaps occur at densities of 4 electrons per moire unit cell, as this corresponds to full filling of the minibands formed by the moire.

At these SDPs the electron wavefunctions can be described as Wannier functions localized by the moire pattern. This means that the translation of the moire will result in translation of the localized change as well.

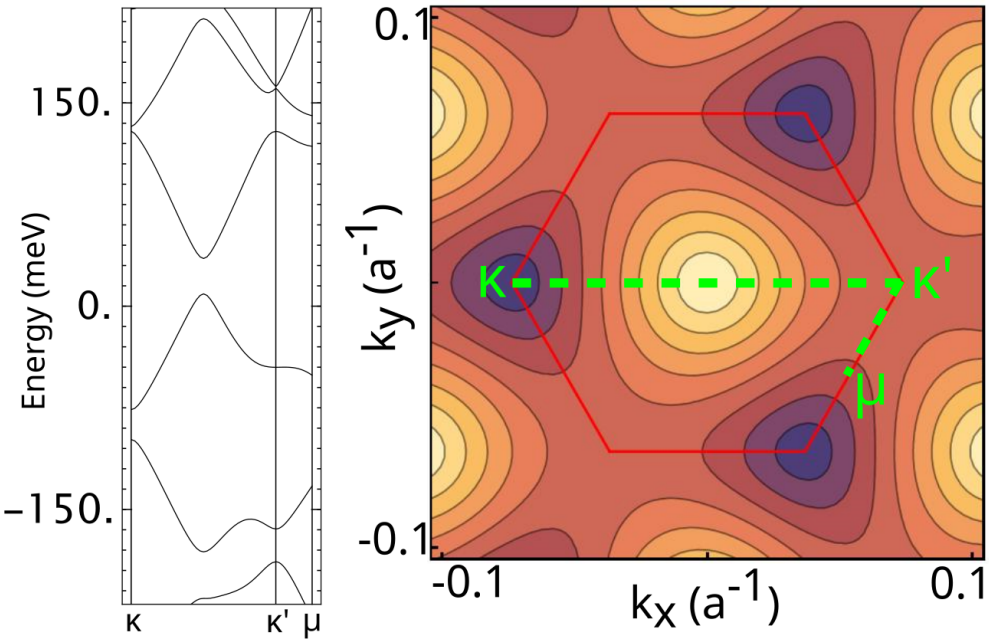

Figure 3.19: Aligned graphene-hBN band structure and density of states

Right image shows a contour plot of the hole side band with a dashed green line to indicate the path of the cut. Units are in inverse graphene lattice constants. Contour intervals are 10 meV

The most straightforward method to translate the charge is to move the whole crystal. However, it is also possible to move the moire by translating one of the layers, most feasibly, the graphene. When the graphene is translated by one lattice constant the moire pattern

also translates but instead by a distance of one *moire* lattice constant. This means that the moire lattice motion is amplified relative to the graphene motion by a ratio of 14/.246, or ∼57. This larger moire motion means that the moire lattice sweeps across the graphene as it moves.

If the system is doped to the hold SDP, the moire will drag the 4 electrons per unit cell as it moves, shuttling charge from one end of the graphene to the other. If the graphene is made to oscillate, such a measurement could be made as a lock-in measurement.

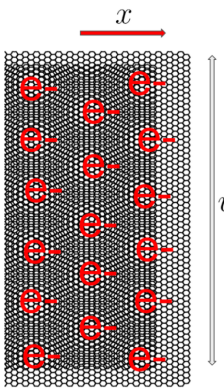

$$I = \rho w \frac{dx_{moire}}{dt} \qquad x_G = A\sin(2\pi f t) \qquad x_{moire} = \frac{a_{moire}}{a_G} A\sin(2\pi f t)$$

$$I = 2\pi f \rho w \frac{a_{moire}}{a_G} A\sin(2\pi f t)$$

$$w = 1\ \mu\text{m}, \quad A = 10\ \mu\text{m}, \quad f = 100\ \text{kHz}, \quad a_G = .246\ \text{nm}, \quad a_{moire} = 14.0\ \text{nm}$$

$$I \approx 0.5\ \text{nA}$$

Figure 3.20: Illustration of localized charge and expected current for oscillatory motion

3.7.2 Open face devices

Initially, we attempted a device style similar to the Dean group g-hBN twisting study, with an open face graphene strip and a sliding aligned hBN piece on top. The primary issue here was that the hBN would tear the graphene as it was slid onto the graphene. It is possible that this worked for the Dean group due to lighter etching parameters or possibly tip cleaning before transferring the hBN rotor. In addition to tearing the graphene during alignment, this suggested we would be unable to oscillate the rotor safely. We devised the alternative, "hockey puck" structure, which protects the graphene and should handle motion better.

3.7.3 Rotors and Cr,Ti friction

In the process of attempting open face devices, we found that the friction of Au/Ti and Au/Cr to hBN was often not sufficient to slide the hBN rotors on an etched hBN substrate. This was especially an issue when the rotors had been annealed, as the Cr and Ti will migrate into the Au and away from the interface, significantly decreasing their contribution as a sticking layer. This was even evident when picking up rotors with a stamp, as the Au/Cr or Au/Ti cap would slide off of many rotors during the natural translation which occurs during the pickup/transfer process.

3.7.4 Outlook

There were several challenges and unknowns which remained when we paused this project. Whether the friction of *aligned* graphene-BN at cryogenic temperatures would allow us to oscillate a hockey puck device. Whether we could make contacts which would stay connected (our test sliding device became disconnected from slow sliding at room temperature). Sliding at high enough frequency is also an issue. The resonance frequency of the Attocube, tip holder, and Martock XYZ state are in the 500-1500 Hz range, which limits the hockey puck oscillation frequency to below that.

Another issue we had was that the graphene would slip out from under the hBN until it aligned with the top hBN. The need to have the moire only between the graphene and the bottom hBN means that the friction of that interface would be higher than that between the graphene and the top hBN. In order for the graphene to slide on the bottom hBN there would need to be an additional force to overcome the graphene bottom hBN friction. At the time we attempted having extra graphene extending from under the top hBN, a "g-out" device, but as we discovered here and later for our heterostrain project, the friction between aligned g-hBN is higher than that of g-Cr or even g-Ni.

All of these issues besides the resonance should be somewhat resolved by our method for gripping monolayer graphene explained in the heterostrain paper. Here the strong adhesion of the O_2-plasma contacts is enough to overcome aligned g-BN friction at room temperature. The pre-etched holes in the hBN give electrical contact which is separate from the handles (likely necessary for good/better contact).

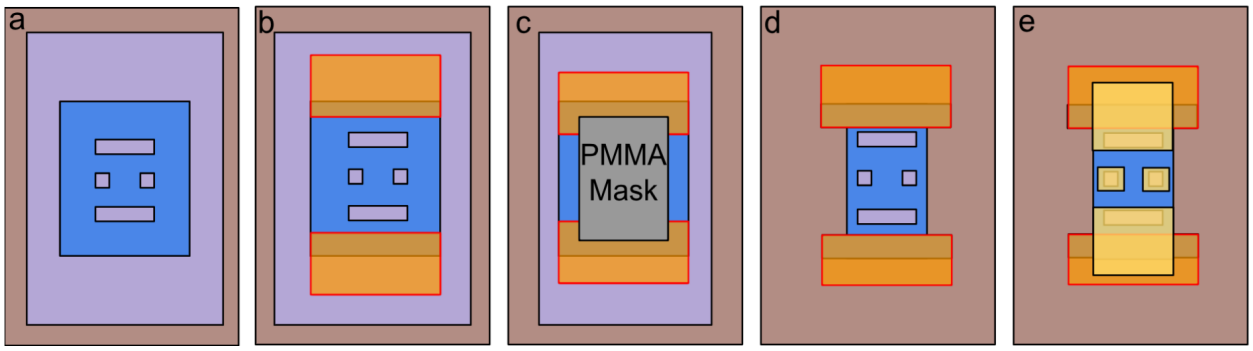

Figure 3.21: Possible fabrication for graphene hockey puck devices

A: graphene (purple) on SiO2, with pre-etched hBN (blue), transfered on top **B:** high friction O_2-plasma-treated Au/Cr handle contacts **C:** PMMA etch mask **D:** $SF_6 + O_2$ reactive ion etch to remove hBN and graphene **E:** Au/Cr or Au contacts added

With a frequency of 100-1000 Hz, the generated current would be ∼0.5-5 pA.

3.8 Curved metal with super low friction

The most extreme case of low friction we observed was for Au/Cr metal which curved outward on the substrate, resulting in very little contact between the metal and substrate and a factor of ∼7-13 reduction in the interface friction. This curvature was likely due to internal stress from the deposition, and stress like this could likely be created intentionally in order to make extremely low interface friction devices.

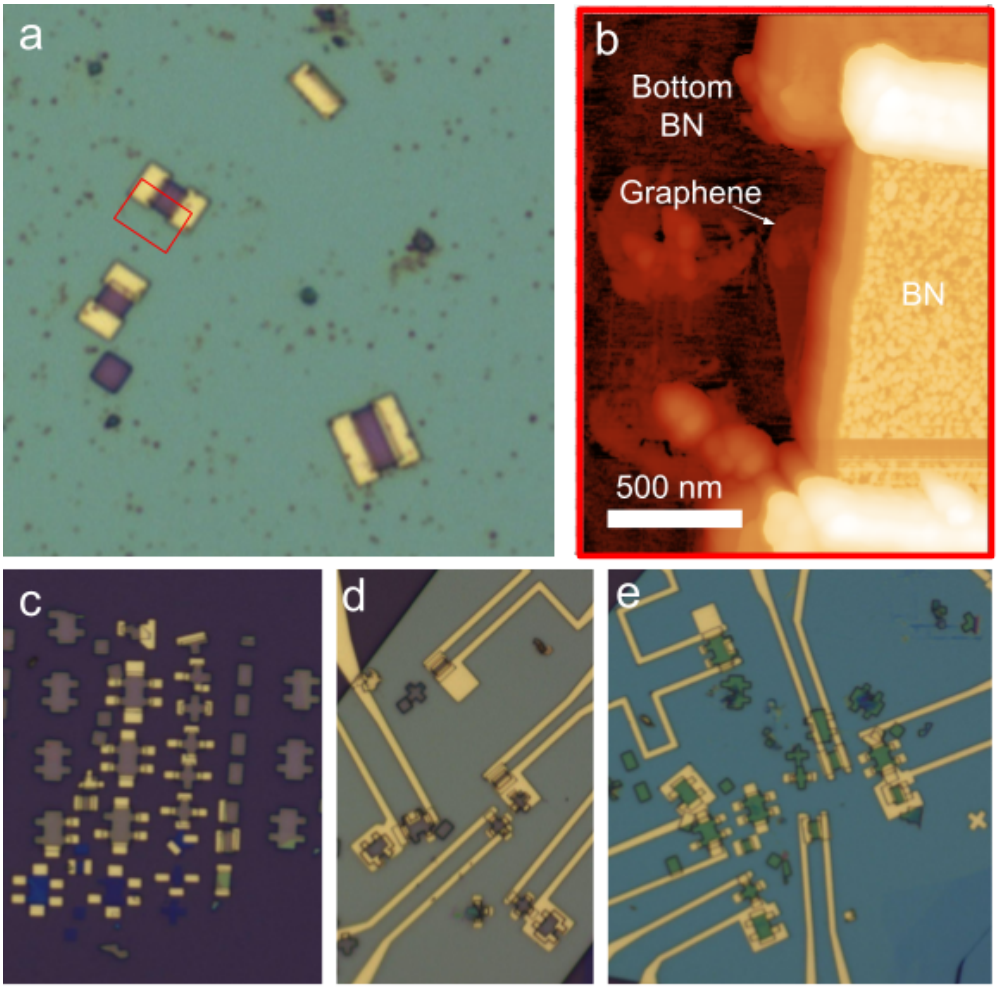

Figure 3.22: Hockey puck devices

A: Hockey puck device transfer to hBN **B:** Close up AFM height image showing graphene slipped out from under top hBN **C:** Graphene-out hockey puck devices before transfer to hBN substrate **D&E:** After transfer and electrical contact. These suffered from graphene slippage just like the non graphene-out devices.
A,B AA10, **C,D** IS27, **E:** IS26

Similarly, reductions in friction were seen for Au/Ti rotor masks which slipped on hBN yet remained suspended above the substrate. This was due to some combination of their rigidity and some built in stress, which caused them to bend upwards. As the Au/Ti slid off the hBN, the friction decreased. Eventually the adhesion force between the Au/Ti and hBN was overcome and the Au/Ti collapsed onto the underlying substrate.

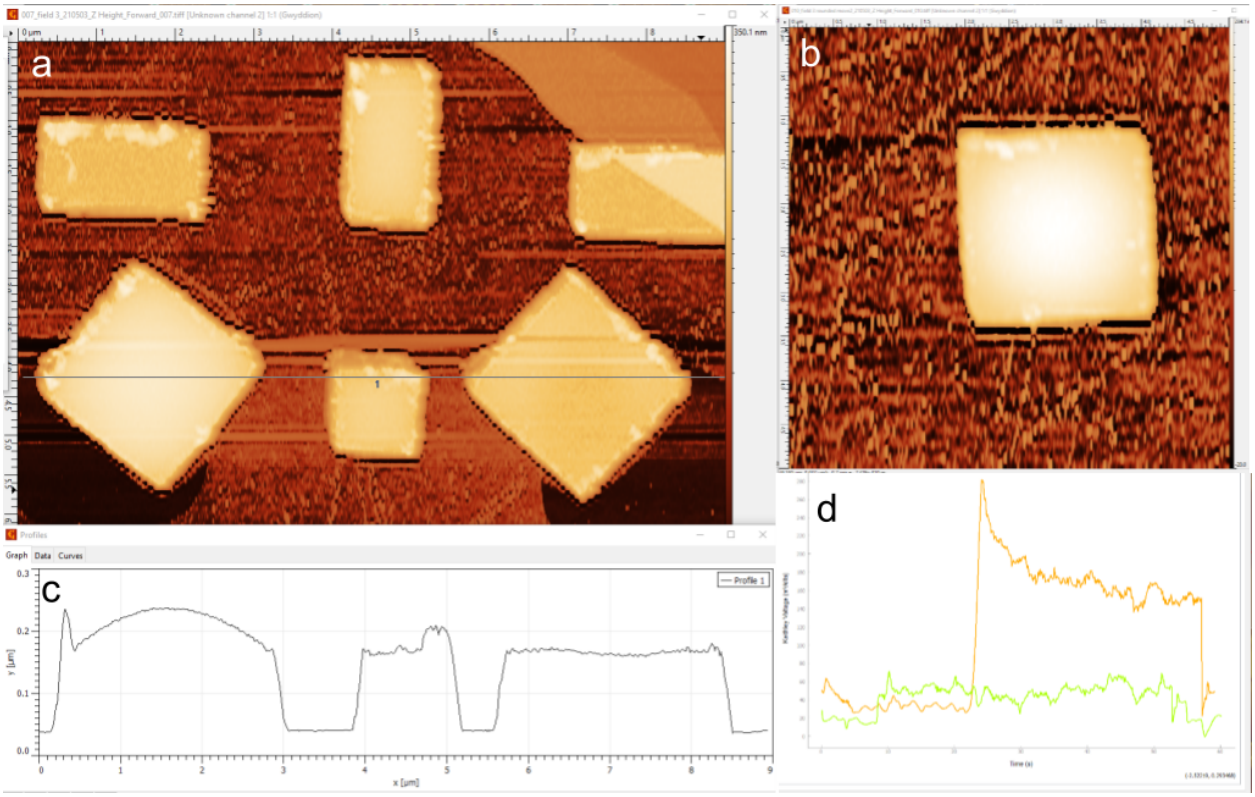

Figure 3.23: Arched Au/Cr metal on graphene/SiO_2 (AG6-TL)

A: AFM height data showing some Au/Cr squares which are rounded due to internal strain and others which remained flat. It is also apparent that some of the squares tore the graphene on which they were deposited **B:** height profile from image A **C:** AFM height image of a rounded square **D:** AFM lateral friction data showing a flat square sliding on graphene (orange), compared with a rounded square sliding on graphene (green) exhibiting significantly lower friction

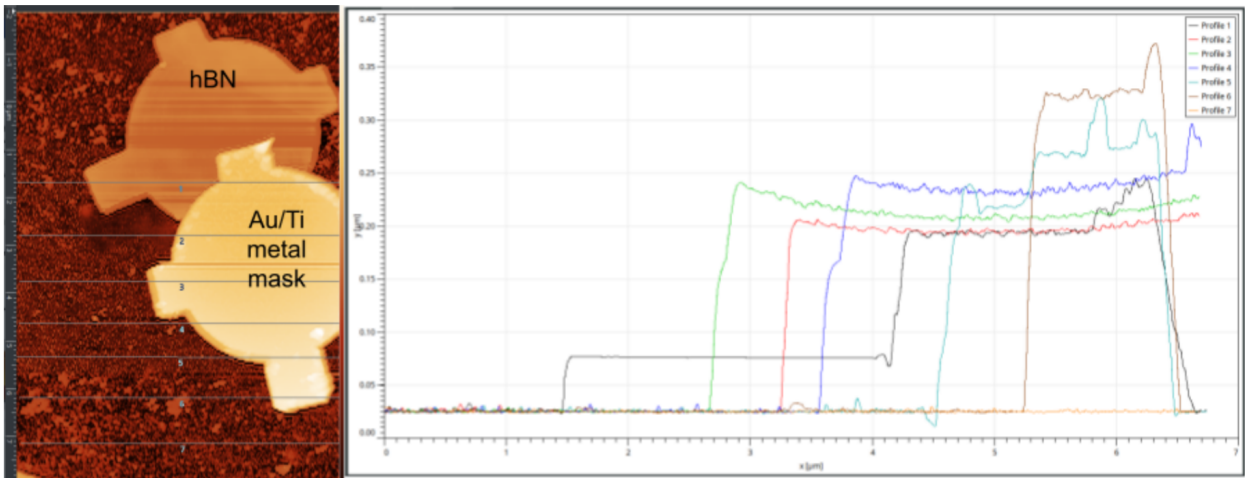

Figure 3.24: Au/Ti mask on hBN suspended in air over the edge (AS43)

Left: AFM height image of Au/Ti mask partially slid off of hBN. From the brightness it is clear that the metal in the lower section of the image is curve upwards and not in contact with the underlying substrate **Right:** Line traces from the height data image showing the bottom-most portion of the metal is curved ∼120 nm above the metal which is in contact with the hBN.

3.9 Electrostatic thermal actuators

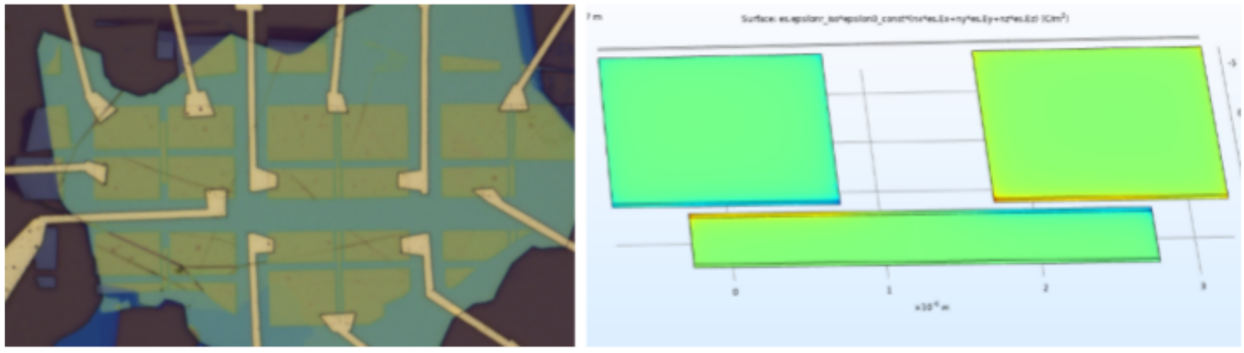

Figure 3.25: Graphite electrostatic actuator device and a related COMSOL force simulation

Left: AS22 (AKA AG10-L G2), etched and contacted graphite flakes which did not move when a voltage was applied **Right:** COMSOL simulation displaying surface charge density for a coplanar capacitor geometry

Our earliest attempts at van der Waals motion came in the form of electrostatic and thermal actuation devices. The electrostatic devices relied on the metal or vdW flakes forming capacitors which, when charged up, would feel an attractive force to each other. Our attempts at graphite devices of this style did not succeed, but gold metal ones did, and we heard from the Cory Dean group that they were able to make such a device with a center graphene flake and outer gold electrodes actuate and bend the graphene.

Due to the complication of the van der Waals transfer process and the favorable forces for coplanar electrostatic devices, we transitioned to making devices using evaporated gold. The electrostatic actuators were initially designed as simple 2-probe devices where the 2 electrodes would attract each other. However, this design has a flaw in that when the actuation was successful, the electrodes would touch and short the circuit, suddenly passing such large currents that the wires would explode (see figure below). We developed an alternative geometry which used 5 probes: 1 center wire which would move, 2 outer wires to which a large voltage would be applied, and 2 additional sensor wires which would make contact with the center wire when it was actuated, heralding the motion with a small signal current.

We had 2 styles of thermal actuators. The first style was a U-shaped thermal actuator which should straightforwardly expand according to its thermal expansion coefficient. These devices were able to work, though they could also fail due to too high of a current flow. The other style was Chevron-shaped. Its geometry is inspired from MEMS thermal actuators and should result in some amplification. We were not able to determine if this style was able to actuate.

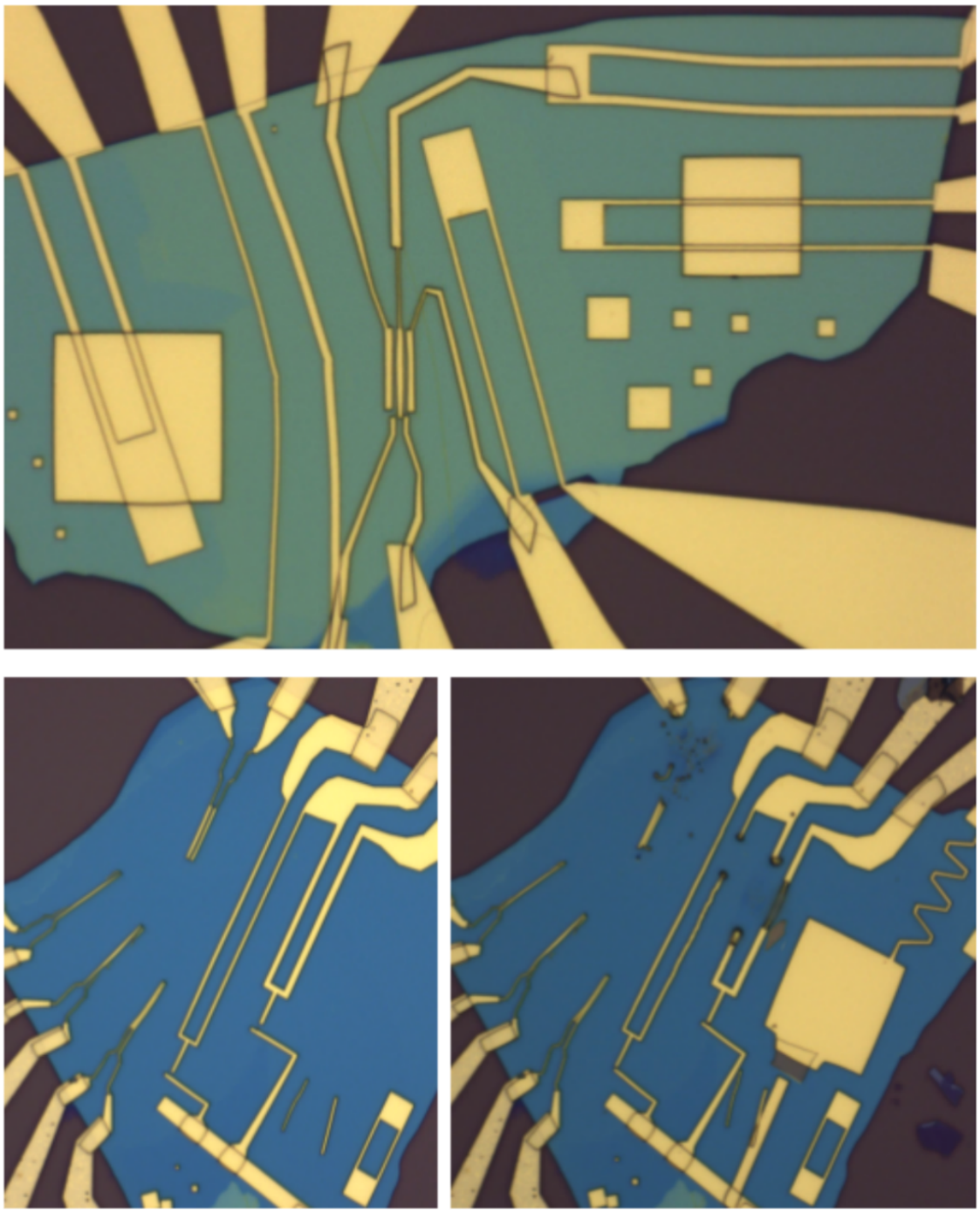

Figure 3.26: Au electrostatic and thermal actuators on hBN

Top: Electrostatic and thermal actuator devices. Some of whose contacts were later used to make alternative devices and sliding test shapes (AS20). **Left:** Actuator devices before actuation (AS19). **Right:** Actuator devices after actuation and subsequent damage due to high currents.

3.10 Motion due to fluids

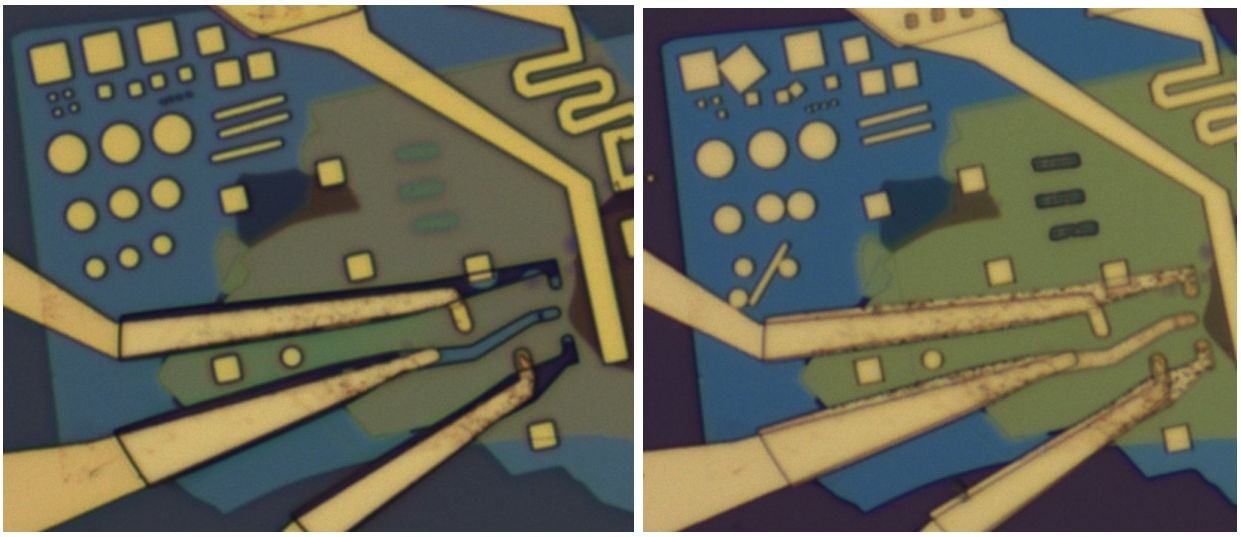

Figure 3.27: Au sliding on hBN due to liftoff in acetone (AS59)
Left: sample with Au on hBN features in the top left corner. Sample is covered in PMMA. **Right:** after liftoff the Au features have move significantly, especially small or high aspect ratio ones. The narrow strip which moved the most was designed to be 500nm wide.

We've seen motion as a result of violent squirting during liftoff, one example is shown in Figure 3.27. In addition to these accidental motions, I tried to intentionally move 1 µm thick Au/Cr/Cu/Cr/Au features using ∼100 psi N_2 gas. 1 MPa (145psi) applied to 1x1 µm surface will exert a force of 1 µN, which exceeds the static friction of a 1 m^2 Au-hBN interface of .4 µN. Assuming all of the force is applied to the surface, 58 psi should be sufficient to move a 1x1x1 µm cube of Au on hBN. In practice, it's likely that a drag/viscous fluid model is a better approach.

Chapter 4

Manipulating moires by controlling heterostrain in van der Waals devices

Y'all been standing on rocks this whole time? - Hannibal Buress

This content is in preparation for submission to ACS Nano Letters.

4.1 Paper main text

Abstract: Van der Waals (vdW) moires offer tunable superlattices that can strongly manipulate electronic properties. We demonstrate the in-situ manipulation of moire superlattices via heterostrain control in a vdW device. By straining a graphene layer relative to its hexagonal boron nitride substrate, we modify the shape and size of the moire. Our sliding-based technique achieves uniaxial heterostrain values exceeding 1%, resulting in distorted moires that are larger than those achievable without strain. The stretched moire is evident in transport measurements, resulting in shifted superlattice resistance peaks and Landau fans consistent with an enlarged superlattice unit cell. Electronic structure calculations reveal

how heterostrain shrinks and distorts the moire Brillouin zone, resulting in a reduced electronic bandwidth as well as the appearance of highly anisotropic and quasi-1-dimensional Fermi surfaces. Our heterostrain control approach opens a wide parameter space of moire lattices to explore beyond what is possible by twist angle control alone.

4.1.1 Introduction

Moire materials offer highly-tunable superlattices with lengthscales that are unattainable in natural crystals. The extreme sensitivity of the electronic behaviors and correlated states to the moire structure motivates the precise control of moire patterns, especially in-situ manipulation techniques [8, 31–33]. These efforts have primarily focused on controlling the relative twist angle, which determines the size of the moire pattern, but cannot alter its shape or symmetry.

Strain control offers an alternative route to manipulating moire patterns beyond what is possible via twist angle, where both the size and symmetry of the moire can be altered. To strongly distort the moire, it is necessary to strain adjacent layers by different amounts, which is referred to as heterostrain. The possibility of achieving large heterostrain on the atomic scale is a unique feature of van der Waals (vdW) materials due to exceptionally low interlayer shear strengths [34]. When two lattices form a moire, the effects of heterostrain are amplified by a moire factor $\sim 1/(\delta - \epsilon)$, where δ is the mismatch between the lattices and ϵ is the strain in one layer. This factor diverges as ϵ approaches δ, and has a directionality set by the strain direction. As a result, heterostrain can strongly distort the moire, changing its size and symmetries in a way not possible when straining both layers simultaneously (Figure 4.1a,b,c)[35, 36]. Correspondingly, heterostrain can also strongly manipulate moire systems' electronic structure, especially in flatband systems such as twisted bilayer graphene[36–38].

To date, the experimental study of heterostrain has been limited by the challenge of con-

trollably producing uniform and large heterostrain. Local probes such as scanning tunneling microscopy or optical measurements have been successful in measuring the effects of heterostrain on spectroscopic features[39–45], but transport measurements have been more limited due to the need for uniform heterostrain over larger areas. Current transport studies have relied on moire heterostrain introduced accidentally in the nanofabrication process[37, 46]. Such strain profiles are generally small, and of uncontrolled direction and homogeneity. Progress has been made in controlling strain in vdW heterostructure devices by stretching or bending the underlying substrate[47–49], or by using deposited stressors[50–52]. For all approaches, an outstanding challenge is to achieve large and controlled heterostrain in a high-quality moire device.

4.1.2 Heterostrain technique

Here, we demonstrate the control of uniaxial heterostrain in graphene-hexagonal boron nitride (g-hBN) devices and study its effects on moire structure and transport properties. To achieve this, we have fabricated open-faced graphene devices on an hBN substrate where the electrodes are used to both measure transport and selectively strain the graphene (Figure 4.1d&e). The graphene is aligned to the hBN using a gold-based transfer method that deterministically produces large moire superlattices (see deterministic alignment of g-hBN samples in the methods section).

Following our prior work on mechanically-reconfigurable vdW devices[53], we implement a moveable handle electrode that grips the graphene to slide and stretch it across the hBN. To selectively adhere the metal handle to the graphene only, we apply a light O_2-plasma etch before depositing the Cr/Au handles. The graphene-handle bond is strong enough to strain graphene beyond its tensile strength and tear it (Figure 4.8a&b). We found the plasma pretreatment to be critical, as thermally-evaporated metals such as Au, Cr, and Ni exhibit low

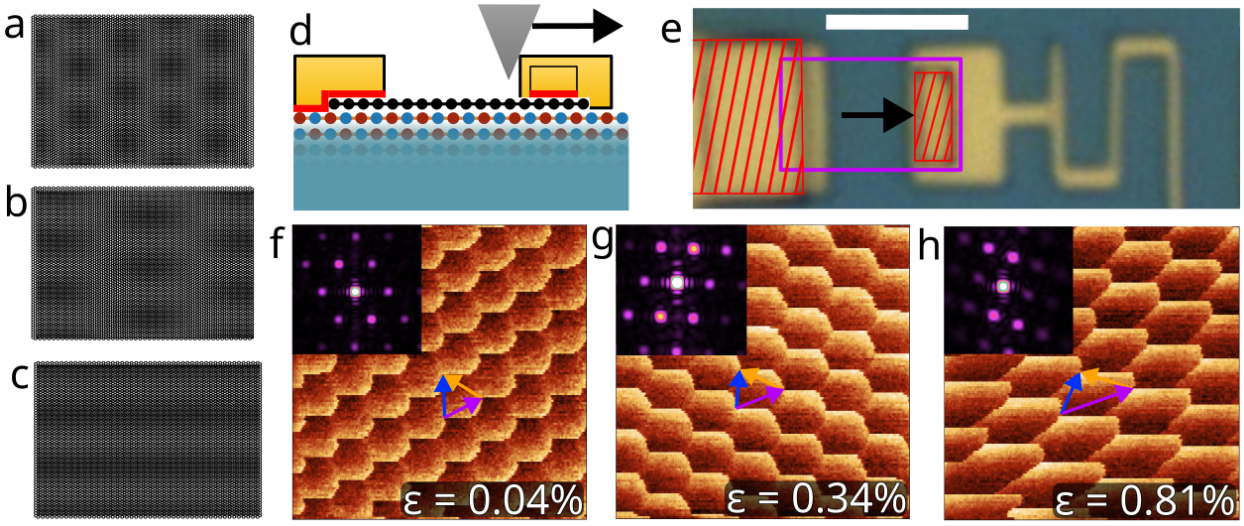

Figure 4.1: Controlling heterostrain to manipulate vdW moires formed between graphene and hBN
a-c: Hexagonal lattices with a $\delta = 5\%$ lattice mismatch. a: unstrained, b: 2.5% uniaxial heterostrain, c: 5% uniaxial heterostrain. **d:** Side view schematic of a stretchable open-face graphene-boron nitride device with an AFM tip pushing on one electrode. Red lines indicate areas that are O_2-plasma treated before deposition **e:** Optical image of device B. Scale bar is 4 µm **f-h:** 100x100 nm CAFM images of g-hBN moires in device A. Inset shows FFT of the image. Fitting the wavevectors results in the indicated strain values ϵ (±3e-4 uncertainty) with strain angles relative to the +x-axis of +80±20°, +1±5°, +17±4°, and twist angles -0.12°, 0.02°, 0.02° for f,g,h, respectively. All parameters and uncertainties are listed in SI Table 4.1

sliding friction on graphene and cannot overcome the friction of graphene aligned to hBN.

The devices are designed with a fixed source electrode and a moveable drain electrode that can be displaced laterally by pushing with an atomic force microscope (AFM) tip (Figure 4.1d&e), inducing heterostrain in the gripped graphene layer. The moveable electrode has sufficient sliding friction to retain the graphene strain when the AFM tip is retracted. The end result is an open-face graphene device that can be progressively strained independent of the hBN substrate. The graphene strain can be directly observed both in the physical displacement of the graphene edges (measured in AFM), as well as in Raman shifts of the graphene G peak, both showing at least 0.6% strain can be fixed in the graphene layer (Figure 4.9a-d).

To image the effects of heterostrain on the g-hBN moire, we perform conductive AFM (CAFM) on the open graphene channels (Figure 4.1f-h). An unstrained graphene is shown in Figure 4.1f, where the moire pattern appears clearly in CAFM with a $\sim$14 nm wavelength, the maximum possible for unstrained g-hBN. By stretching the graphene via the gold handle, we observe a large elongation of the moire along the strain direction, in line with the channel (Figure 4.1g&h). For the case in Figure 4.1h, the moire lattice vector most aligned to the strain direction is stretched by 84% to 25.7 nm.

To analyze the stretched moire structure, we extract the moire lattice vectors from the fast fourier transform (FFT) of the CAFM images. We find that a uniaxial strain model can fit most device regions to within 1% of the extracted wavevectors. By assuming pure uniaxial graphene heterostrain, we can extract local values for the uniaxial strain (ϵ), strain direction (ϕ), relative graphene-hBN twist angle (θ), as well as the global orientation of the layers with respect to the AFM image (See SI Uniaxial heterostrain model and fitting section).

4.1.3 Characterization of moire with CAFM

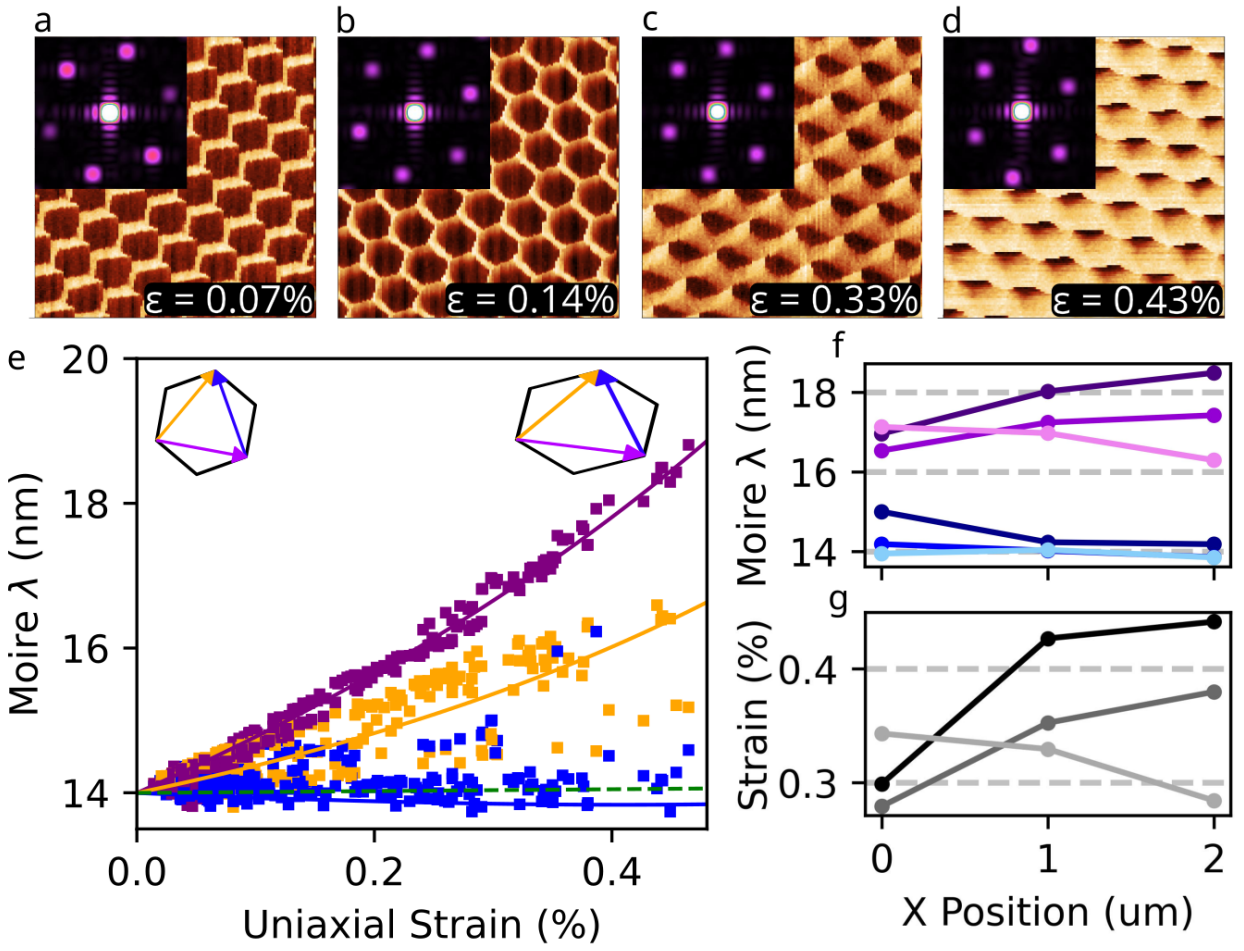

Figure 4.2: Progressive uniaxial strain and spatial uniformity in device B

All reported strain values have an average uncertainty of ±0.02% due to a 1% uncertainty in measuring the moire wavevector. All parameters and uncertainties are listed in SI Table 4.1. **a-d:** Sequence of 100x100 nm CAFM images of graphene-hBN moires ordered from lower to higher strain (0.07% to 0.43%). Images are taken within ∼200 nm of the same location. Insets: FFT of the real space images. White hexagon overlay is the same for each panel as a reference to demonstrate the evolution of the lattice wavevectors with strain. **e:** Plot of measured moire wavelengths versus uniaxial graphene strain for ten strained states. Lines are theoretical moire wavelengths for a twist angle of 0.022° and strain angle of 18.279° with respect to the graphene lattice vector, that correspond to the average values for the dataset. Insets illustrate the moire unit cell orientation and stretch. **f:** Moire wavelength versus position for the most strained state. Blue/purple shaded points correspond to the blue/purple vectors in **e**, respectively. Different hues correspond to different rows along the devices separated by vertical distances of 1 µm. **g:** Graphene strain versus position for a single strained state. Each line is a row along the device.

To track the evolution of the moire patterns under strain, we incrementally stretch our samples and perform CAFM imaging in a grid of locations to characterize the homogeneity. Figures 4.2a-d show a sample of these for device B, as it is progressively stretched horizontally. We measure this sample in ten strained states and plot the measured moire wavelengths versus the strain values extracted from our uniaxial strain model fits (Figure 4.2e). As the graphene is stretched, we observe that the moire lattice vectors are elongated depending on their orientation to the strain axis. The (purple) moire vector, nearly aligned with the strain axis, is stretched up to 34% relative to 14 nm, corresponding to a 0.46% uniaxial strain of the graphene aligned 5±4° with respect to the AFM x-axis and the graphene channel. The (blue) moire vector that is nearly perpendicular to the strain axis shows little change. The theoretical moire wavelength for a 0° sample under uniaxial homostrain is plotted in green and shows weak dependence on strain. It is clear then that by heterostraining our samples we are able to achieve moire wavelengths that would be impossible using homostrain.

We compare the moire wavelength measurements to the expected values given by the average twist angle ($\theta = 0.022°$) and uniaxial strain angle ($\phi = 5°$ with respect to the horizontal) extracted for all the points (solid lines in Figure 4.2e). A majority of the datapoints are clustered around the model lines, indicating the uniformity in the twist and strain angles in the sample. See SI figure 4.12 for an example of a stretched device with a non-uniform twist angle.

The stretched moires exhibit a consistent spatial variation across the channel, with the largest moire wavelengths and strains near the stretching electrode. This effect is clearly seen in the final strained state in Figure 4.2 f&g. We attribute this strain gradient to the friction of the aligned g-hBN domains, as well as local pinning from sample edges and disorder, which prevents an ideal elastic response of the stretched graphene. Nonetheless, in the final state, the device is strained across its entire 2.1 µm length with a max wavelength that varies from 16.3 to 18.8 nm.

4.1.4 Effects on electronic properties

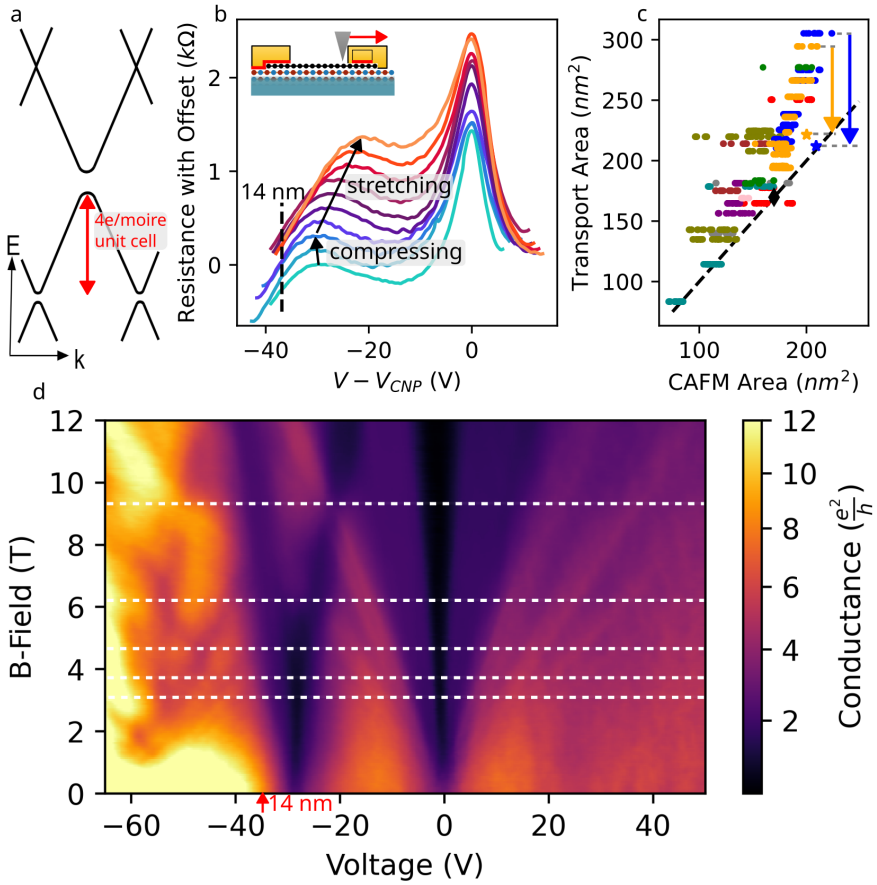

Figure 4.3: Effects of uniaxial heterostrain on the transport properties of graphene-hBN devices

a: Cartoon band structure of aligned g-hBN at zero strain. Each moire subband corresponds to 4 electrons per moire unit cell area. **b:** Room temperature gate sweeps of device B showing the superlattice peak shifting due to AFM manipulation. Sequential traces are offset for clarity. The measurements are made in situ to the AFM immediately after manipulating. The first two manipulations are compressive and the last seven are stretching motions. The dashed black line indicates the expected location of the superlattice peak for the largest unstrained moire, corresponding to a 14 nm wavelength. Inset: device manipulation schematic. **c:** Moire unit cell area measured from CAFM images versus the area extracted from the superlattice resistance peak position via transport. Marker colors differentiate 10 devices. Circle markers correspond to transport data taken at ambient conditions. The two star markers correspond to transport data taken at 1.6K (plotted at the average CAFM area). Devices B/C are colors blue/orange, respectively. The black dashed line denotes equal CAFM and transport areas. **d:** Magnetoconductance data of device C taken at 1.6K. Horizontal white lines overlaid correspond to a magnetic flux of 1/2,1/3,1/4,1/5,1/6 flux quanta per moire unit cell area ($221 \pm 5 \text{nm}^2$). A contact resistance value of 4.43 kΩ is subtracted to align the $\nu = 2$ plateau to 2 e^2/h.

The large heterostrain with micron-scale uniformity achieved with our approach offers a unique opportunity to study the electronic properties of stretched moires in transport. When graphene is aligned to hBN, superlattice-induced band gaps emerge at the edge of the reduced moire Brillouin zone (Figure 4.3a). In transport measurements, this results in new superlattice resistance peaks at densities n = ± 4/(moire unit cell area), where the peak at hole doping is more prominent (Figure 4.3b). As the aligned graphene is stretched, we observe the satellite resistance peak to progressively shift closer to the primary Dirac peak at charge neutrality. Compressing the channel shifts the peak in the opposite direction. This effect is consistent with heterostrain causing a substantial modification of the moire unit cell area. At the maximum strained state, the satellite peak has moved 29% closer to the main Dirac peak, suggesting a corresponding increase in the moire unit cell area.

To further analyze the behavior of the satellite resistance peak, we compare moire areas extracted from the resistance peak position to moire areas measured by CAFM.We plot these in Figure 4.3c for multiple devices in different strained states. Due to the applied heterostrain, many of the data points exceed the maximum area for unstrained, aligned g-hBN of $\sqrt{3}/2(14\text{nm})^2 \sim 170$ nm^2 (black diamond). The horizontal spread in CAFM areas is due to strain and twist angle inhomogeneity within each device. For small moires, there is agreement between the areas extracted from transport and CAFM. However, for stretched moires beyond $\sim$14 nm, the moire area extracted from transport consistently exceeds the area measured in CAFM. We ascribe this effect to the reduced electronic bandwidths of the stretched g-hBN devices. Similar effects have been observed in room temperature measurements of twisted bilayer graphene[46, 54]. Indeed, cooling down devices B and C to 1.6 K removes the discrepancy between the transport and CAFM areas (see SI satellite dirac peak temperature dependence section).

At cryogenic temperatures, applying a perpendicular magnetic field to devices with nearly-uniform heterostrain results in Landau fans emerging from the charge neutrality point and

the hole-side superlattice peak (Figure 4.3d and Figure 4.15). Figure 4.3d shows magneto-transport data for device C, which has an average uniaxial strain of 0.30±0.04%, twist angle of 0.03±0.04°, and strain angle of 9±4° with respect to the graphene lattice vector, where the uncertainties are the standard deviation from the CAFM dataset. Fan features emerge from a sharp superlattice peak corresponding to a moire area of 221±5 nm^2, which is close to the average areas measured by CAFM at room temperature (200±10 nm^2). Due to the stretched moire unit cell size, the primary Landau fan is disrupted at lower magnetic fields than is typical for g-hBN devices[55, 56]. These disruptions arise due to the collisions of the primary and superlattice Landau fans, with intersections occurring at B field values of 1 flux quanta per integer number of moire unit cells, $B = \phi_0/(q*A_m)$, where B is the magnetic field, ϕ_0 is the magnetic flux quanta, Am is the moire unit cell area, and q is an integer (horizontal lines in Figure 4.3d). We conclude that the heterostrain is sufficiently uniform to produce coherent superlattice modulation of the transport features consistent with a stretched moire unit cell.

Another characteristic of aligned g-hBN devices is the presence of an insulating state at charge neutrality due to the breaking of graphene inversion symmetry by the aligned hBN[56, 57]. In the heterostrained devices, we only observe a weak insulating-like dependence at the charge neutrality point or at the superlattice point for our heterostrained devices. We ascribe this to strain and charge inhomogeneity in the device, where the latter is known to play an important role in obscuring insulating states in graphene devices due to edge doping effects[58, 59].

4.1.5 Theoretical calculations

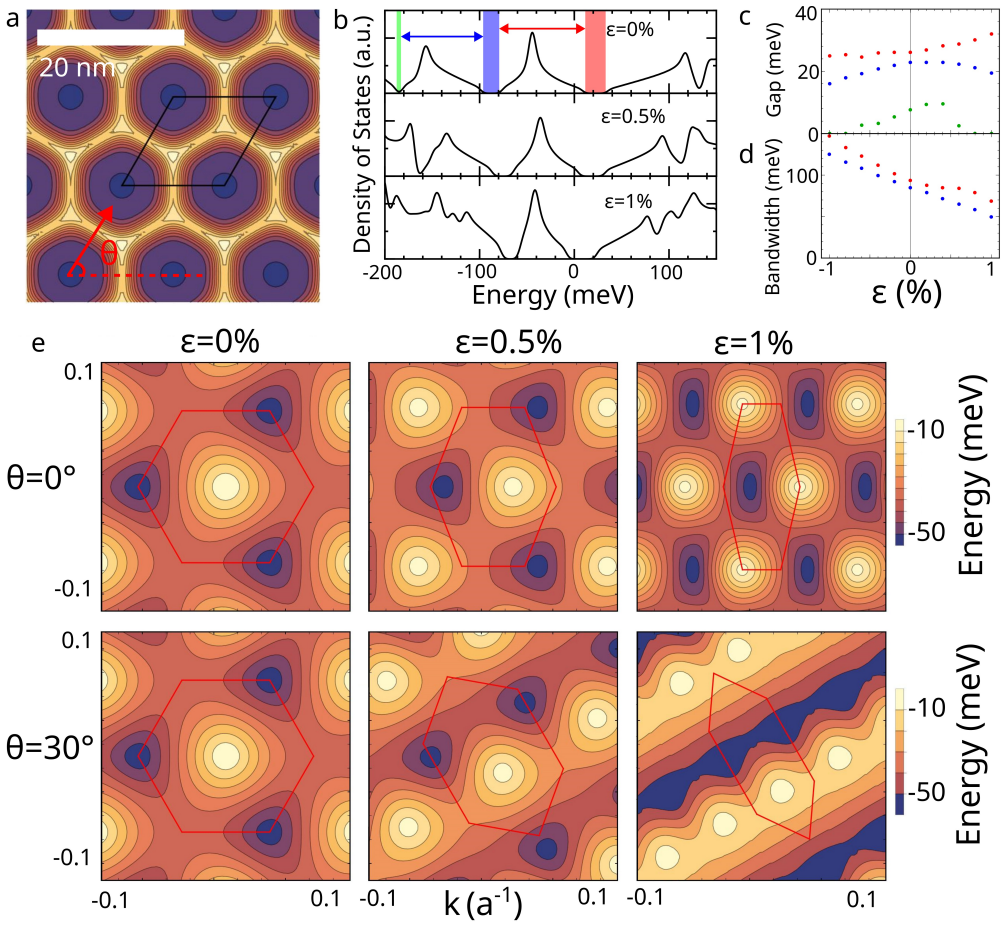

Figure 4.4: Aligned graphene-hBN theoretical band structure and DOS

A: Real space plot of moire superlattice showing the unit cell and strain angle orientation. **B:** Density of states plots for ϵ=0%, 0.5%, and 1% at ϕ=0°. Arrows and highlighted regions indicate gap and bandwidths for c and d. **C:** Primary, secondary, and tertiary gap size versus strain at ϕ=0. **D.** First and second hole miniband bandwidth versus strain at ϕ=0. **E.** Band structure contour plots of the first hole miniband for ϵ=0%, 0.5%, and 1% at ϕ=0° and ϕ=30°. Red hexagons show the moire Brillouin zones. Contour intervals are 10 meV

To analyze the effects of heterostrain on the electronic structure of the g-hBN moire, we theoretically calculate the band structure using a continuum model that includes lattice relaxation (Figure 4.4, details in the SI theory section). The simplest effect of the uniaxial

heterostrain is to shrink the moire Brillouin zone (BZ), reducing the carrier density per superlattice miniband. This results in a reduced bandwidth of the first hole miniband, which shrinks by 41.9% for 1% uniaxial strain applied along the graphene lattice vector (zero strain angle). Under the same strain conditions, the primary Dirac point gap grows by 22.7%, and the first hole superlattice gap decreases by 15.5%. Straining along different directions causes different changes to the gap sizes, but the primary and hole superlattice gaps remain open up to 1% strain, independent of strain angle. These basic theoretical results are in line with our experimental observations of the shifting of the superlattice resistance peak as strain increases the size of the moire unit cell. Because both the primary and hole-side superlattice gaps remain open as the graphene is stretched, the carrier density of the hole miniband remains at 4 electrons per superlattice unit cell, which is consistent with the match between our cryogenic transport measurements of the superlattice hole peak and the CAFM-extracted moire area. By contrast, the electron-side superlattice band edge remains gap-less with applied strain, consistent with our lack of observation of an electron-side superlattice resistance peak. Moreover, the decrease in bandwidth with uniaxial strain is consistent with the discrepancy with the moire area extracted from room temperature measurements as compared with CAFM and cryogenic measurements. At room temperature, thermal energy is a significant fraction of the bandwidth of the first hole miniband, with increased thermal excitation expected as the bandwidth is reduced with 1% heterostrain from 85 meV to 49 meV for zero strain angle (Figure 4.4).

Heterostrain introduces strong anisotropy in the graphene electronic structure, where the Fermi surface near the hole superlattice gap becomes stretched and can even become quasi one-dimensional due to the heterostrain. For zero strain angle, the anisotropy is apparent in the effective mass at the bottom of the hole miniband, where m_y/m_x $\sim$3.63, corresponding to the ratio of the effective mass in the direction of the strain versusperpendicular for 1% uniaxial strain and zero strain angle. This is contrasted with the Fermi surfaces around the primary Dirac point, which are less sensitive to the distorted moire and remain effectively

isotropic under the effects of the 1% graphene strain. For 30° strain angle, open Fermi surfaces dominate the electronic band structure for large heterostrain (Figure 4.4e). These open Fermi surfaces are strongly anisotropic and quasi-one-dimensional, where the Fermi velocity is limited to a range of directions along a preferred propagation direction.

4.1.6 Conclusion

In summary, we present a method to controllably introduce large heterostrain in a g-hBN device. The induced heterostrain is sufficiently homogenous to observe a modified electronic structure corresponding to the stretched moire pattern. These overall observations are in agreement with the reduced bandwidth and BZ size observed in theoretical calculations, which also predict that heterostrain should introduce anisotropy in the effective masses and open Fermi surfaces. In future studies, multi-terminal devices with different strain angles will be able to probe the effects of the anisotropic electronic structure. We note that even larger strain values are achievable locally using this technique, where we have observed local moire patterns ∼70 nm long correspond to ∼1.4% level strains (See SI Figure 4.12).

For this work, we used an AFM tip to set the strain in our devices, but we envision that other actuation methods such as bending, piezoelectric actuation, or thermal contraction can be used to achieve in-situ manipulation, even at cryogenic temperatures. Moreover, our methods should apply to other types of crystals supported on hBN, especially twisted graphene and transition metal dichalcogenide multilayers, where strain control can be used to controllably break the symmetry of moire patterns, manipulate the structure of pseudomagnetic fields and electronic flatbands, or alternatively be used as a method to reduce strain in a device unintentionally introduced by nanofabrication.

4.2 Materials and Methods

4.2.1 Sample Fabrication

Deterministic alignment of graphene-hBN samples

To maximize the impact of heterostrain on the size of the g-hBN moire pattern, the graphene must be aligned to the hBN, with the twist angle as close to zero degrees as possible. To reliably fabricate such aligned open-face g-hBN stacks, we developed a gold-based transfer technique and deterministically rotate the graphene into alignment using AFM nanomanipulation.

We begin by lithographically defining rectangular gold shapes (4 µm x 8 µm x 200 nm) on SiO_2 and picking them up with a PC stamp. To pick up the gold shapes, we typically heat to approximately 150C, so the PC melts and completely encases the gold shapes, then cool to room temperature and pick up slowly to reduce strain in the PC film. Next, we transfer the gold shapes onto graphene and perform an O_2 plasma etch to remove the exposed graphene (Figure 4.5a&b). At this stage, the gold-graphene stack is picked up with another PC stamp and transferred onto a bottom hBN substrate (Figure 4.5c).

To rotate the graphene, the Au is pushed laterally at one end with an AFM tip (Figure 4.6 a&b). This rotates the Au, and the friction between the Au and graphene rotates the graphene along with it (see AFM manipulation technique section). Near 0°, the g-hBN friction peaks due to increased atomic registry [4, 8, 10, 32] (Figure 4.6e). Ideally this friction exceeds the Au-graphene friction, causing the graphene to lock to the hBN and the Au to slide off of the graphene and leaving behind a well-aligned, clean, open-face g-hBN stack (Figure 4.6 c&d). In practice though, the g-hBN friction is not always enough to release the graphene from the Au by rotating. Often we find that it is necessary to halt the rotation at

the aligned g-hBN friction peak, then translate the Au off of the graphene.

A common failure when rotating or translating the Au off, is for the graphene to be torn from its edges. We speculate this is due to the edges of the graphene having bonded to the gold. Nevertheless, we found this process proved to be significantly more reliable in producing well-aligned (<0.5°), open-face devices as compared to simply aligning straight edges of the two flakes during the transfer process. Lastly, to further clean the surfaces and aid in further alignment we vacuum anneal the samples at 350C for 30 minutes.

Flexible electrode and handle contacts

We perform 2 steps of electron beam lithography (EBL) and metal vapor deposition, with the first step primarily to mechanically contact the graphene and the second to electrically contact.

Using EBL, we define a large contact on one side of the graphene which overlaps with the hBN. This will be the side of the graphene which is stationary and pinned to the hBN. On the other side of the graphene strip we define a rectangle in the interior of the graphene, so that it does not overlap with the hBN at all. This will be the handle which we will use to apply forces to the graphene. We then etch these features with an O_2 plasma. The etch is performed with a PE-25 plasma cleaner on low power (∼10W), with 15 SCCM of O_2 at 250 mTorr for 20s. We then deposit 5/95 nm of Cr/Au.

For the 2nd metal contact step we overlap the previous contacts in order to improve electrical contact to the graphene. On the handle side of the strip we write the electrode in a thin, serpentine shape in order to increase compliance and decrease friction for AFM manipulation. This deposition is also 5/95 nm Cr/Au.

AFM tip cleaning

Post device processing, the graphene will have substantial polymer residue on it which can interfere with CAFM imaging and is also a major source of disorder, broadening transport features. To clean the surface, we tip clean the sample with a Budget Sensors Multi75-G using a setpoint force between 5-15 nN. Before tip cleaning, superlattice peaks are typically not visible. After tip cleaning, the Dirac peak becomes sharper and the satellite peaks are clearly resolvable.

AFM cutting

We find that strain-induced tears tend to originate from nicks and sharp corners in the graphene. We remove these features by AFM cutting the graphene into a regular channel with rounded corners ($\sim$0.5 µm radius of curvature). We use AC local anodic oxidation[60] to cut the graphene in our Park NX10 AFM. We use a Nanoworld ARROW-EFM tip, 100 nN setpoint force, and 100 kHz, 20 Vpp tip bias.

Current annealing

Large contact resistances were observed in many of the devices. To decrease the contact resistance, we current anneal by voltage biasing while measuring the current with a Keithley 2400 source measuring unit to perform IV measurements. Typically the samples were current annealed up to 0.5 mA/µm [61]. After current annealing we observed significant reduction in the contact resistance and hysteresis.

4.2.2 Transport measurements

Two probe transport measurements were performed via current biasing with a 1 MΩ resistor at a frequency of 17 Hz and using an SRS830 lock-in amplifier to measure the voltage drop. At room temperature, current biases of 10 µA or 100 µA were used in order. At cryogenic temperatures, current biases of 100 µA or 1 µA were used.

For the g-hBN moire, the first hole doped satellite gap is larger than its counterpart on the electron doped side[56, 57]. At room temperature, thermal broadening and strain inhomogeneity often obscure the satellite resistance peak on the electron-doped side of the Dirac point. For this reason, and to minimize hysteresis which can occur at ambient conditions in a silicon-backgated sample, we typically constrain our room temperature gate sweeps to the hole-doped side.

4.2.3 AFM manipulation technique

We stretch our devices using the Lithography mode of our Park NX10 AFM with the 1200 kHz tip on the MikroMasch 4XC-NN probe. We choose this very stiff tip (100 N/m) for manipulations because softer tips often exceed the 10 V limit of our AFM photodiode when manipulating higher friction objects and stiffer tips exhibit less backlash when transitioning from static to kinetic friction. We first measure the height of the gold handle surface. For the manipulation, the Z piezo is set to ∼150 nm below the top surface of the gold handle, and the tip moves at 1 nm/s. During motions, we monitor and record both the AFM lateral deflection signal and the device resistance in order to better understand when the device begins moving. We have observed that friction for the initial motion is higher than for subsequent ones. This usually results in a large initial displacement on the order of 50 nm, which for short devices, is enough to immediately tear the graphene. For this reason, our first motion is to compress the device, so the initial large displacement does not rip the

graphene.

4.2.4 Conductive AFM

Our conductive AFM (CAFM) images are taken using the internal lock-in of our Park NX10 AFM. We apply an AC voltage to the sample and amplify the tip current signal using a FEMTO current amplifier. We use an ARROW-EFM tip with 50 nN setpoint force. Other tips, like the ARROW-NCPt work as well, but we prefer the ARROW-EFM because its lower spring constant makes it better suited for contact mode. These tips have a PtIr coating, and we have found that we are able to image moires with them for longer than TiIr coated tips, and much longer than Au or Pt coated tips.

We take several steps to account for the drift in our conductive AFM images and reduce its effects. First, we minimize the time per scan by using a relatively high scan rate of 15 Hz, taking small scale images (100x100 nm), and only taking 128 lines per scan. At each moire position, we sequentially record a forward and backward scan image and extract a thermal drift velocity by comparing the differences in the extracted moire lattice vectors. With this information we can correct for the effects of the drift in each image. Additional details can be found in the SI AFM drift correction section.

4.2.5 Moire FFT strain fitting

To determine the strain parameters from the g-hBN moire patterns, we adapted a fitting approach from Tran et al[62]. The code generates graphene and hBN lattice vectors, transforms them via a global rotation, a relative g-hBN rotation, and a uniaxial strain. From these transformed lattice vectors we can generate the moire lattice vectors, and iteratively adjust rotation angles and strain to match the moire lattice measured from CAFM images.

We use $a_G = 0.246$ nm and $a_{hBN} = 0.2504$ nm for the graphene and boron nitride lattice constants, respectively, and a graphene Poisson ratio = 0.16 [63, 64].

4.2.6 Error Analysis

To estimate the uncertainty for the extracted device parameters, we numerically invert functions for calculating the twist angle, strain and strain angle parameters for a given set of moire wavevectors. We assume a 1% error in the moire wavevectors, and report the max and min range of the resulting calculated parameters as the uncertainty values in the main text. We estimate a 1% error in the FFT position from the reproducibility of repeated CAFM moire imaging in a single position (See SI Figure 4.10: AFM moire wavelength reproducibility).

4.3 Supplementary Information

4.3.1 Sample fabrication figures

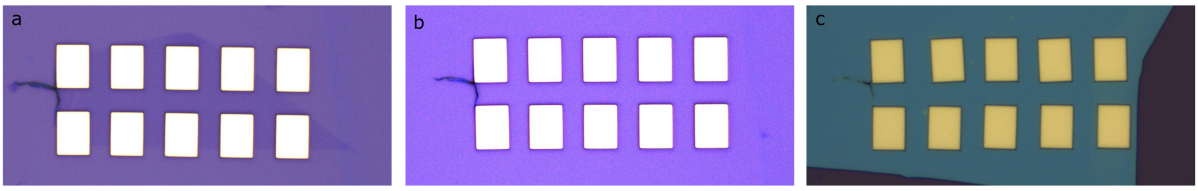

Figure 4.5: Optical images of gold based transfers

a: 200 nm thick gold shapes transferred onto a graphene flake. Shapes are 8 µm x 6 µm **b:** After oxygen plasma etching to etch away exposed graphene **c:** Etched gold-graphene stack transferred onto bottom hBN flake and ready to be aligned by performing AFM manipulations

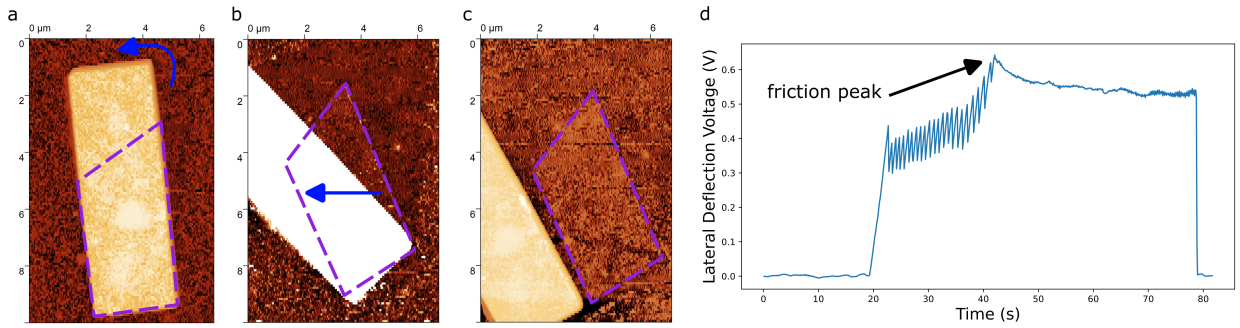

Figure 4.6: Deterministic alignment of graphene to hBN substrate

a-d: Sequence of AFM topography images of gold-graphene on hBN during the AFM manipulations to rotate the graphene into alignment, purple dashed lines outline the graphene. Blue arrows indicate positions where the gold shape is pushed with the AFM tip. **d** is the final result after sliding the gold off of the aligned graphene-hBN **e:** Lateral AFM deflection voltage vs time for the manipulations done in a (blue) and b (orange). As the graphene gets rotated into alignment with the hBN, there is a peak in the voltage signal and the gold slips off.

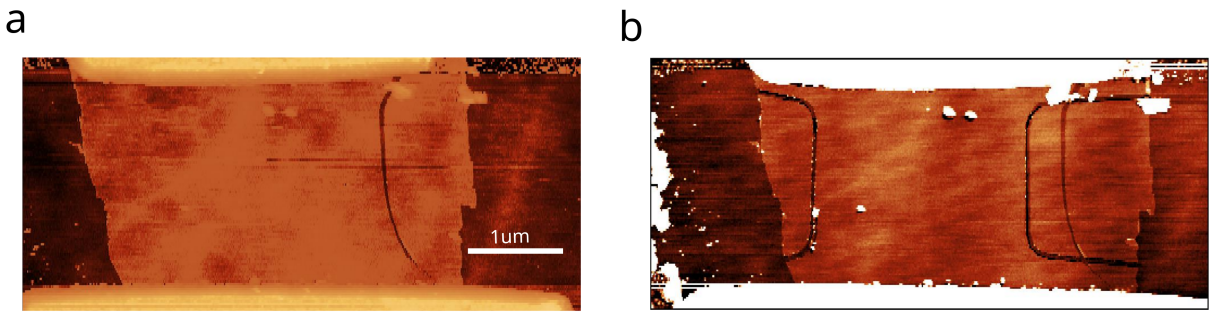

Figure 4.7: Device E before (a) and after (b) AFM cutting

4.3.2 AFM image of torn graphene device

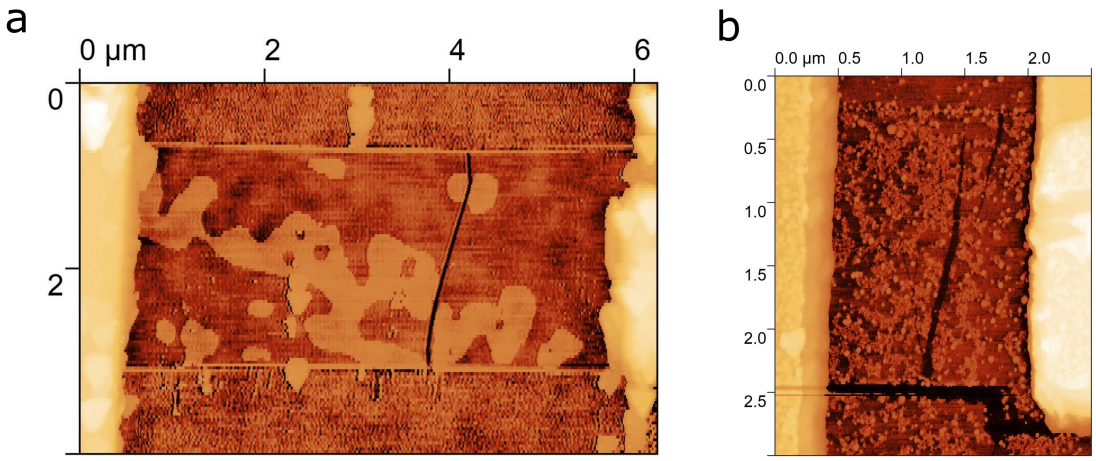

Figure 4.8: Torn graphene-hBN devices

a,b: Graphene strips tore due to being stretched. Close inspection of **(a)** showed it tore at a nick in the edge.

4.3.3 Unaligned G-BN strain Raman signal

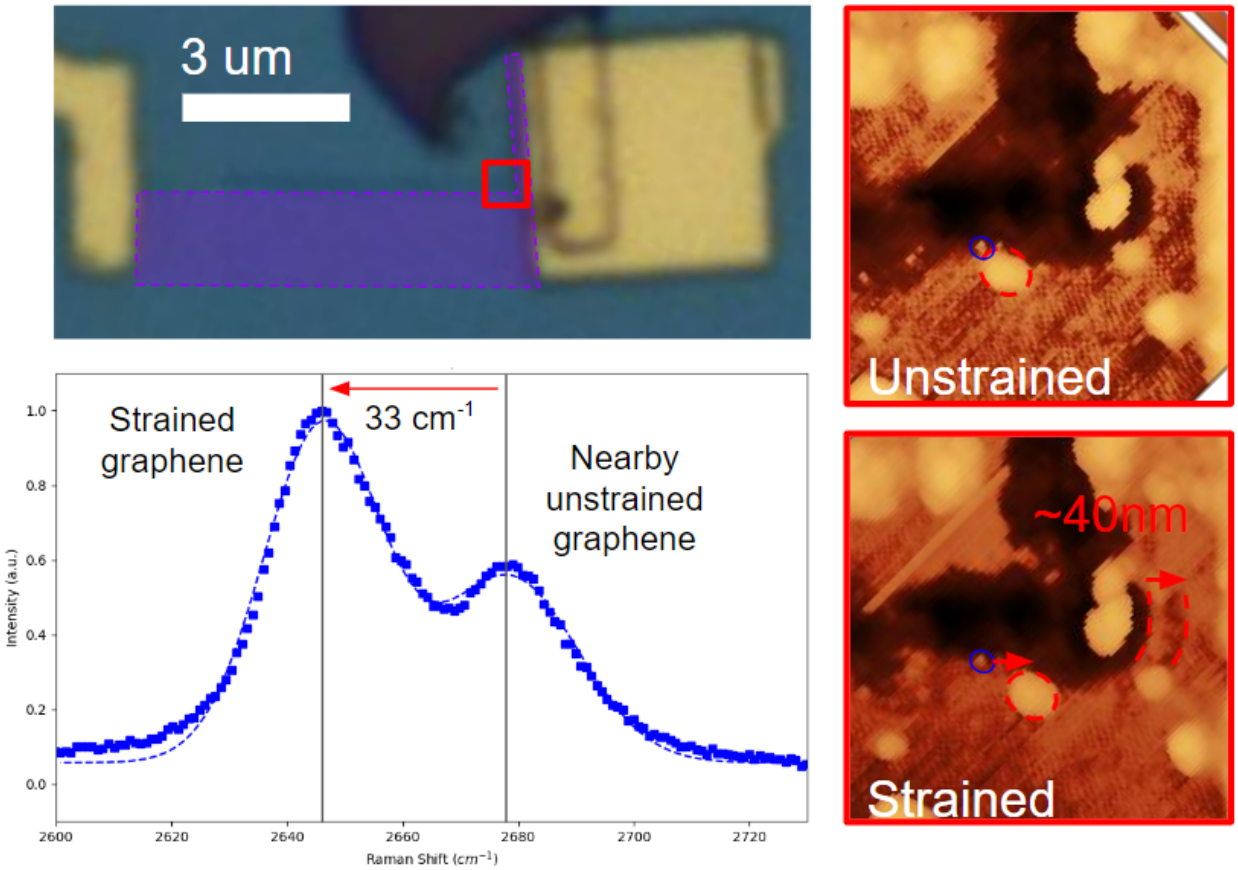

Figure 4.9: Stretching and Raman of unaligned G-hBN

a: Optical image of unaligned G-hBN device. Graphene strip highlighted in purple **b:** Raman signal from strained graphene. Spot size also includes an adjacent, unstrained graphene strip. 33 cm^{-1} shift corresponds to 0.61% graphene strain [48] **c:** AFM image of graphene corner before motion **d:** AFM image of graphene corner after motion, showing ∼40 nm displacement relative to hBN substrate. 40 nm displacement for a ∼6.78 µm long strip corresponds to 0.59% strain. This agrees well with the Raman signal

4.3.4 AFM drift correction

We model the drift in our AFM images as follows: For a square image with dimension d taken at scan rate f, the time elapsed between 2 points in a scan is:

$$\Delta t = \frac{\Delta x}{d}\frac{1}{2f} + \frac{\Delta y l}{d}\frac{1}{f}$$

d = Image dimension f = scan rate

l = number of lines in the slow direction

x = x position or size y = y position or size

Given 2 vectors **a** and **b**, one from an image taken top-to-bottom and the other taken bottom-to-top, the drift velocity, v, can be calculated, assuming it is constant for the duration of the 2 scans. Both vectors are an attempt to measure the same true feature in the image, but are distorted due to the drift, and thus each differ from the true feature by an offset $\Delta\mathbf{a}$ and $\Delta\mathbf{b}$ (the offsets are different from each other because **a** and **b** are different lengths, and thus different have different elapsed times, meaning different displacements).

$$\vec{a} + \Delta\vec{a} = \vec{b} + \Delta\vec{b} \tag{4.1}$$

The drift velocity can then be calculated from this offset and from the time it took to measure a. We know how much time elapsed between any two points in the AFM image, Δt, from above. And the distance the AFM has drifted in that time is $\Delta\mathbf{a}$.

$$\vec{v} = \Delta\vec{a}\left(\frac{a_x}{d}\frac{1}{2f} + \frac{a_y l}{d}\frac{1}{f}\right)^{-1} \tag{4.2}$$

The same is also true for **b**.

$$\vec{v} = \Delta\vec{b}\left(\frac{b_x}{d}\frac{1}{2f} + \frac{b_y l}{d}\frac{1}{f}\right)^{-1} \tag{4.3}$$

Equations 4.1, 4.2, and 4.3 form a system of equations whose solutions are the drift velocity and offsets. We get 2 systems of equations from each pair of images, one from the a1 vector and one from a2. Performing this analysis on all of the moire AFM data we present in this paper, we find a relatively low drift: in the y direction 0.08±0.16 nm/s and in the x direction 0.00±0.04 nm/s corresponding to a 1±2 nm drift over the course of a single scan. There is significant spread which we attribute to having the AFM piezo scanners warmed up to different extents between measurements and other thermal effects.

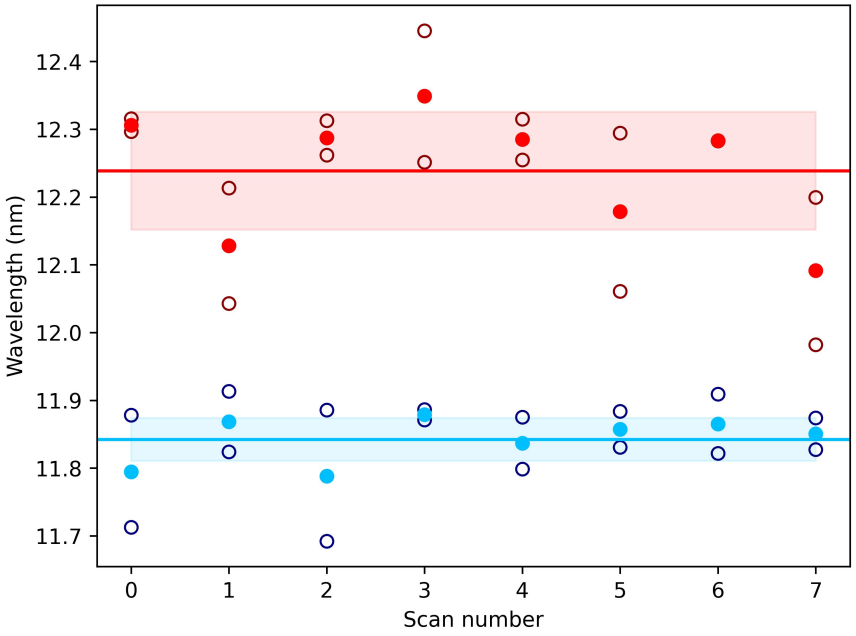

Figure 4.10: AFM moire wavelength reproducibility

8 pairs of images taken sequentially at the same position over the course of 8 minutes. Even pairs consist of one image with the slow direction upwards and one downward; odd pairs have one rightwards and one leftwards. This explains the alternating spread in uncorrected wavelength. Dark, hollow markers are moire wavelengths from the 2 uncorrected images, and light, solid markers are the corrected values. The mean and standard deviation of the corrected values are shown with the horizontal lines and shaded areas, which are 12.24 ± 0.09 nm and 11.84 ± 0.03 nm. This corresponds to a 0.7%, 0.3% spread in the moire wavelength.

We calibrate our AFM's XY scanner using an etched SiO_2/Si calibration standard provided by Park Systems by taking a 50x50 µm image of the 5 µm pitch standard.

4.3.5 Uniaxial heterostrain model and fitting

We transform the real space graphene unit vectors with a rotated strain matrix:

$$I + R(\phi)SR^T(\phi)\vec{G}$$

Which is then rotated by the graphene-hBN twist angle, θ: $R(\theta)(I + R(\phi)SR^T(\phi)\vec{G})$

This result and the hBN unit vectors are rotated by a global twist angle. Their reciprocal lattice vectors are calculated. And the moire reciprocal lattice vectors are calculated by subtracting the rotated hBN reciprocal lattice vector from the stretched/rotated graphene reciprocal lattice vector.

I is the identity matrix, and R and S are defined as follows:

$$R(\theta) = \begin{pmatrix} cos(\theta) & -\sin(\theta) \\ sin(\theta) & cos(\theta) \end{pmatrix}, \qquad S = \begin{pmatrix} \epsilon & 0 \\ 0 & -0.16\epsilon \end{pmatrix}$$

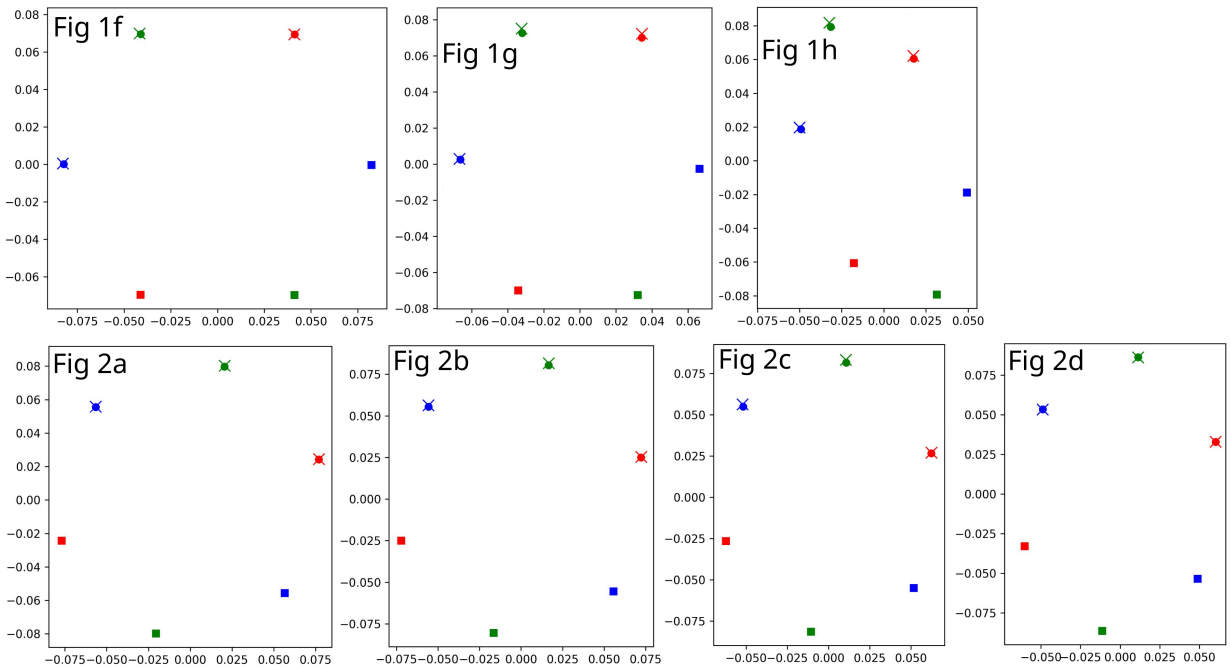

Figure 4.11: Moire peak fitting

Moire fits from the CAFM images of main text figures. Solid circles are the peak positions measured from the FFTs of CAFM moire images; solid squares are the same peaks inverted; crosses are the fitted peak positions using a uniaxial strain model to fit the measured peaks. The largest discrepancies in fitting result from the images which appear to require some biaxial strain to fit, such as Fig 1f&g. 85% of our moires can be fit to within 1% of the measured FFT peaks, and >99% can be fit to within 5%.

	Uniaxial strain ϵ (%)		**Graphene-hBN twist θ (°)**		**Strain angle wrt graphene ϕ_G (°)**		**Global twist θ_{global} (°)**		**Strain angle wrt horizontal ϕ (°)**	
Fig 1f	0.043	+0.024 -0.018	-0.12	+0.147 -0.112	50.6	+20.172 -17.069	30.6	+6.552 -8.621	81.2	+17.759 -19.483
Fig 1g	0.336	+0.023 -0.015	0.021	+0.112 -0.129	-26.0	+3.793 -5.172	27.2	+7.862 -7.034	1.2	+5.310 -3.931
Fig 1h	0.805	+0.021 -0.011	0.017	+0.103 -0.131	-6.9	+3.586 -4.690	24.0	+9.176 -7.059	17.1	+4.487 -3.473
Fig 2a	0.074	+0.026 -0.019	0.019	+0.117 -0.159	-12.3	+10.345 -11.724	345	+9.310 -6.552	-27.3	+11.379 -10.690
Fig 2b	0.142	+0.017 -0.017	0.009	+0.117 -0.145	10.97	+6.207 -6.207	-13.035	+8.621 -6.552	-2.065	+6.552 -6.552
Fig 2c	0.333	+0.022 -0.016	0.008	+0.117 -0.131	15.631	+3.793 -4.483	-10.92	+7.931 -7.241	4.711	+4.828 -4.138
Fig 2d	0.426	+0.022 -0.022	-0.176	+0.059 -0.045	-0.447	+2.241 -1.897	2.135	+2.586 -3.621	1.688	+2.069 -2.414
Fig 2e	0.05	+0.026 -0.018	0.02	+0.117 -0.131	18	+14.483 -15.862	-13	+7.759 -6.724	5	+16.724 -13.966
Fig 2e	0.1	+0.022 -0.016	0.02	+0.112 -0.147	18	+7.759 -7.759	-13	+8.207 -6.276	5	+8.241 -7.276
Fig 2e	0.2	+0.026 -0.016	0.02	+0.103 -0.159	18	+5.241 -5.793	-13	+9.31 -5.862	5	+6.000 -5.310
Fig 2e	0.3	+0.023 -0.015	0.02	+0.117 -0.145	18	+4.345 -5.172	-13	+8.690 -7.034	5	+4.759 -3.931
Fig 2e	0.4	+0.018 -0.013	0.02	+0.103 -0.131	18	+3.621 -4.103	-13	+7.862 -6.207	5	+4.241 -3.207

Table 4.1: Parameters and uncertainties for main text figures

The uncertainties correspond to a 1% error in the moire FFT peak position. The rows for Fig 2e each use the average twist angle, strain angle, and global rotation angle for the Fig 2e data with several uniaxial strain values in order to estimate the uncertainty throughout the data range.

4.3.6 CAFM and strain data from other devices

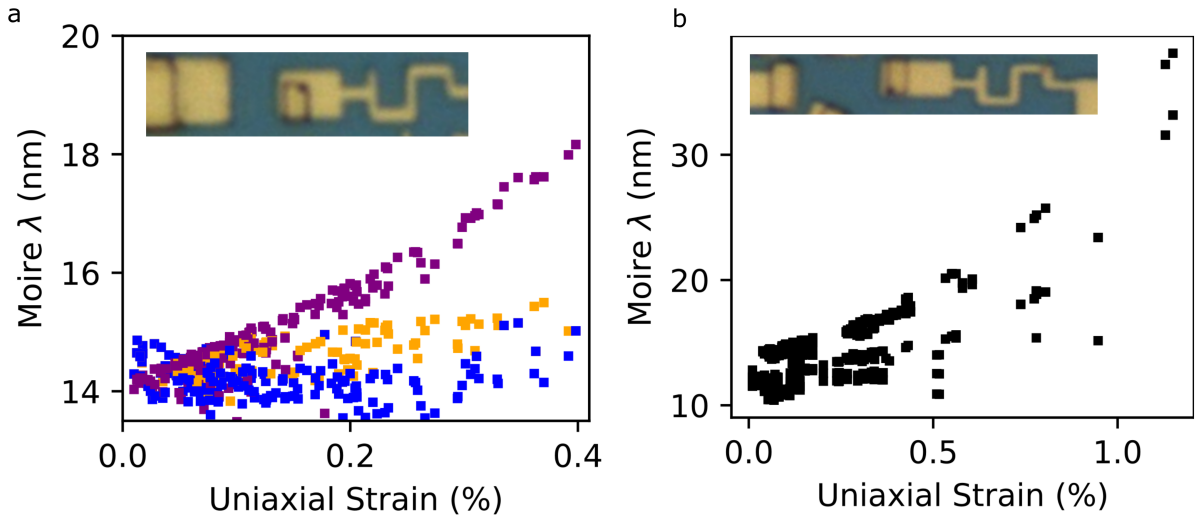

Figure 4.12: Moire wavelength versus strain for Device C (left) and Device A (right) Data for Device A are not differentiated by color because the twist inhomogeneity and high strain make different moire vectors difficult to distinguish.

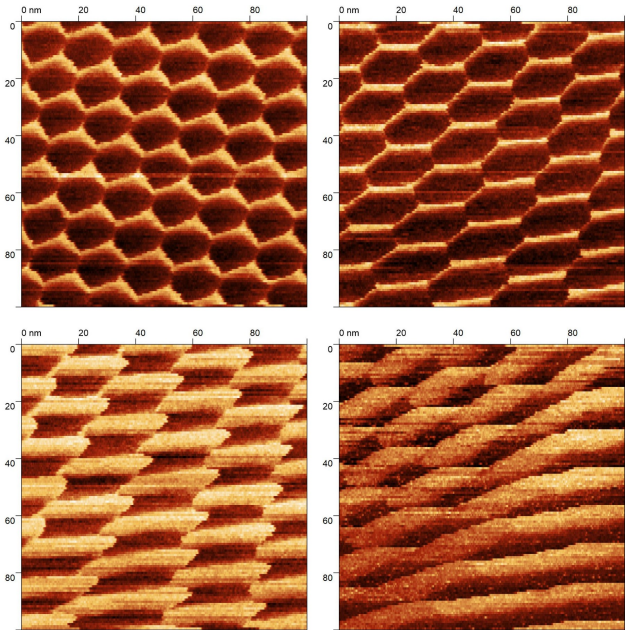

Figure 4.13: Extreme moire heterostrain in Device A

CAFM moire images of Device A, our most strained sample. Note it has a high degree of strain inhomogeneity, as evidenced by the varying moire size within the right and bottom pairs of images.

4.3.7 Satellite Dirac peak temperature dependence

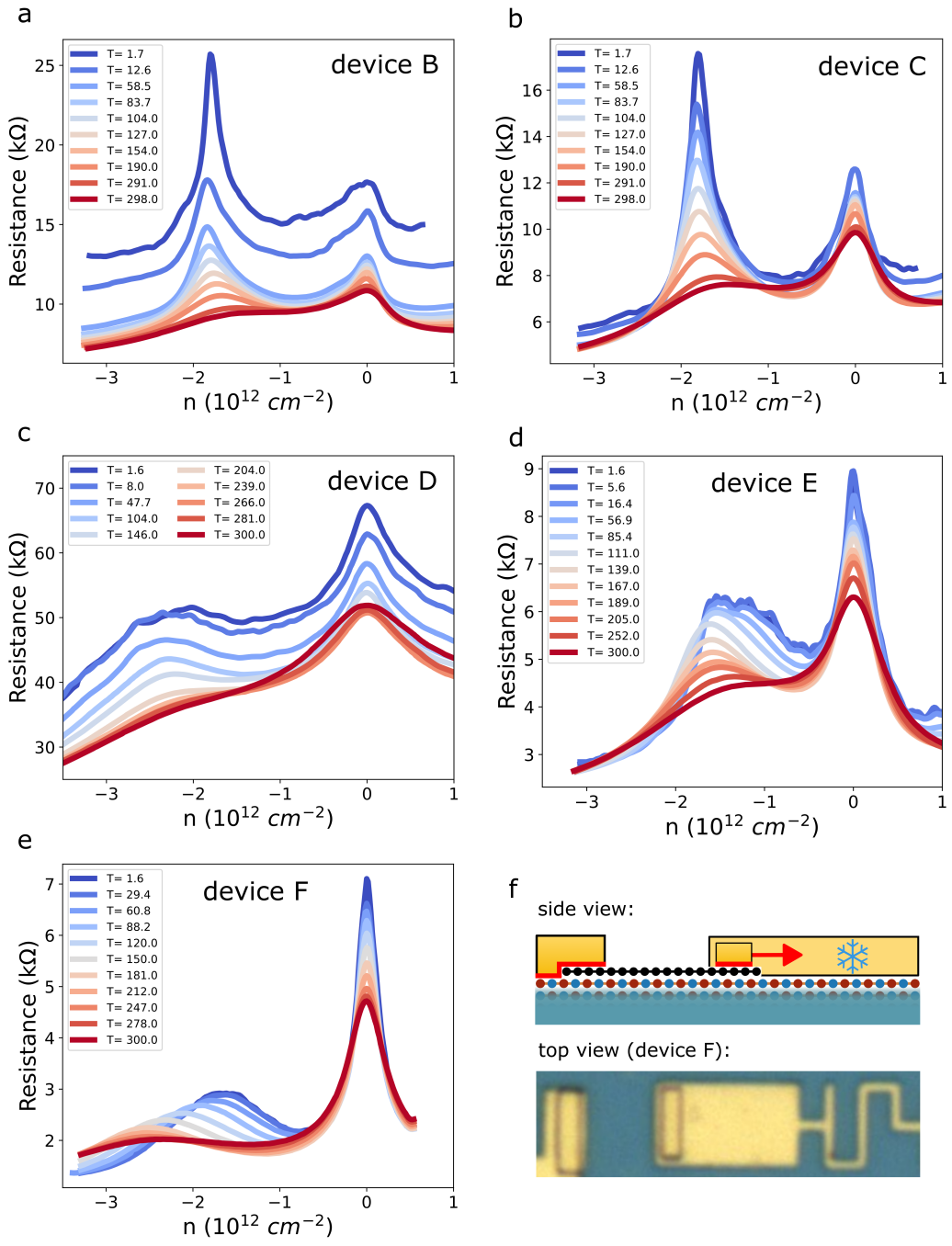

Figure 4.14: Temperature dependent gate sweeps for various devices
a-e: Temperature dependent gate sweeps for 5 separate devices. Red to blue color scale corresponds to temperatures from 300K to 1.6K. **f:** Side view schematic indicating thermal contraction of the anchor with temperature and top view optical image of device F.

Device	Anchor (μm)	Channel (μm)	Ratio
B	1.5	3	0.5
C	1.5	4	0.375
D	1.5	4.5	0.33
E	1.3	2.7	0.48
F	5.2	3.2	1.625

Table 4.2: Table of the device dimensions presented in Figure 4.14

Upon cooling, the superlattice peak for most of our devices shifts outward, to higher densities (Figure 4.14a-d). This effect is also observed in twisted bilayer graphene[46, 54] and is discussed in the main text. However, for one device, the dependence is opposite, exhibiting an overall shift to lower densities and larger superlattice unit cells as the sample is cooled to 1.6K. This suggests that the graphene is being stretched as it is cooled down. We attribute this effect to thermal contraction of the anchoring drain electrode, which should have a large effect for this device as the metal anchor is ∼1.75x the length of the graphene channel (Figure 4.14f). The anchor is held only by its friction with the hBN, so we expect it to contract inward equally on all sides. From 293K to 4K the relative contraction of gold is ∼0.3% [65], so the graphene should receive an additional strain of 0.3% *1.75/2 = ∼0.28%. This is a substantial amount of thermally-induced strain. By contrast, the other devices that do not exhibit thermal contraction effects have a metal anchor that is only half the length of the graphene channel, which would result in a 3.5x smaller thermally-induced strain (0.075%).

In addition, variations in the O_2 plasma etch performed on the electrodes lead to different levels of friction with the graphene. In some cases, this results in slipping and a lack of one-to-one motion during manipulations, as was the case for the devices B and C presented in Figure 4.3 of the main text. Consequently, significantly larger motions (∼100x) of the handle were necessary to impart strain. This provides further reasoning as to why for these devices we do not observe a decrease in carrier densities due to the thermal contraction of the anchors upon cooling.

4.3.8 Additional magnetotransport

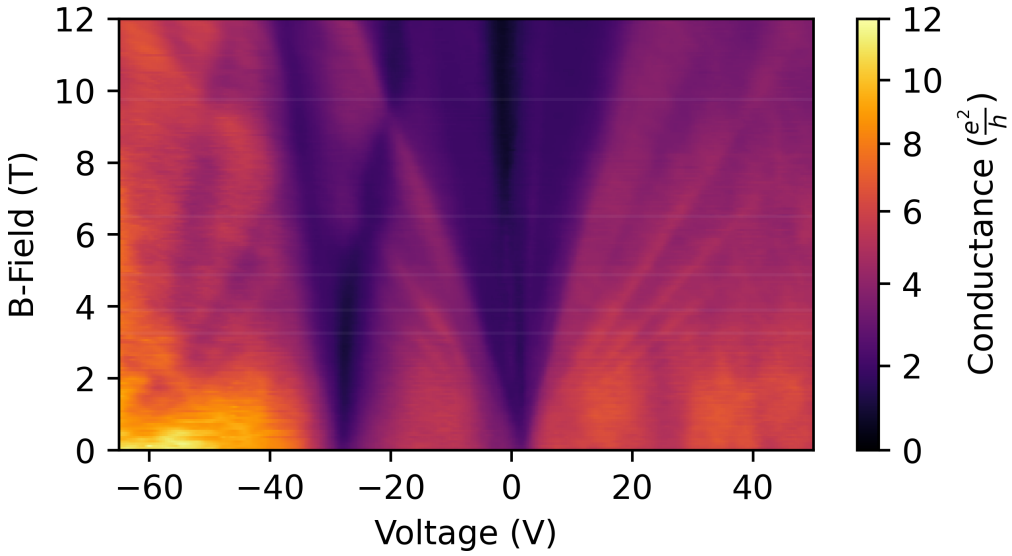

Figure 4.15: 1.6K magneto transport of device B

Before cooling down, the sample had an average: uniaxial strain of 0.35±0.05%, twist angle of 0.01±0.05°, and strain angle of 14±8° with respect to the graphene lattice vector where the uncertainties are the standard deviation from the CAFM dataset. A constant resistance value of 10.54 kΩ is subtracted to align the ν=2 plateau at $2e^2/h$.

4.3.9 Additional theory

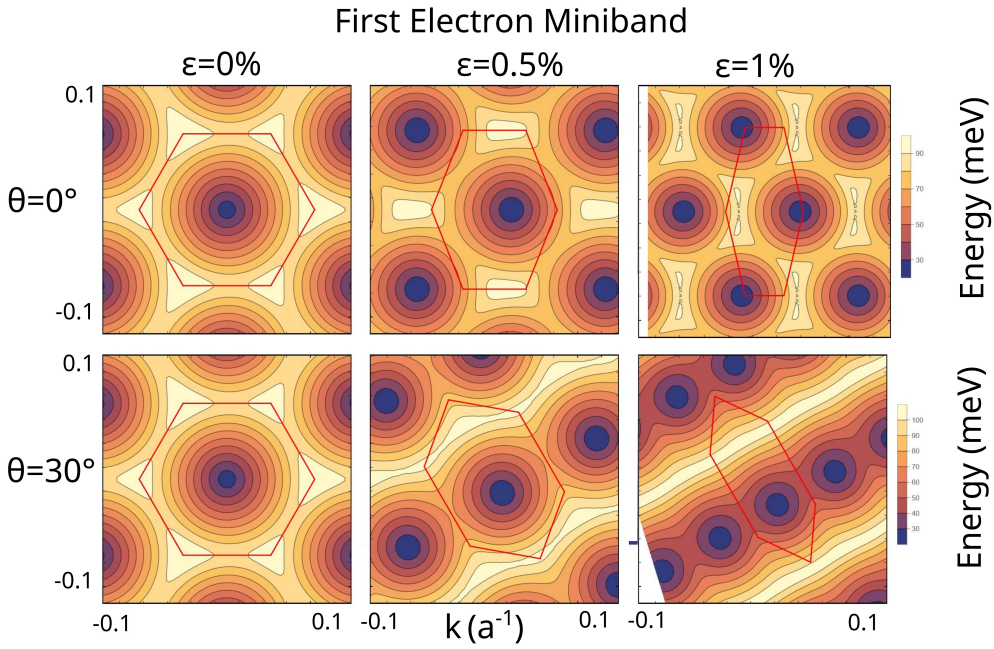

Figure 4.16: Contour plots of first electron mini band

Contour intervals are 10meV

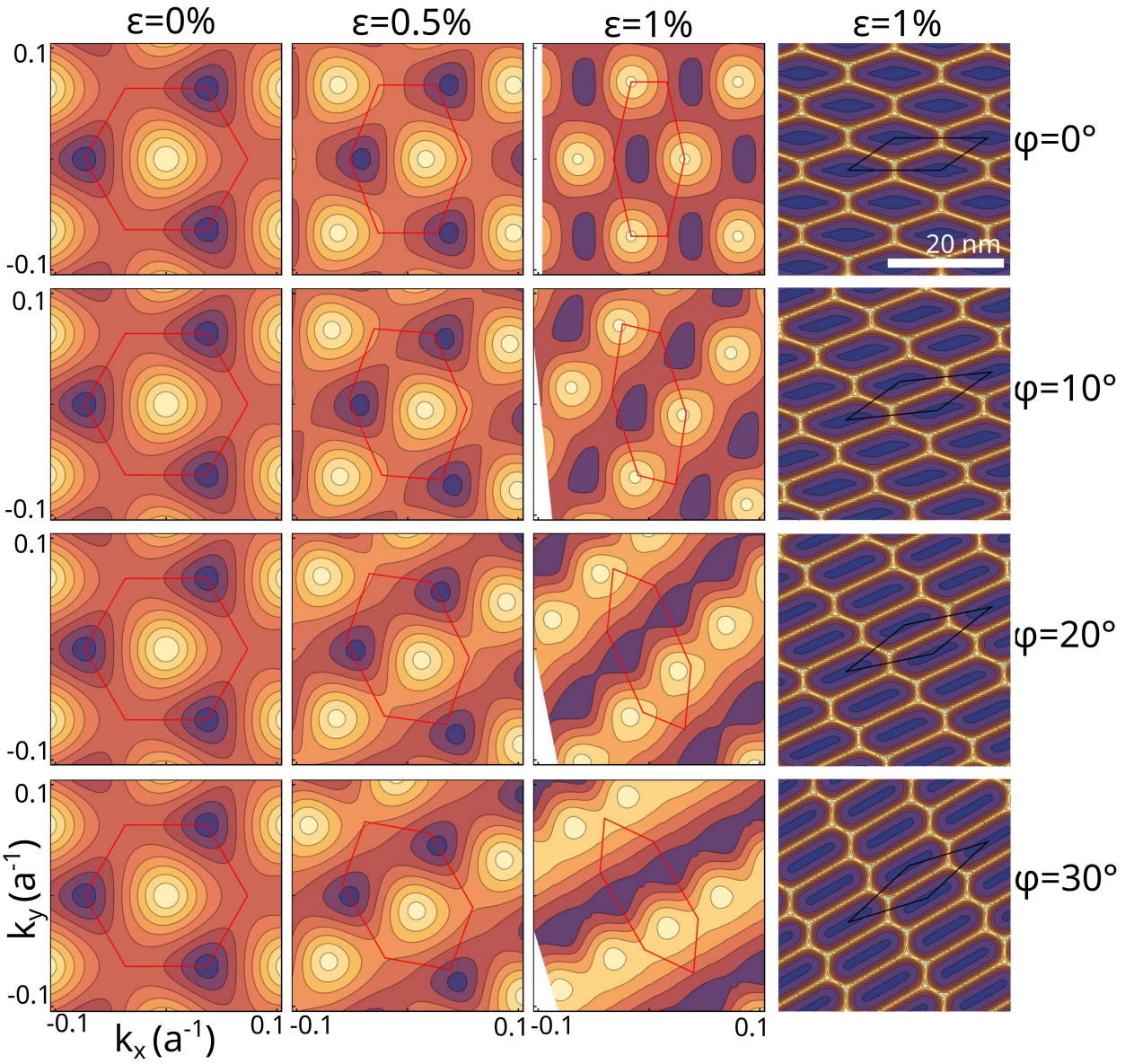

Figure 4.17: First hole mini band contours dependence on strain angle

Contour intervals are 10 meV. The right column shows the real space moire structure for 1% strain.

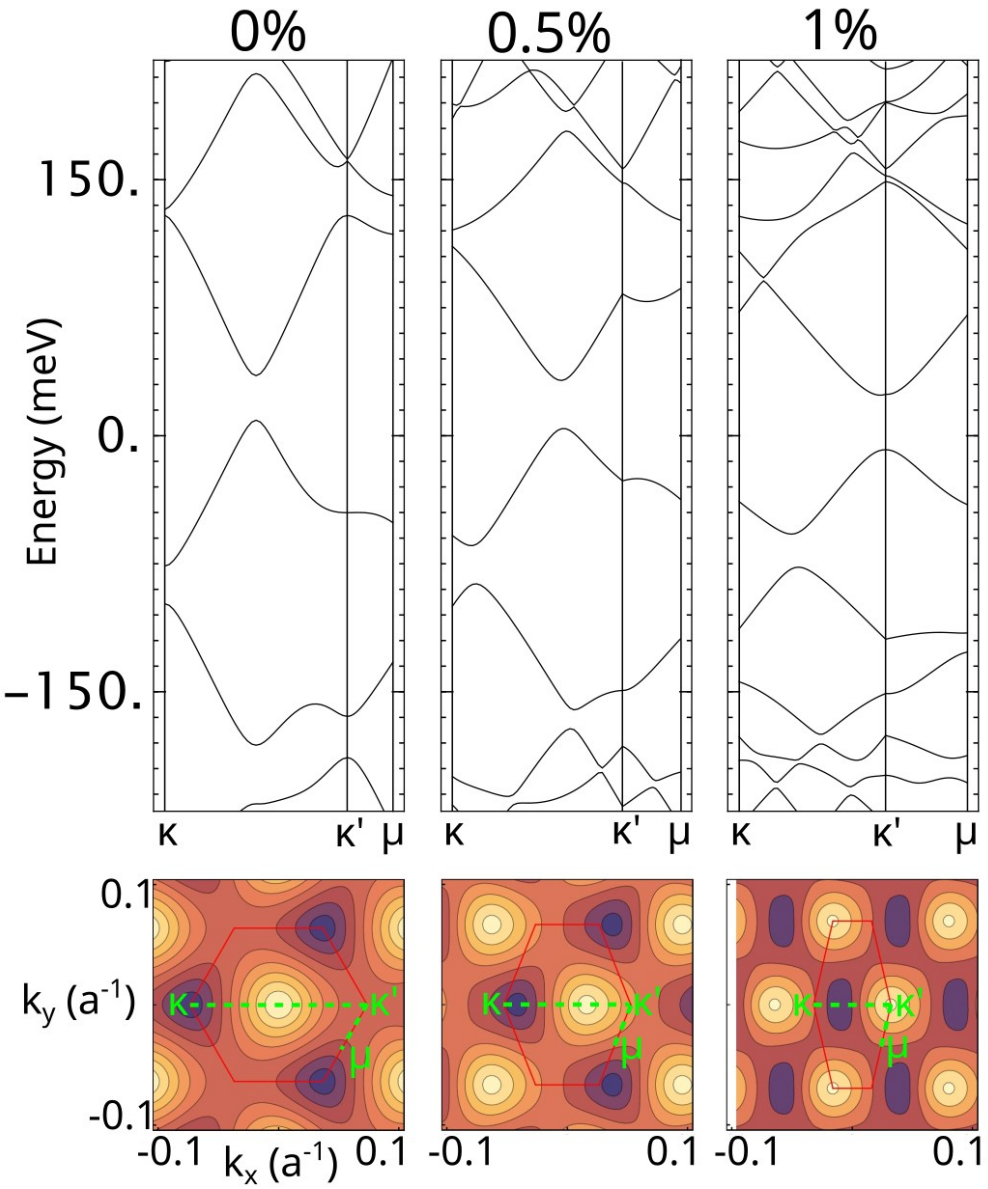

Figure 4.18: Band structure cuts for several strain values at 0° strain angle

Upper plots are band structure cuts following the green dashed line in the 2D contour plots below. Contour intervals are 10 meV.

4.3.10 Detailed theory methods

In our theoretical calculation, we assume that only graphene has a uniform strain that is independent of real-space. Each strain is characterized by the two parameters: the strain

strength ϵ and strain angle ϕ. We set $\phi = 0$ to align with the zigzag direction of moiré hexagonal pattern of g-hBN. The moiré pattern of strained g-hBN is defined by $\boldsymbol{G}_j = \boldsymbol{b}_j - \boldsymbol{b}'_j$, where $\boldsymbol{b}_j$, $\boldsymbol{b}'_j$ and $\boldsymbol{G}_j$ are the reciprocal lattice vector of the strained graphene, hBN, and moiré lattice respectively. The moiré real lattice vector is given by $\boldsymbol{G}_i \cdot \boldsymbol{L}_j = 2\pi\delta_{ij}$.

To investigate the relaxed lattice structure of the strained g-hBN, we apply the continuum method [66, 67]. For the analysis of electronic properties, we employ the continuum Hamiltonian with relaxation[68, 69]. The details of the calculation are presented in the Supplementary Material.

Moiré pattern

In this section, we define the moiré pattern for strained graphene/hBN. We consider the bilayer system constructed by monolayer graphene and hBN. We take the xy-plane in the layers and the z-axis along their perpendicular direction. The lattice constant of graphene and hBN are $a = 0.246$ nm and $a_{hBN} = 0.2504$ nm respectively.

Before we derive moiré lattice of strained graphene/hBN, we briefly review moiré pattern the non-strained case. We consider that hBN is rotated by θ relative to graphene. The lattice vector of graphene are defined as $\boldsymbol{a}_1^0 = a(1, 0)$ and $\boldsymbol{a}_2^0 = a(1/2, \sqrt{3}/2)$, and for hBN, it is written as $\boldsymbol{a}'_j = R(\theta)(a_{hBN}/a)\boldsymbol{a}_j^0$ for $j = 1, 2$ where $R(\theta)$ is the 2d rotation matrix. The reciprocal lattice vector are given by $\boldsymbol{b}_1^0 = (4\pi/\sqrt{3}a)(\sqrt{3}/2, -1/2)$ and $\boldsymbol{b}_2^0 = (4\pi/\sqrt{3}a)(0, 1)$ for graphene, and $\boldsymbol{b}'_j = R(\theta)(a/a_{hBN})\boldsymbol{b}_j^0$ for hBN. The corner of B.Z. of graphene and hBN are written as $\boldsymbol{K}_\xi = \xi(2\boldsymbol{b}_1^0 + \boldsymbol{b}_2^0)/3$ and $\boldsymbol{K}'_\xi = R(\theta)(a/a_{hBN})\boldsymbol{K}_\xi$ respectively.

While the system generally has a commensurate moiré period at the specific twist angle, for an angle small enough, we can define the incommensurate moiré period by $\boldsymbol{G}_j^0 = \boldsymbol{b}_j^0 - \boldsymbol{b}'_j$ for $j = 1, 2$. The moiré lattice vector $\boldsymbol{L}_j$ is given from $\boldsymbol{G}_i^0 \cdot \boldsymbol{L}_j^0 = 2\pi\delta_{ij}$. The angle between

$\boldsymbol{L}_1^0$ and x-axis is

$$\phi_M = \arctan\left(\frac{-\sin\theta}{1+\delta-\cos\theta}\right), \tag{4.4}$$

where $\delta = (a_{hBN} - a)/a$.

Next, we move to the case of strained Graphene/hBN. In this model, we ignore the strain on hBN because the strain of graphene is more dominant for electronic properties around the fermi energy.

The primitive lattice vector of strained monolayer graphene is given by $\boldsymbol{a}_j = (1+\mathcal{E})\boldsymbol{a}_j^0$, and the reciprocal lattice vector is $\boldsymbol{b}_j = (1+\mathcal{E})^{-1,t}\boldsymbol{b}_j^0$, where

$$\begin{aligned}
\mathcal{E} &= \begin{pmatrix} \epsilon_{xx} & \epsilon_{xy} \\ \epsilon_{xy} & \epsilon_{yy} \end{pmatrix} \\
\epsilon_{xx} &= \epsilon\left[\cos^2(\phi+\phi_M) + \nu_P \sin^2(\phi+\phi_M)\right] \\
\epsilon_{yy} &= \epsilon\left[\nu_P \cos^2(\phi+\phi_M) + \sin^2(\phi+\phi_M)\right] \\
\epsilon_{xy} &= \epsilon\,(1+\nu_P)\sin(\phi+\phi_M)\cos(\phi+\phi_M).
\end{aligned} \tag{4.5}$$

is the strain matrix. ϵ and ϕ are the strength and direction of the strain. $\nu_P = 0.16$ is the Poisson's ratio of monolayer graphene[63, 64]. We set $\phi = 0$ to align to L_1^0 at each twist angle. $\phi = 60°$ gives the same moiré pattern of $\phi = 0°$ due to C_{2z} symmetry of the strain matrix (4.5) and C_{3z} symmetry of non-strained graphene/hBN. Therefore we only consider ($0° \leq \phi < 60°$) in this model.

The moiré reciprocal lattice vector for the strained Graphene/hBN can be defined by

$$\begin{aligned}\boldsymbol{G}_j &= \boldsymbol{b}_j - \boldsymbol{b}'_j \\ &= \left[(1+\mathcal{E})^{-1,t} - \left(\frac{a}{a_{hBN}}\right) R(\theta)\right] \boldsymbol{b}_j \end{aligned} \tag{4.6}$$

for each strain parameter ϵ and ϕ. The moiré lattice vector is given by $\boldsymbol{G}_i \cdot \boldsymbol{L}_j = 2\pi\delta_{ij}$.

Continuum method for lattice relaxation

For each strain parameter ϵ and ϕ, we calculate the optimized lattice structure by using the continuum method[66, 67] while keeping the strained moiré unit cell.

We define the displacement vector of each atom as $\boldsymbol{u}(R^(l)_X)$, where $\boldsymbol{R}^{(l)}_X$ is the atom position of the sublattice $X(= A, B)$ in layer l. When moiré period is long enough relative to the atomic length scale, the displacement vector $\boldsymbol{u}$ smoothly varies in the moiré length scale. As a result, we can adapt the continuum approximation for the displacement vector and we can replace it as the continuum function of real space $\boldsymbol{u}(R^{(l)}_X) \to \boldsymbol{u}^{(l)}(\boldsymbol{r})$.

We introduce the total lattice energy as the function of the displacement vector $U = U[\boldsymbol{u}^{(1)}(\boldsymbol{r}), \boldsymbol{u}^{(2)}(\boldsymbol{r})] = U_B + U_E$, and the optimized lattice structure is given by solving $\partial U/\partial u^{(l)}_\mu = 0$. U_B is the binding energy between layers

$$U_B = \int \mathrm{d}^2\boldsymbol{r} \sum_{j=1}^{3} 2V_0 \cos\left[\boldsymbol{G}_j \cdot \boldsymbol{r} + \boldsymbol{b}^0_j \cdot \left(\boldsymbol{u}^{(2)} - \boldsymbol{u}^{(1)}\right) + \psi_0\right], \tag{4.7}$$

where $\boldsymbol{b}^0_3 = -\boldsymbol{b}^0_1 - \boldsymbol{b}^0_2$, $\boldsymbol{G}_3 = -\boldsymbol{G}_1 - \boldsymbol{G}_2$. We take $V_0 = 0.202$ eV/nm^2 and $\psi_0 = -0.956$ [67]. We ignore the constant term of the binding energy because it disappears on the equation $\partial U/\partial u^{(l)}_\mu = 0$.

The elastic energy U_E is written in a standard form [70, 71] as

$$U_E = \sum_{l=1}^{2} \frac{1}{2} \int \Big[\left(\mu^{(l)} + \lambda^{(l)}\right) \left(u_{xx}^{(l)} + u_{yy}^{(l)}\right)^2 + \mu^{(l)} \left\{ \left(u_{xx}^{(l)} - u_{yy}^{(l)}\right)^2 + 4 \left(u_{xy}^{(l)}\right)^2 \right\} \Big] \mathrm{d}^2\boldsymbol{r}, \tag{4.8}$$

where $\lambda^{(1)} = 3.25$ eV/Å^2 and $\mu^{(1)} = 9.57$ eV/Å^2 are graphene's Lamé factors, and $\lambda^{(2)} = 3.5$ eV/Å^2 and $\mu^{(2)} = 7.8$ eV/Å^2 are for hBN[57, 72, 73]. $u_{ij}^{(l)} = (\partial_i u_j^{(l)} + \partial_j u_i^{(l)})/2$ is the strain tensor. Here we ignore the elastic energy caused by the strain matrix because it only gives a constant term due to the uniformity of strain.

To solve the equation $\partial U/\partial u^{(l)\mu} = 0$, we define the Fourier components of the displacement vector as

$$\boldsymbol{u}\left(\boldsymbol{r}\right) = \sum_{\boldsymbol{G}} \boldsymbol{u}_{\boldsymbol{G}} \mathrm{e}^{i\boldsymbol{G}\cdot\boldsymbol{r}}. \tag{4.9}$$

where $\boldsymbol{G} = m_1\boldsymbol{G}_1 + m_2\boldsymbol{G}_2$ are the reciprocal lattice vector of strained moiré.

We also introduce $f_{\boldsymbol{G},j}$ by

$$\sin\left[\boldsymbol{G}_j \cdot \boldsymbol{r} + \boldsymbol{b}_j^0 \cdot (\boldsymbol{u}^{(2)}(\boldsymbol{r}) + \boldsymbol{u}^{(2)}(\boldsymbol{r}))\right] = \sum_{\boldsymbol{G}} f_{\boldsymbol{G},j} \mathrm{e}^{i\boldsymbol{G}\cdot\boldsymbol{r}}. \tag{4.10}$$

After some calculation using the above Fourier components, $\partial U/\partial u_\mu^{(l)} = 0$ for $(\mu = x, y)$ and $(l = 1, 2)$ gives the self-consistent equation as follows,

$$\begin{aligned} \boldsymbol{u}_{\boldsymbol{G}}^{(1)} &= -2V_0 \sum_{j=1}^{3} f_{\boldsymbol{G},j} \left[\hat{K}_{\boldsymbol{G}}^{(1)}\right]^{-1} \boldsymbol{b}_j^0 \\ \boldsymbol{u}_{\boldsymbol{G}}^{(2)} &= +2V_0 \sum_{j=1}^{3} f_{\boldsymbol{G},j} \left[\hat{K}_{\boldsymbol{G}}^{(2)}\right]^{-1} \boldsymbol{b}_j^0, \end{aligned} \tag{4.11}$$

where

$$\hat{K}_{\boldsymbol{G}}^{(l)} = \begin{pmatrix} \left(\lambda^{(l)} + 2\mu^{(l)}\right) G_x^2 + \mu^{(l)} G_y^2 & \left(\lambda^{(l)} + \mu^{(l)}\right) G_x G_y \\ \left(\lambda^{(l)} + \mu^{(l)}\right) G_x G_y & \left(\lambda^{(l)} + 2\mu^{(l)}\right) G_y^2 + \mu^{(l)} G_x^2 \end{pmatrix}. \tag{4.12}$$

By using Eq. (4.9),(4.10) and (4.11), we numerically solve the self-consistent equation while keeping the strained moiré period.

Continuum Hamiltonian

Here we define the continuum Hamiltonian for strained graphene/hBN following [68, 69]. The Hamiltonian for valley ξ is written as

$$\mathcal{H}^{(\xi)}(\boldsymbol{k}) = \begin{pmatrix} H_G(\boldsymbol{k}) & U^\dagger \\ U & H_{hBN} \end{pmatrix}, \tag{4.13}$$

where $H_G(\boldsymbol{k})$ and H_{hBN} are the 2×2 Hamiltonian of distorted monolayer graphene and hBN.

The $H_G(\boldsymbol{k})$ is given by

$$H_G(\boldsymbol{k}) = -\hbar v \left[(1+\mathcal{E})^{-1} \left(\boldsymbol{k} + \frac{e}{\hbar}\boldsymbol{A}\right)\right] \cdot \boldsymbol{\sigma}, \tag{4.14}$$

where v is the graphene's band velocity, $\boldsymbol{\sigma} = (\xi\sigma_x, \sigma_y)$ and σ_x, σ_y are the Pauli matrices in the sublattice space (A, B).

We take $\hbar v/a = 2.14$ eV [74]. The $\boldsymbol{A}$ is the strain-induced vector potential that is given

by[70, 75, 76]

$$\boldsymbol{A}^{(l)} = \xi\frac{3}{4}\frac{\beta\gamma_0}{ev}\begin{pmatrix}\epsilon_{xx}-\epsilon_{yy}\\ -2\epsilon_{xy}\end{pmatrix}. \tag{4.15}$$

$\gamma_0 = 2.7$ eV is the nearest neighbor transfer energy of intrinsic graphene and $\beta \approx 3.14$.

The effective Hamiltonian of hBN H_{hBN} is given by

$$H_{hBN} = \begin{pmatrix} V_N & 0\\ 0 & V_B\end{pmatrix}, \tag{4.16}$$

where V_N and V_B are the on-site potential of nitrogen and boron. We ignore the $\boldsymbol{k}$ dependence in this model.

U is the inter-layer coupling which written as

$$U = \sum_{j=1}^{3} U_j\, \mathrm{e}^{i\xi[\boldsymbol{q}_j\cdot\boldsymbol{r}+\boldsymbol{Q}_j\cdot(\boldsymbol{u}^{(2)}(\boldsymbol{r})-\boldsymbol{u}^{(1)}(\boldsymbol{r}))]}, \tag{4.17}$$

where we define

$$\begin{aligned} &q_1 = K^{(1)} - K^{(2)}, \quad q_2 = q_1 + \boldsymbol{G}_1, \quad q_3 = q_1 + \boldsymbol{G}_1 + \boldsymbol{G}_2\\ &Q_1 = K_+, \quad Q_2 = Q_1 + \boldsymbol{b}_1^0, \quad Q_3 = Q_1 + \boldsymbol{b}_1^0 + \boldsymbol{b}_2^0. \end{aligned} \tag{4.18}$$

and

$$U_1 = \begin{pmatrix} 1 & 1\\ 1 & 1\end{pmatrix}, \quad U_2 = \begin{pmatrix} 1 & \omega^{-\xi}\\ \omega^{+\xi} & 1\end{pmatrix}, \qquad U_3 = \begin{pmatrix} 1 & \omega^{+\xi}\\ \omega^{-\xi} & 1\end{pmatrix}. \tag{4.19}$$

The parameters $t_0 = 152$ meV is the interlayer coupling strength[77].

Chapter 5

Manipulating moires by controlling heterostrain in van der Waals devices: Additional details

His screaming is nearly gone from my mind - Twark Might

5.1 Massaging out strain with AFM tip

After performing an overlapping grid of 500x500 nm CAFM images of one device, MS24-B, we found that the sample appeared drastically less strained. However, the transport appeared unchanged. These large, overlapping CAFMs show some interesting signals in the lateral signal channel and strong dislocations in moire at the same locations.

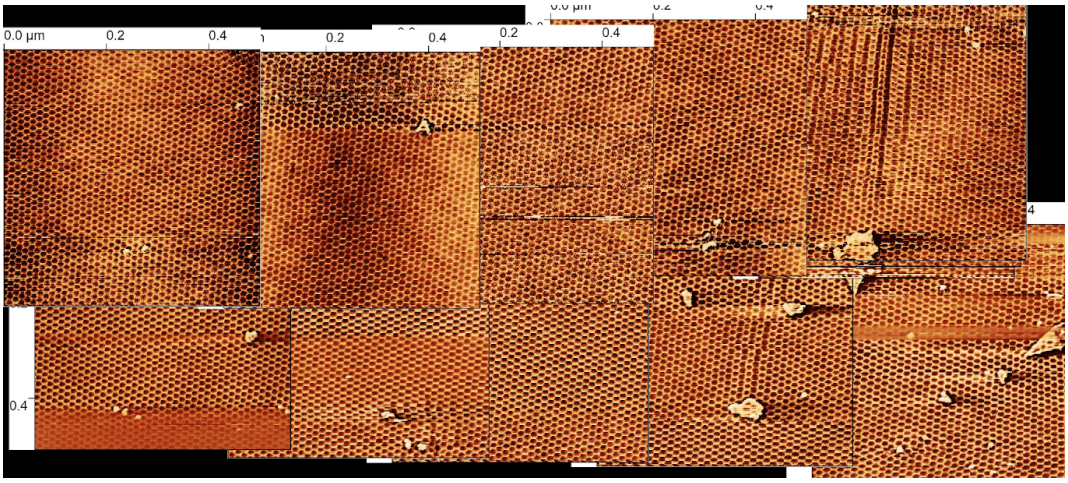

Figure 5.1: Stitched together CAFM images spanning the entire device (MS24-B)

Vertical dislocations in some of the right images correspond to lateral friction signals suggesting that the graphene is shifting as a result of the AFM scan.

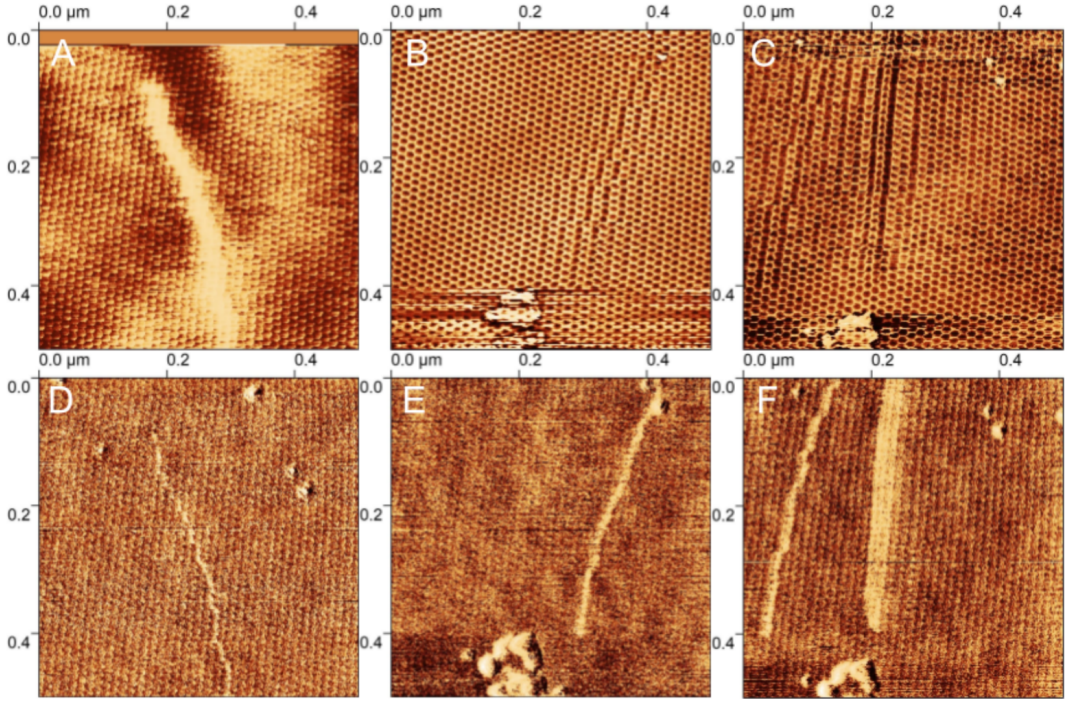

Figure 5.2: AFM moire dislocation streaks (MS24-B)

Top row: CAFM channel. **Bottom row:** LFM (Lateral) channel for the same scans. Clear streak-like dislocations in the CAFM amplitude data correspond to higher lateral signal. These suggest some mechanical shift in the graphene due to the scan.

5.2 AC Conductive AFM (and AFM internal lock-ins)

We perform conductive AFM differently from how Park suggests, which is a DC measurement. Instead we use the same external current amplifier scheme they outline, but we use one of the AFM's internal signal generators and lock-in amplifiers to perform a lock-in measurement. We have found this to be a more reliable method to image moires of graphene-hBN. It is possible that it may not be sufficient for imaging moires of the transition metal dichalcogenides due to their band gap. If there are issues, the lock-in signal could be combined with a DC offset to the sample bias in order to overcome the gap.

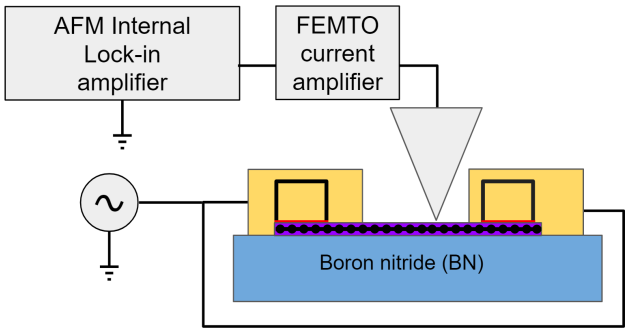

Figure 5.3: Conductive AFM circuit

Figure 5.4 shows the 4 AFM internal lock-in amplifiers. Each one differs slightly in what channels they can input or output to. Lock-in 1 is dedicated for NCM/Tapping mode and has a maximum frequency of 5 MHz. As far as I can tell its parameters are set as a result of an NCM sweep and can only be modified through the NCM Sweep window.

The other lock-ins can be configured by the user. 3 and 4 have a max frequency of 5 MHz; 2 has a max of 100kHz. All have a maximum output amplitude of 10V (peak to peak). All of the lock-ins get disabled/reset when switching between different tip modes, eg Tapping mode to Contact mode. According to Park this is for "safety reasons". Unfortunately, this means that lock-in 2, which can output its 100kHz voltage directly to the AFM tip, cannot be used for AFM Local Anodic Oxidation lithography unless the tip is in Contact mode

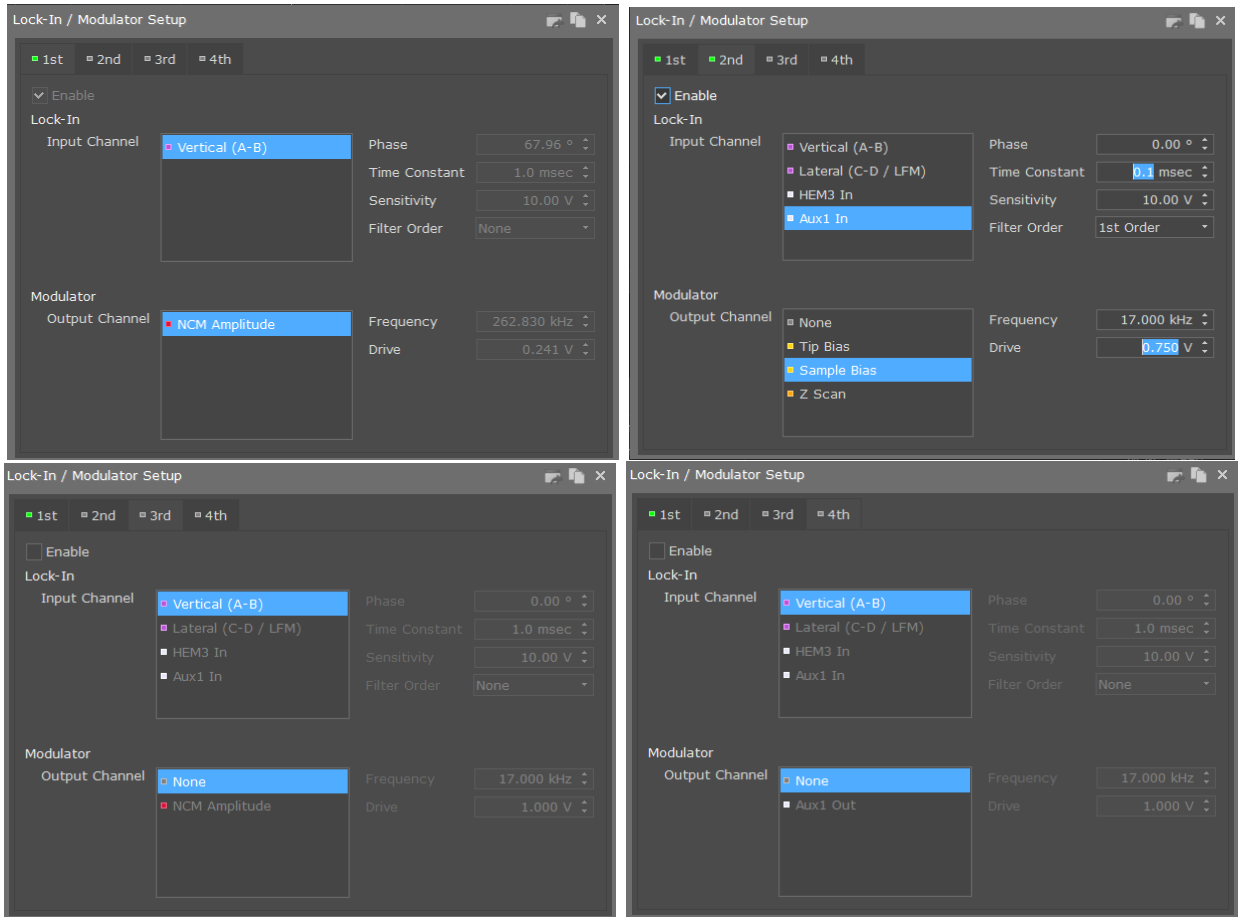

Figure 5.4: AFM 4 internal lock-ins

before performing lithography. So while the AFM technically has the ability to apply an AC voltage to the tip during lithography, it is less convenient than simply connecting a function generator to the AFM controller. We've told Park we want lithography to have this capability built in, in the same way a DC voltage can be applied. So they are likely working on it, but it doesn't hurt to remind them or check in on progress.

Lock-in 2 is shown configured to perform conductive AFM (CAFM) imaging of an open-face graphene-hBN moire device. The AC output of 17kHz and 0.75V is set to bias the sample. We use the default frequency of 17kHz because we found that the FEMTO current amplifier is noisier above ∼20 kHz. Other frequencies can still image a moire though, and in the past we've used frequencies ranging from 7kHz to 45kHz.

In order to reach the sample, the graphene must be electrically contacted, wirebonded, and shorted to the AFM puck. Usually we use a fully shorted chip carrier, which biases every pin on the chip carrier, including the back gate. It's likely that this is simultaneously gating the graphene, and it's also possible that there could be phase differences in the signals received by the different contacts or the gate. In practice, though, we have found no issues in measuring in this way. It wouldn't be unreasonable if this AC gating enhancing the CAFM signal either.

With the graphene biased, a conductive tip in contact will act as a path for current from the graphene. This current can be roughly in the $\sim$.1-100 µA range, depending on the resistance of the tip-graphene contact. We amplify this current using a FEMTO DLPCA-200 current amplifier, which is capable of AC current amplification from 10^3-10^{11} V/A. The output of the FEMTO is connected to the Aux1 In BNC on the AFM controller, which must be selected as the Input for Lock-in 2. It is also important to adjust the time constant from the default 1 ms, which cannot be to long compared to the drive frequency. We also usually apply the 1st Order filter, which strikes a reasonable balance between noise and smoothing. The Sensitivity is left at 10V to avoid inadvertently clipping the signal (which can happen as the tip-graphene contact resistance tends decrease over time). For this reason, we usually adjust the FEMTO gain to result in a lock-in amplitude voltage of .1-1 V. It may be necessary to adjust parameters for different moire systems. The lock-in signal can be seen in the Lock-in1/2/3/4 I/Q/Amplitude/Phase AFM channels. The I and Q channels are the in-phase and out-of-phase amplitudes, respectively.

This lock-in style measurement can also be performed using an external lock-in as well, such as our SRS830's or more advanced lock-ins such as high frequency Zurich Instruments lock-ins. To perform imaging with these, the lock-in should be connected in its standard way (applying a signal and measuring output at desired locations) and the amplitude/phase/etc should be output to the AFM controller's Aux Inputs, which can then be selected as imaging

channels.

A similar internal lock-in setup is used to perform PFM measurements with Lock-in 2, where the output is the Tip Bias and Input is the Vertical or Lateral signals. Additional details for that setup can be found in the Park PFM manuals.

In order to collect the minute current reaching the tip from the sample, the tip holder must be insulated from the rest of the AFM. We have done this by modifying a Park Clip Type Chip Carrier with an insulating layer of mica, which prevents the center tungsten ball on the probe hand from coming in electrical contact with the clip. This has the advantage of not requiring any modification/extra handling of the AFM head. Note, that this will not insulate from every Park probe hand. Our high frequency probe hand (up to 5MHz) has 3 tungsten balls instead of 2 ruby and 1 tungsten, so the alignment holes on the clip would also need to be insulated somehow.

Figure 5.5: AFM CAFM clip-type carrier
Left image: the top side of the soldered clip type chip carrier. A single pin socket has soldered directly to the edge of the clip and partially ground down in order to keep from interfering with the cantilever exchanger (the large black screw-down object for swapping the tip in the clip). **Right image:** the underside. A small square of 10 µm thick mica (measured with calipers) has been attached to the bottom using Crystal Bond.

It's possible that this mica insulation could degrade over time, so I wouldn't take this

insulation for granted. Though, it's hard to imagine there would be much leakage over such a thick object, when the tip is not actually be voltage biased for CAFM. It may be relevant to measure leakage for voltages up to 1-10 V, as are used for PFM. If it needs to be replaced, the Crystal Bond is soluble in acetone.

There are other options to achieve this tip insulation, but they are much less convenient. The stock option are PTFE or ceramic insulated holders with glued AFM tips, which would be much more time consuming or expensive to replace. Our system also has an alternative probe hand with a PEEK clamp. This is also not convenient because the AFM head must be removed, the probe hand swapped out, and a tip mounted into the clamp each time. This makes swapping between CAFM, imaging, and manipulating significantly more time-consuming. A third option would be to simply disconnect the 3-wire plug for the probe hand. This would electrically isolate the probe hand, but also disconnect the vibration piezo, preventing NCM or Tapping mode from being used. Yet another option would be to only disconnect the single tip bias wire from that plug. I have not tried this, and you would need to be careful not to damage the wire crimp.

5.3 *In situ* AFM measurement

In ordered to perform AFM manipulations with electrical feedback (and also perform gate sweeps in quick succession) I soldered and mounted a 16 pin DIP socket to an AFM puck. The wiring and pins are held up from the puck with a piece of white delrin epoxied to the puck (not PTFE which is very hard to glue to). The wires are twisted pairs of polyamide insulated magnet wire (from the Attocube wiring kit), and they are clamped to the delrin with a nylon screw and PTFE washer in order to keep strain from directly reaching the solder joints. Only plastic comes into contact with the wires to avoid scratching through the thin polyamide insulation.

This wiring it honestly too thick, and it applies a significant force to the puck. To minimize this force the wires are coiled into a loose spring. The thick cable they are connected to must be taped down as well. Ideally, thinner wire, perhaps something like the cryoloom (which would be horrific to have to solder) or an extremely flexible polyamide ribbon cable/wire could be used.

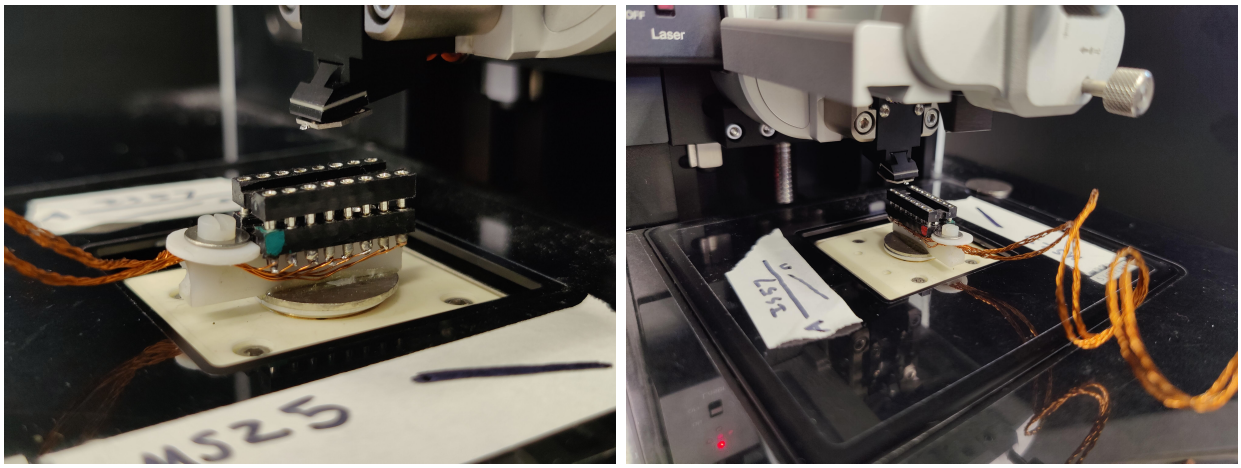

Figure 5.6: AFM wired DIP socket

5.4 AFM drift velocity

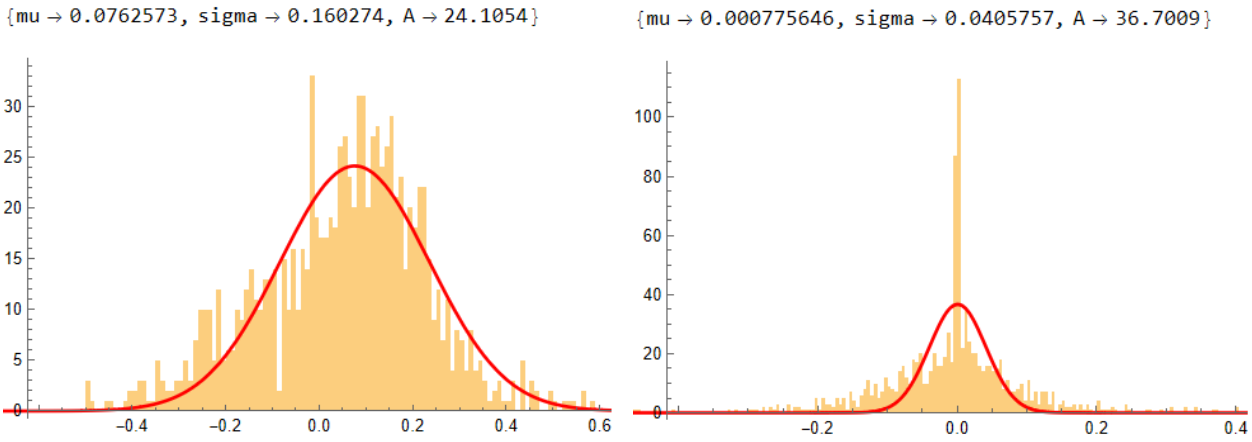

Figure 5.7: AFM drift velocities in y and x direction

These histograms take data from ∼1000 AFM images of different devices. The left is the y-velocity and right is x-velocity.

The drift in the y direction is much larger, on average, than in x, and the standard deviation is much larger as well. This is likely because the cantilever is tilted along that direction, so drifts in the height of any of the materials in the entire (∼10 cm scale) AFM stack can result in a translation in the y direction.

5.5 Moire Fitting Error

We determine the uncertainty for our moire fit parameters using a numerical inversion of the our code to generate the moire reciprocal lattice vectors. We create a range of parameters around a specific global angle, twist angle, graphene strain, and strain angle (a 4D cube in the parameter space) and generate moire reciprocal lattice vectors for every possible parameter combination. We then filter out the points which lie outside a desired error range of all 3 measured reciprocal lattice points. We choose 1% for this error primarily based on the spread in sequential moire lattice measurements in a single position.

Generating the 4D cube of parameters and calculating the corresponding moire wavevectors for all of them is very time consuming; a 30x30x30x30 cube takes ∼20 minutes. Thus this method would not be acceptable if one wanted to perform error analysis for many points.

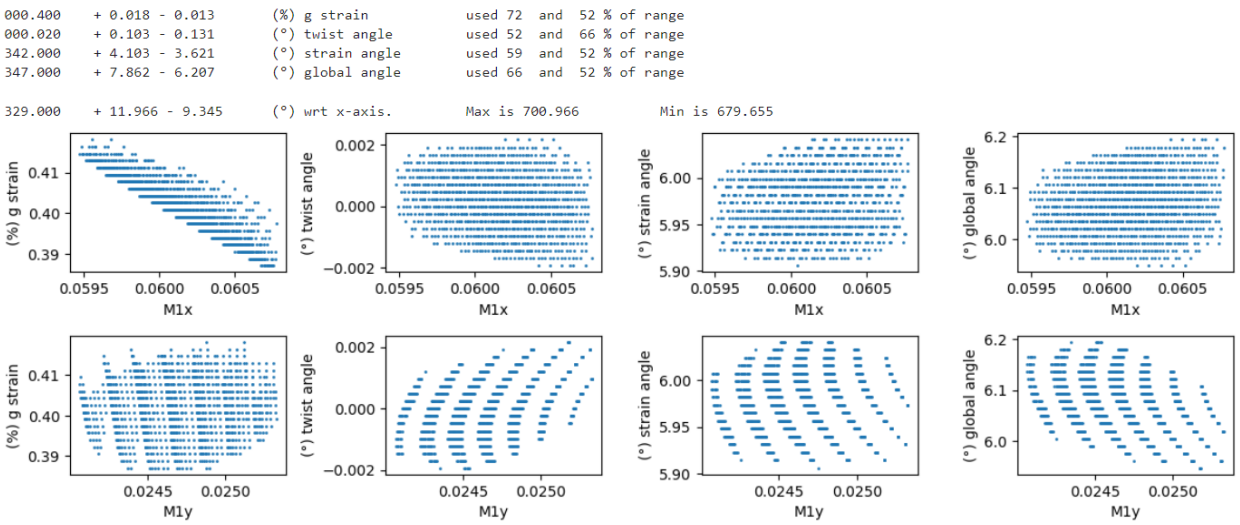

Figure 5.8: Output from moire error analysis

Range of filtered parameters for M1x and M1y. If these points were too sparse, it would suggest that the parameter hypercube should be shrunk or the number of points should be increased in order to increase the density and more accurately measure a spread in parameters. Only M1 is plotted for brevity, however it may be necessary to make these plots for M2 and/or M3 as well if one of them is not sufficiently dense.

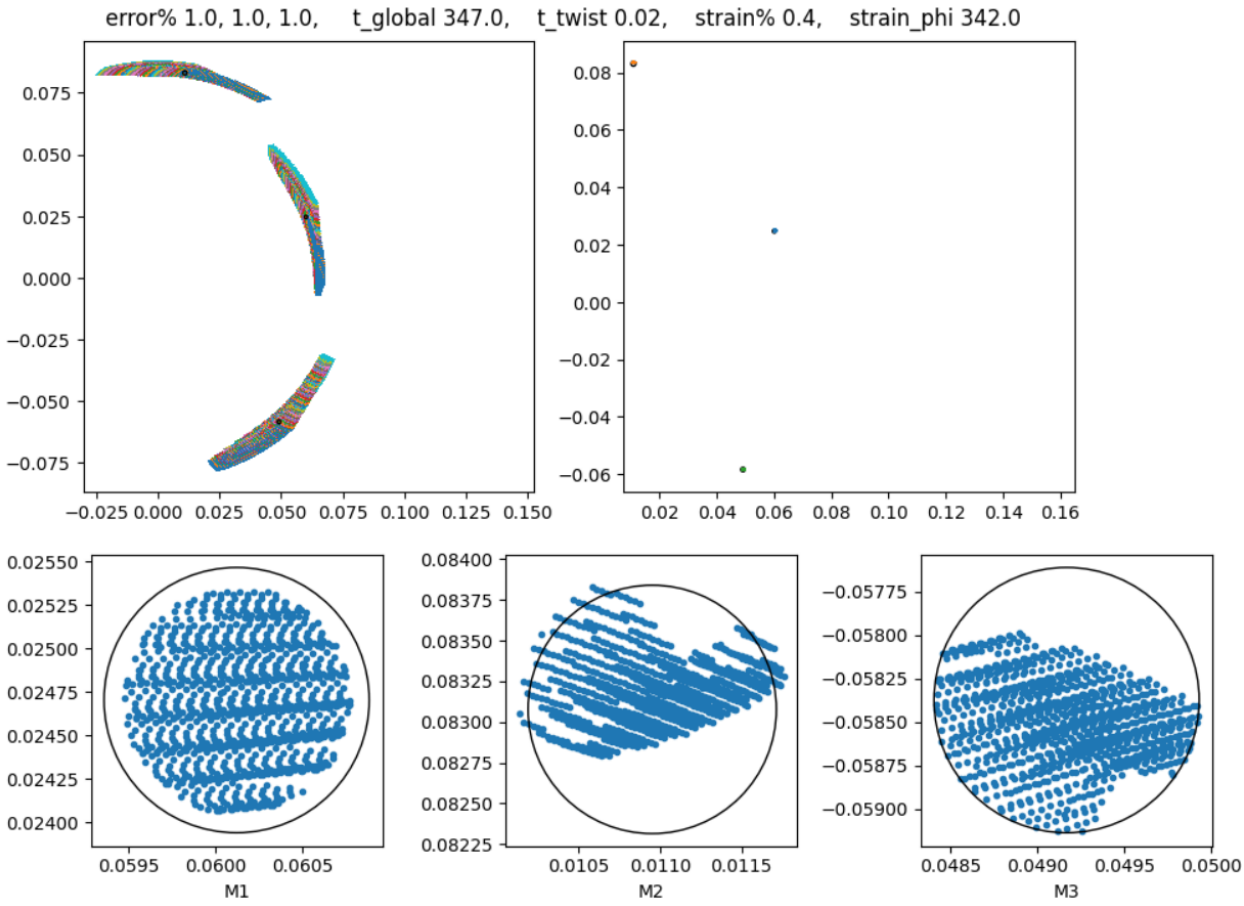

Figure 5.9: Addtional output from moire error analysis

First row: Plot of all generated moire wavevectors from the parameter cube with black circles showing the central parameters and their error range. Right plot is the same except with the filter applied. **Second row:** Zoomed in plots of the filtered moires. All points should only exist inside the circles, however, some are outside of the boundaries for some reason. This results in an overestimate in the error for this range. Not all of the circles are fully filled in this filtered case because all 3 moire wavevectors must land within the error bound for M1,M2,M3. Thus a point may be inside the M1 error bound, but outside the M2 and therefore be excluded.

Bibliography

[1] M. Dienwiebel, G. S. Verhoeven, N. Pradeep, J. W. M. Frenken, J. A. Heimberg, and H. W. Zandbergen, "Superlubricity of graphite," *Physical Review Letters*, vol. 92, Mar. 2004.

[2] O. Hod, E. Meyer, Q. Zheng, and M. Urbakh, "Structural superlubricity and ultralow friction across the length scales," *Nature*, vol. 563, no. 7732, pp. 485–492, 2018.

[3] E. Koren, E. Lörtscher, C. Rawlings, A. W. Knoll, and U. Duerig, "Adhesion and friction in mesoscopic graphite contacts," *Science*, vol. 348, no. 6235, pp. 679–683, 2015.

[4] Y. Song, D. Mandelli, O. Hod, M. Urbakh, M. Ma, and Q. Zheng, "Robust microscale superlubricity in graphite/hexagonal boron nitride layered heterojunctions," *Nature Materials*, vol. 17, no. 10, pp. 894–899, 2018.

[5] H. Rokni and W. Lu, "Direct measurements of interfacial adhesion in 2d materials and van der waals heterostructures in ambient air," *Nature Communications*, vol. 11, no. 1, p. 5607, 2020.

[6] Z. Liu, J. Yang, F. Grey, J. Z. Liu, Y. Liu, Y. Wang, Y. Yang, Y. Cheng, and Q. Zheng, "Observation of microscale superlubricity in graphite," *Physical Review Letters*, vol. 108, no. 20, p. 205503, 2012.

[7] M. Liao, P. Nicolini, L. Du, J. Yuan, S. Wang, H. Yu, J. Tang, P. Cheng, K. Watanabe, T. Taniguchi, L. Gu, V. E. P. Claerbout, A. Silva, D. Kramer, T. Polcar, R. Yang, D. Shi, and G. Zhang, "UItra-low friction and edge-pinning effect in large-lattice-mismatch van der waals heterostructures," *Nature Materials*, vol. 21, no. 1, pp. 47–53, 2022.

[8] R. Ribeiro-Palau, C. Zhang, K. Watanabe, T. Taniguchi, J. Hone, and C. R. Dean, "Twistable electronics with dynamically rotatable heterostructures," *Science*, vol. 361, no. 6403, pp. 690–693, 2018.

[9] N. R. Finney, M. Yankowitz, L. Muraleetharan, K. Watanabe, T. Taniguchi, C. R. Dean, and J. Hone, "Tunable crystal symmetry in graphene–boron nitride heterostructures with coexisting moiré superlattices," *Nature Nanotechnology*, vol. 14, no. 11, pp. 1029–1034, 2019.

[10] T. Chari, R. Ribeiro-Palau, C. R. Dean, and K. Shepard, "Resistivity of rotated graphite–graphene contacts," *Nano Letters*, vol. 16, no. 7, pp. 4477–4482, 2016.

[11] E. Koren, I. Leven, E. Lörtscher, A. Knoll, O. Hod, and U. Duerig, "Coherent commensurate electronic states at the interface between misoriented graphene layers," *Nature Nanotechnology*, vol. 11, no. 9, pp. 752–757, 2016.

[12] S. D. Senturia, *Microsystem Design*. Springer US, 2021.

[13] D. Dietzel, A. S. D. Wijn, M. Vorholzer, and A. Schirmeisen, "Friction fluctuations of gold nanoparticles in the superlubric regime," *Nanotechnology*, vol. 29, no. 15, p. 155702, 2018.

[14] D. Dietzel, M. Feldmann, U. D. Schwarz, H. Fuchs, and A. Schirmeisen, "Scaling laws of structural lubricity," *Physical Review Letters*, vol. 111, no. 23, p. 235502, 2013.

[15] L. Banszerus, A. Rothstein, E. Icking, S. Möller, K. Watanabe, T. Taniguchi, C. Stampfer, and C. Volk, "Tunable interdot coupling in few-electron bilayer graphene double quantum dots," *Applied Physics Letters*, vol. 118, no. 10, p. 103101, 2021.

[16] L. A. Cohen, N. L. Samuelson, T. Wang, K. Klocke, C. C. Reeves, T. Taniguchi, K. Watanabe, S. Vijay, M. P. Zaletel, and A. F. Young, "Nanoscale electrostatic control in ultra clean van der waals heterostructures by local anodic oxidation of graphite gates," 2024.

[17] H. Overweg, H. Eggimann, X. Chen, S. Slizovskiy, M. Eich, R. Pisoni, Y. Lee, P. Rickhaus, K. Watanabe, T. Taniguchi, V. Fal'ko, T. Ihn, and K. Ensslin, "Electrostatically induced quantum point contacts in bilayer graphene," *Nano Letters*, vol. 18, no. 1, pp. 553–559, 2018.

[18] C. Déprez, L. Veyrat, H. Vignaud, G. Nayak, K. Watanabe, T. Taniguchi, F. Gay, H. Sellier, and B. Sacépé, "A tunable fabry–pérot quantum hall interferometer in graphene," *Nature Nanotechnology*, vol. 16, no. 5, pp. 555–562, 2021.

[19] J. Nakamura, S. Liang, G. C. Gardner, and M. J. Manfra, "Direct observation of anyonic braiding statistics," *Nature Physics*, vol. 16, no. 9, pp. 931–936, 2020.

[20] A. F. Young, C. R. Dean, L. Wang, H. Ren, P. Cadden-Zimansky, K. Watanabe, T. Taniguchi, J. Hone, K. L. Shepard, and P. Kim, "Spin and valley quantum hall ferromagnetism in graphene," *Nature Physics*, vol. 8, no. 7, pp. 550–556, 2012.

[21] K. Zimmermann, A. Jordan, F. Gay, K. Watanabe, T. Taniguchi, Z. Han, V. Bouchiat, H. Sellier, and B. Sacépé, "Tunable transmission of quantum hall edge channels with full degeneracy lifting in split-gated graphene devices," *Nature Communications*, vol. 8, no. 1, p. 14983, 2017.

[22] Y. Ronen, T. Werkmeister, D. Haie Najafabadi, A. T. Pierce, L. E. Anderson, Y. J. Shin, S. Y. Lee, Y. H. Lee, B. Johnson, K. Watanabe, T. Taniguchi, A. Yacoby, and P. Kim, "Aharonov–bohm effect in graphene-based fabry–pérot quantum hall interferometers," *Nature Nanotechnology*, vol. 16, no. 5, pp. 563–569, 2021.

[23] X. Zhao, M. Hamilton, W. G. Sawyer, and S. S. Perry, "Thermally activated friction," *Tribology Letters*, vol. 27, no. 1, pp. 113–117, 2007.

[24] M. A. Topinka, B. J. LeRoy, S. E. J. Shaw, E. J. Heller, R. M. Westervelt, K. D. Maranowski, and A. C. Gossard, "Imaging coherent electron flow from a quantum point contact," *Science*, vol. 289, p. 2323–2326, Sept. 2000.

[25] J. Xue, J. Sanchez-Yamagishi, D. Bulmash, P. Jacquod, A. Deshpande, K. Watanabe, T. Taniguchi, P. Jarillo-Herrero, and B. J. LeRoy, "Scanning tunnelling microscopy and spectroscopy of ultra-flat graphene on hexagonal boron nitride," *Nature Materials*, vol. 10, p. 282–285, Feb. 2011.

[26] M. Fujimoto, H. Koschke, and M. Koshino, "Topological charge pumping by a sliding moiré pattern," *Physical Review B*, vol. 101, Jan. 2020.

[27] Y. Zhang, Y. Gao, and D. Xiao, "Topological charge pumping in twisted bilayer graphene," *Physical Review B*, vol. 101, Jan. 2020.

[28] Y. Su and S.-Z. Lin, "Topological sliding moiré heterostructure," *Physical Review B*, vol. 101, Jan. 2020.

[29] F. Pizzocchero, L. Gammelgaard, B. S. Jessen, J. M. Caridad, L. Wang, J. Hone, P. Bøggild, and T. J. Booth, "The hot pick-up technique for batch assembly of van der waals heterostructures," *Nature Communications*, vol. 7, June 2016.

[30] D. G. Purdie, N. M. Pugno, T. Taniguchi, K. Watanabe, A. C. Ferrari, and A. Lombardo, "Cleaning interfaces in layered materials heterostructures," *Nature Communications*, vol. 9, Dec. 2018.

[31] A. Inbar, J. Birkbeck, J. Xiao, T. Taniguchi, K. Watanabe, B. Yan, Y. Oreg, A. Stern, E. Berg, and S. Ilani, "The quantum twisting microscope," *Nature*, vol. 614, no. 7949, pp. 682–687, 2023.

[32] Y. Yang, J. Li, J. Yin, S. Xu, C. Mullan, T. Taniguchi, K. Watanabe, A. K. Geim, K. S. Novoselov, and A. Mishchenko, "In situ manipulation of van der waals heterostructures for twistronics," *Science Advances*, vol. 6, no. 49, p. eabd3655, 2020.

[33] M. Kapfer, B. S. Jessen, M. E. Eisele, M. Fu, D. R. Danielsen, T. P. Darlington, S. L. Moore, N. R. Finney, A. Marchese, V. Hsieh, P. Majchrzak, Z. Jiang, D. Biswas, P. Dudin, J. Avila, K. Watanabe, T. Taniguchi, S. Ulstrup, P. Bøggild, P. J. Schuck, D. N. Basov, J. Hone, and C. R. Dean, "Programming twist angle and strain profiles in 2d materials," *Science*, vol. 381, no. 6658, pp. 677–681, 2023.

[34] J. S. Alden, A. W. Tsen, P. Y. Huang, R. Hovden, L. Brown, J. Park, D. A. Muller, and P. L. McEuen, "Strain solitons and topological defects in bilayer graphene," *Proceedings of the National Academy of Sciences*, vol. 110, no. 28, pp. 11256–11260, 2013.

[35] M. Kögl, P. Soubelet, M. Brotons-Gisbert, A. V. Stier, B. D. Gerardot, and J. J. Finley, "Moiré straintronics: a universal platform for reconfigurable quantum materials," *npj 2D Materials and Applications*, vol. 7, no. 1, p. 32, 2023.

[36] F. Escudero, A. Sinner, Z. Zhan, P. A. Pantaleón, and F. Guinea, "Designing moiré patterns by strain," *Physical Review Research*, vol. 6, no. 2, p. 023203, 2024.

[37] J. Finney, A. L. Sharpe, E. J. Fox, C. L. Hsueh, D. E. Parker, M. Yankowitz, S. Chen, K. Watanabe, T. Taniguchi, C. R. Dean, A. Vishwanath, M. A. Kastner, and D. Goldhaber-Gordon, "Unusual magnetotransport in twisted bilayer graphene," *Proceedings of the National Academy of Sciences*, vol. 119, no. 16, p. e2118482119, 2022.

[38] X. Wang, J. Finney, A. L. Sharpe, L. K. Rodenbach, C. L. Hsueh, K. Watanabe, T. Taniguchi, M. A. Kastner, O. Vafek, and D. Goldhaber-Gordon, "Unusual magnetotransport in twisted bilayer graphene from strain-induced open fermi surfaces," *Proceedings of the National Academy of Sciences*, vol. 120, no. 34, p. e2307151120, 2023.

[39] A. Kerelsky, L. J. McGilly, D. M. Kennes, L. Xian, M. Yankowitz, S. Chen, K. Watanabe, T. Taniguchi, J. Hone, C. Dean, A. Rubio, and A. N. Pasupathy, "Maximized electron interactions at the magic angle in twisted bilayer graphene," *Nature*, vol. 572, no. 7767, pp. 95–100, 2019.

[40] L. Huder, A. Artaud, T. Le Quang, G. T. De Laissardière, A. G. Jansen, G. Lapertot, C. Chapelier, and V. T. Renard, "Electronic spectrum of twisted graphene layers under heterostrain," *Physical Review Letters*, vol. 120, no. 15, p. 156405, 2018.

[41] F. Mesple, A. Missaoui, T. Cea, L. Huder, F. Guinea, G. Trambly De Laissardière, C. Chapelier, and V. T. Renard, "Heterostrain determines flat bands in magic-angle twisted graphene layers," *Physical Review Letters*, vol. 127, no. 12, p. 126405, 2018.

[42] J.-B. Qiao, L.-J. Yin, and L. He, "Twisted graphene bilayer around the first magic angle engineered by heterostrain," *Physical Review B*, vol. 98, no. 23, p. 235402, 2018.

[43] Y. Xie, B. Lian, B. Jäck, X. Liu, C.-L. Chiu, K. Watanabe, T. Taniguchi, B. A. Bernevig, and A. Yazdani, "Spectroscopic signatures of many-body correlations in magic-angle twisted bilayer graphene," *Nature*, vol. 572, no. 7767, pp. 101–105, 2019.

[44] Y. Choi, J. Kemmer, Y. Peng, A. Thomson, H. Arora, R. Polski, Y. Zhang, H. Ren, J. Alicea, G. Refael, F. Von Oppen, K. Watanabe, T. Taniguchi, and S. Nadj-Perge, "Electronic correlations in twisted bilayer graphene near the magic angle," *Nature Physics*, vol. 15, no. 11, pp. 1174–1180, 2019.

[45] Y. Bai, L. Zhou, J. Wang, W. Wu, L. J. McGilly, D. Halbertal, C. F. B. Lo, F. Liu, J. Ardelean, P. Rivera, N. R. Finney, X.-C. Yang, D. N. Basov, W. Yao, X. Xu, J. Hone, A. N. Pasupathy, and X.-Y. Zhu, "Excitons in strain-induced one-dimensional moiré potentials at transition metal dichalcogenide heterojunctions," *Nature Materials*, vol. 19, no. 10, pp. 1068–1073, 2020.

[46] L. Zhang, Y. Wang, R. Hu, P. Wan, O. Zheliuk, M. Liang, X. Peng, Y.-J. Zeng, and J. Ye, "Correlated states in strained twisted bilayer graphenes away from the magic angle," *Nano Letters*, vol. 22, no. 8, pp. 3204–3211, 2022.

[47] X. Gao, H. Sun, D.-H. Kang, C. Wang, Q. J. Wang, and D. Nam, "Heterostrain-enabled dynamically tunable moiré superlattice in twisted bilayer graphene," *Scientific Reports*, vol. 11, no. 1, p. 21402, 2021.

[48] L. Wang, S. Zihlmann, A. Baumgartner, J. Overbeck, K. Watanabe, T. Taniguchi, P. Makk, and C. Schönenberger, "In situ strain tuning in hBN-encapsulated graphene electronic devices," *Nano Letters*, vol. 19, no. 6, pp. 4097–4102, 2019.

[49] Z. Liu, X. Ma, J. Cenker, J. Cai, Z. Fei, P. Malinowski, J. Mutch, Y. Zhao, K. Hwangbo, Z. Lin, A. Manna, J. Yang, D. Cobden, X. Xu, M. Yankowitz, and J.-H. Chu, "Continuously tunable uniaxial strain control of van der waals heterostructure devices," *Journal of Applied Physics*, vol. 135, no. 20, p. 204306, 2024.

[50] T. Peña, S. A. Chowdhury, A. Azizimanesh, A. Sewaket, H. Askari, and S. M. Wu, "Strain engineering 2d MoS $_2$ with thin film stress capping layers," *2D Materials*, vol. 8, no. 4, p. 045001, 2021.

[51] Y. Zhang, H. L. Zhao, S. Huang, M. A. Hossain, and A. M. Van Der Zande, "Enhancing carrier mobility in monolayer MoS $_2$ transistors with process-induced strain," *ACS Nano*, vol. 18, no. 19, pp. 12377–12385, 2024.

[52] Y. Zhang, M. A. Hossain, K. J. Hwang, P. F. Ferrari, J. Maduzia, T. Peña, S. M. Wu, E. Ertekin, and A. M. Van Der Zande, "Patternable process-induced strain in 2d monolayers and heterobilayers," *ACS Nano*, vol. 18, no. 5, pp. 4205–4215, 2024.

[53] A. Z. Barabas, I. Sequeira, Y. Yang, A. H. Barajas-Aguilar, T. Taniguchi, K. Watanabe, and J. D. Sanchez-Yamagishi, "Mechanically reconfigurable van der waals devices via low-friction gold sliding," *Science Advances*, vol. 9, no. 14, p. eadf9558, 2023.

[54] H. Polshyn, M. Yankowitz, S. Chen, Y. Zhang, K. Watanabe, T. Taniguchi, C. R. Dean, and A. F. Young, "Large linear-in-temperature resistivity in twisted bilayer graphene," *Nature Physics*, vol. 15, no. 10, pp. 1011–1016, 2019.

[55] L. A. Ponomarenko, R. V. Gorbachev, G. L. Yu, D. C. Elias, R. Jalil, A. A. Patel, A. Mishchenko, A. S. Mayorov, C. R. Woods, J. R. Wallbank, M. Mucha-Kruczynski, B. A. Piot, M. Potemski, I. V. Grigorieva, K. S. Novoselov, F. Guinea, V. I. Fal'ko, and A. K. Geim, "Cloning of dirac fermions in graphene superlattices," *Nature*, vol. 497, no. 7451, pp. 594–597, 2013.

[56] B. Hunt, J. D. Sanchez-Yamagishi, A. F. Young, M. Yankowitz, B. J. LeRoy, K. Watanabe, T. Taniguchi, P. Moon, M. Koshino, P. Jarillo-Herrero, and R. C. Ashoori, "Massive dirac fermions and hofstadter butterfly in a van der waals heterostructure," *Science*, vol. 340, no. 6139, pp. 1427–1430, 2013.

[57] J. Jung, A. M. DaSilva, A. H. MacDonald, and S. Adam, "Origin of band gaps in graphene on hexagonal boron nitride," *Nature Communications*, vol. 6, no. 1, p. 6308, 2015.

[58] A. Aharon-Steinberg, A. Marguerite, D. J. Perello, K. Bagani, T. Holder, Y. Myasoedov, L. S. Levitov, A. K. Geim, and E. Zeldov, "Long-range nontopological edge currents in charge-neutral graphene," *Nature*, vol. 593, no. 7860, pp. 528–534, 2021.

[59] Y.-T. Cui, B. Wen, E. Y. Ma, G. Diankov, Z. Han, F. Amet, T. Taniguchi, K. Watanabe, D. Goldhaber-Gordon, C. R. Dean, and Z.-X. Shen, "Unconventional correlation between quantum hall transport quantization and bulk state filling in gated graphene devices," *Physical Review Letters*, vol. 117, no. 18, p. 186601, 2016.

[60] H. Li, Z. Ying, B. Lyu, A. Deng, L. Wang, T. Taniguchi, K. Watanabe, and Z. Shi, "Electrode-free anodic oxidation nanolithography of low-dimensional materials," *Nano Letters*, vol. 18, no. 12, pp. 8011–8015, 2018.

[61] H. Ramamoorthy and R. Somphonsane, "In-situ current annealing of graphene-metal contacts," *Journal of Physics: Conference Series*, vol. 1144, p. 012186, 2018.

[62] S. J. Tran, J.-L. Uslu, M. Pendharkar, J. Finney, A. L. Sharpe, M. Hocking, N. J. Bittner, K. Watanabe, T. Taniguchi, M. A. Kastner, A. J. Mannix, and D. Goldhaber-Gordon, "Quantitative determination of twist angle and strain in van der waals moir\'e superlattices," 2024.

[63] C. Lee, X. Wei, J. W. Kysar, and J. Hone, "Measurement of the elastic properties and intrinsic strength of monolayer graphene," *Science*, vol. 321, no. 5887, pp. 385–388, 2008.

[64] O. L. Blakslee, D. G. Proctor, E. J. Seldin, G. B. Spence, and T. Weng, "Elastic constants of compression-annealed pyrolytic graphite," *Journal of Applied Physics*, vol. 41, no. 8, pp. 3373–3382, 1970.

[65] G. Ventura and M. Perfetti, *Thermal Expansion*, pp. 81–91. Springer Netherlands, 2014. Series Title: International Cryogenics Monograph Series.

[66] N. N. T. Nam and M. Koshino, "Lattice relaxation and energy band modulation in twisted bilayer graphene," *Physical Review B*, vol. 96, no. 7, p. 075311, 2017.

[67] L. P. A. Krisna and M. Koshino, "Moiré phonons in graphene/hexagonal boron nitride moiré superlattice," *Physical Review B*, vol. 107, no. 11, p. 115301, 2023.

[68] M. Koshino and N. N. T. Nam, "Effective continuum model for relaxed twisted bilayer graphene and moiré electron-phonon interaction," *Physical Review B*, vol. 101, no. 19, p. 195425, 2020.

[69] N. Nakatsuji and M. Koshino, "Moiré disorder effect in twisted bilayer graphene," *Physical Review B*, vol. 105, no. 24, p. 245408, 2022.

[70] H. Suzuura and T. Ando, "Phonons and electron-phonon scattering in carbon nanotubes," *Physical Review B*, vol. 65, no. 23, p. 235412, 2002.

[71] P. San-Jose, A. Gutiérrez-Rubio, M. Sturla, and F. Guinea, "Electronic structure of spontaneously strained graphene on hexagonal boron nitride," *Physical Review B*, vol. 90, no. 11, p. 115152, 2014.

[72] K. V. Zakharchenko, M. I. Katsnelson, and A. Fasolino, "Finite temperature lattice properties of graphene beyond the quasiharmonic approximation," *Physical Review Letters*, vol. 102, no. 4, p. 046808, 2009.

[73] B. Sachs, T. O. Wehling, M. I. Katsnelson, and A. I. Lichtenstein, "Adhesion and electronic structure of graphene on hexagonal boron nitride substrates," *Physical Review B*, vol. 84, no. 19, p. 195414, 2011.

[74] M. Koshino, N. F. Yuan, T. Koretsune, M. Ochi, K. Kuroki, and L. Fu, "Maximally localized wannier orbitals and the extended hubbard model for twisted bilayer graphene," *Physical Review X*, vol. 8, no. 3, p. 031087, 2018.

[75] V. M. Pereira and A. H. Castro Neto, "Strain engineering of graphene's electronic structure," *Physical Review Letters*, vol. 103, no. 4, p. 046801, 2009.

[76] F. Guinea, M. I. Katsnelson, and A. K. Geim, "Energy gaps and a zero-field quantum hall effect in graphene by strain engineering," *Nature Physics*, vol. 6, no. 1, pp. 30–33, 2010.

[77] P. Moon and M. Koshino, "Electronic properties of graphene/hexagonal-boron-nitride moiré superlattice," *Physical Review B*, vol. 90, no. 15, p. 155406, 2014.